2021

Perovskite Thin Films Annealed in Supercritical fluids for Efficient Solar Cells

Gilbert Annohene
Virginia Commonwealth University

Perovskite Thin Films Annealed in Supercritical fluids for Efficient Solar Cells

A Dissertation submitted in partial fulfillment of the requirements for the degree of Doctor of

Philosophy at Virginia Commonwealth University.

by

GILBERT ANNOHENE

Mechanical and Nuclear Engineering – May, 2021

Director: Dr. Gary C. Tepper

Department Chair, Professor, Department of Mechanical and Nuclear Engineering

Virginia Commonwealth University

Richmond, Virginia

ACKNOWLEDGEMENTS

First, I would like to acknowledge my Research Director, Dr. Gary Tepper, for creating a supportive environment during my Ph.D. program. I am exceptionally blessed to have had the opportunity to work beneath the supervision of a really experienced and learned advisor who was continuously accessible and put me in positions to exceed expectations. I will always look forward to learning from the new scientific advances from his research group.

I am extremely grateful to everyone who supported my work at Virginia Commonwealth University (VCU). I am thankful to VCU College of Engineering and the Department of Mechanical and Nuclear Engineering for supporting and funding all my research work. The Nanomaterials Core Characterization Facility at VCU helped in all of the material characterizations of my samples. I would like to appreciate the Virginia Microelectronic Center for assisting me in making my complex devices. I am thankful to Dr. Karla Mossi for all her support in my graduate coursework and for helping me determine the right opportunities.

I would like to thank my committee members: Dr. Ram Gupta, Dr. Hong Zhao, Dr. Carlos Castano, and Dr. Dmitry Pestov. I appreciated their guidance during my Ph.D. proposal, which steered me in the right direction. All members were so accommodating by bringing their knowledge and experience to my assistance throughout my research. They have always been available whenever I needed information on various aspect of my project, and they helped me expand my knowledge. In terms of research subject, experimental methods, and writing style, their research work has also been an inspiration to me.

Without the help of my friends and family, I would not have made it this far. I owe a debt of gratitude to my friends for making my time at VCU so unforgettable. I appreciate working with

TABLE OF CONTENTS

LIST OF FIGURES

LIST OF TABLES

NOMENCLATURE

$CH_3NH_3PbI_3$ Methylammonium Lead Trihalide Perovskite

CH_3NH_3I Methylammonium Iodide

SCF   Supercritical Fluid

$scCO_2$ Supercritical Carbon Dioxide

CO_2 Carbon dioxide

PCE and η   Power Conversion Efficiency

PSC(s)   Perovskite Solar Cell(s)

J_{sc} Short Circuit Current

J_{mp} Current at maximum power

V_{oc} Open Circuit Voltage

V_{mp} Voltage at maximum power

FF   Fill Factor

P_s Power density

HTL   Hole Transport Layer

ETL   Electron Transport Layer

TiO_2 Titanium Oxide

NiO   Nickel Oxide

ZnO   Zinc Oxide

Spiro-OMeTAD   2,2',7,7'-Tetrakis[N,N-di(4-methoxyphenyl)amino]-

                       9,9'-spirobifluorene

PEDOT:PSS   poly(3,4-ethylenedioxythiophene) polystyrene sulfonate

PCBM   [6,6]-Phenyl-C61-butyric acid methyl ester

P3HT   Poly(3-hexylthiophene-2,5-diyl)

PbI_2 Lead (II) Iodide

MA   Methylammonium

HI   Hydrogen Iodide

THF   Tetrahydrofuran

DMF   N,N-dimethylformamide

Ag   Silver

ABSTRACT

In the field of photovoltaics, scientists and researchers are working fervently to produce a combination of efficient, stable, low cost and scalable devices. Because of its high photovoltaic efficiency, low cost, and ease of manufacture, methylammonium lead trihalide perovskite ($CH_3NH_3PbI_3$) has sparked a lot of interest. Their high absorption coefficient, tunable band gap, low temperature processing compared to other thin film absorber materials, and abundant elemental constituent makes the technology highly advantageous. Since the perovskite film is so critical in the application, researchers have looked into morphology, crystallization, compositional and interface engineering to improve its efficiency and stability.

High temperatures necessary for crystallization of organic-inorganic hybrid perovskite films can have detrimental effects such as degradation of perovskite into other products (impurities) resulting in non-uniform optoelectronic performance across the thickness of the active layer, thus reducing photovoltaic performance. Furthermore, at lower annealing temperatures, the time taken for full crystallization of the perovskite film increases significantly, making device production at lower temperatures impractical. We have produced high quality perovskite active layer films at low temperatures with the assistance of supercritical carbon dioxide ($scCO_2$). Carbon dioxide (CO_2) above critical point: 31℃, 1071psi, serves as a non-solvent mobilizer, accelerating the crystallization rate of the film at low temperatures and assisting in the removal of residual solvent. We also discovered that $scCO_2$ in combination with organic cosolvents may have selective interactions with one or both precursor compounds, resulting in a variety of film morphologies ranging from uniform films with large grains to films with large cubic and hexagonal crystals.

By annealing the perovskite layer in the presence of $scCO_2$, perovskite-based solar cells with high power conversion efficiency and stability were developed. Photovoltaic devices were made using perovskite layers that were annealed at 50°C or 100°C, with and without the use of $scCO_2$. In contrast to devices annealed at 50°C without $scCO_2$, the use of $scCO_2$ resulted in as 88 percent improvement in power conversion efficiency (PCE) from 9.17% to 17.22%. The use of $scCO_2$ compared to those thermally annealed resulted in a smaller (3%) increase in PCE for devices annealed at 100°C from 16.94% to 17.52%. Understanding the degradation mechanisms will lead to subsequent stability enhancement strategies of using post-deposition annealing with supercritical fluids. Moisture stability of $CH_3NH_3PbI_3$ perovskite solar devices processed with $scCO_2$ is also detailed.

X-ray diffraction, scanning electron microscopy, and optical absorption were used to assess the consistency of the perovskite layer at each annealing condition. The quality of the photoactive perovskite layer corresponded to better PCE. The perovskite layers annealed in $scCO_2$ exhibited higher smoothness, larger average grain size, higher crystallinity and improved optical absorption. $ScCO_2$ is a low-cost, abundant, environmentally green solvent with a low critical pressure and temperature and is an excellent candidate for scalable low temperature production of perovskite-based solar cells.

CHAPTER 1

INTRODUCTION

1.1 Energy

Energy is key in survival, development, and sustainability of any country or economy. The amount of energy consumed per capita is linked to a country's growth. For example, total primary energy consumption in the United States was about 100 quads in 2018, accounting for around 17% of global primary energy consumption. However, in 2018, the United States' population share of the global population was below 4%. Another indicator of the intensity of energy demand is how effectively an economy uses energy to generate every dollar of Gross Domestic Product (GDP). Between 1949 and 2019, the amount of energy used per actual 2012 dollar of GDP in the United States decreased in several years. Though the growth of US energy consumption is affected by GDP and other economic factors, it is also influenced by improvements in energy efficiency and other economic changes that result in lower energy consumption per unit of economic production [1].

Primary and secondary energy, renewable and nonrenewable energy, and fossil fuels are some of the many forms and sources of energy generated and consumed in the United States. The primary energy sources are fossil fuels (petroleum, natural gas, and coal), nuclear energy, alternative energy sources, and others. Figure 1.1 depicts the trend in primary energy use in the United States by energy source from 1950 to 2019. Electricity is a secondary energy supply that is generated by converting primary energy sources into electricity. The demand for energy continues to rise, but most non-sustainable energy sources (such as oil, natural gas, coal, and other fossil fuels) have finite potential. Furthermore, some of them have a negative impact on the climate,

environment and health. As a result, there is a need for electricity supplies that are both renewable and low-polluting. Renewable energy sources may be an option, but the costs of harnessing energy from these sources are already too great [2].
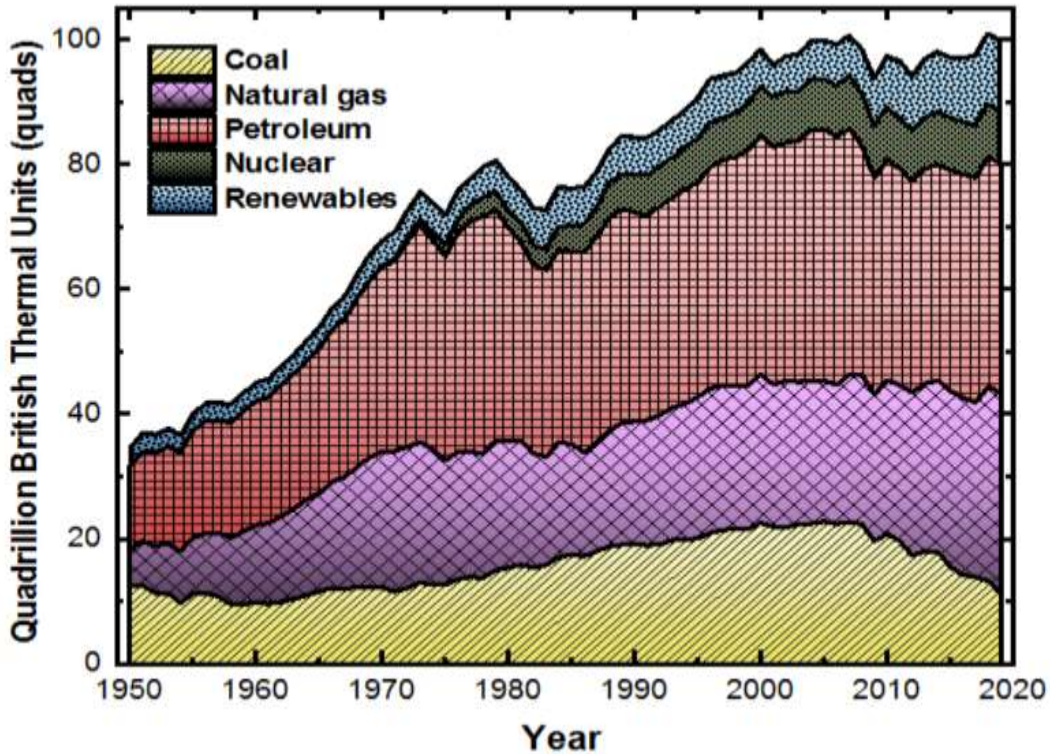
Figure 1.1: The yearly U.S primary energy consumption by major sources from 1950 to 2019. Data acquired from [2].

1.2 Renewable Energy

Renewable energy comes from naturally replenishing yet flow-limited sources; renewable supplies are nearly inexhaustible in terms of length but have a finite amount of energy available per unit of time. They have achieved popularity as a result of their long-term viability and low environmental effects. With increasing energy demand and depleting fossil fuel reserves, a focus on developing environmentally sustainable energy systems and expanding renewable energy penetration has been placed. Energy integration systems that can meet energy demands in different

2

forms are considered a viable approach in this regard for increasing the use of renewable resources

and improving generation performance [3].
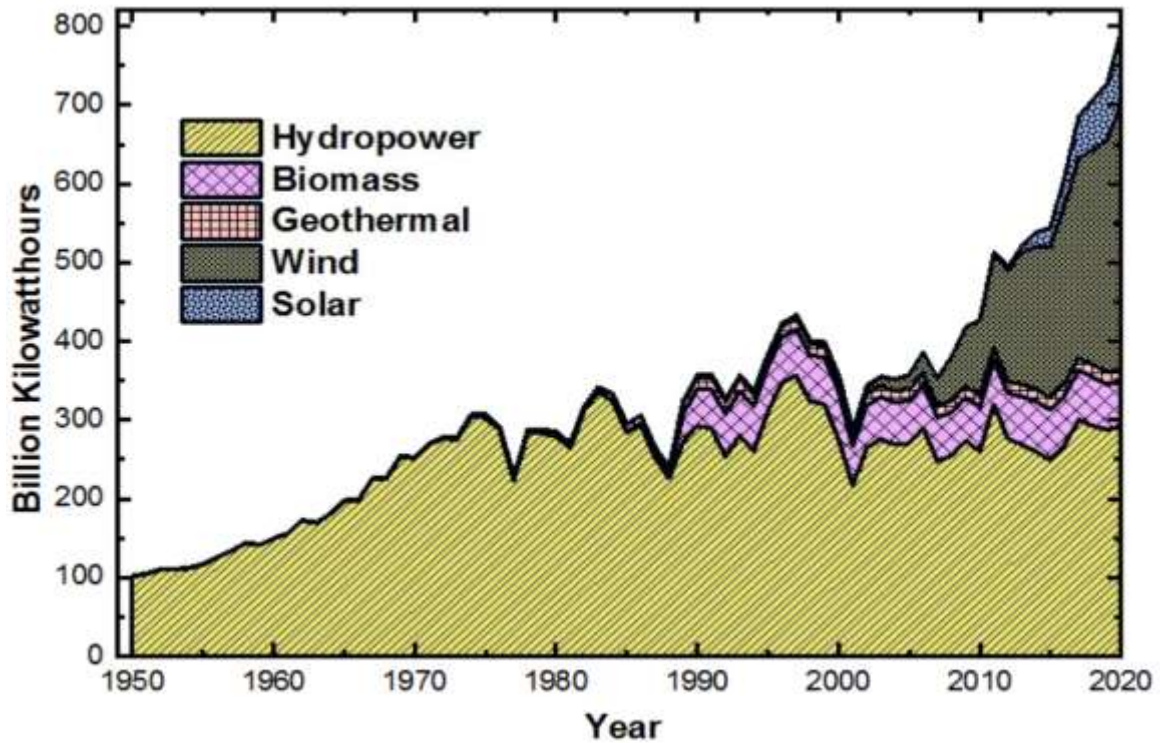
Figure 1.2: U.S electricity generation from renewable energy sources from 1950 to 2020. Data

acquired from [4]

Figure 1.2 depicts the patterns of different renewable energy sources in the United States

over time. Renewable energy accounted for about 11.4 percent of overall energy demand in the

United States, owing primarily to record-high solar and wind energy generation. Because of lower

precipitation levels, mostly in the western United States, hydroelectric power generation in 2019

was around 12% lower than the 50-year average. The total volume of biomass produced and used

in 2019 was marginally lower than in 2018, which saw the highest amount of biomass output and

usage since at least 1950. In 2019, geothermal energy usage was around 2% lower than the peak in 2014 [4].

Biofuels, geothermal, solar, and wind energy demand in the United States was almost three times higher in 2019 than it was in 2000. Renewable technology has the potential to significantly reduce greenhouse gas emissions. Renewable energy can help to reduce the use of fossil fuels, which are the primary source of CO_2 emissions in the United States. Renewable energy demand in the United States is expected to rise through 2050, according to the US Energy Information Administration [4]. Solar energy is increasingly expanding in terms of potential, despite the fact that hydropower and wind energy sources are dominant in the renewable energy space. [5].

1.3 Solar Photovoltaics

Electromagnetic waves carry solar radiation from the sun to the earth. Even if only a small portion of the sun's energy enters the planet, it is adequate to fulfill the world's energy needs. It has the advantages of being abundant in nature, environmentally friendly, and a sustainable and reliable energy source. Solar panels have a low maintenance cost, the technology does not contribute to noise pollution and provides energy security [6]. Solar energy has a theoretical power output of about 2300 TW/year, compared to the world's power generation of about 16 TW/year. However, solar energy accounted for 2.4% of global electricity production [7].

Photovoltaics is the method of transforming solar energy into electricity. Photovoltaic solar cells are the leading technology for sustainable, renewable energy, yet to compete with and replace non-renewable sources of energy, fabrication costs must be lowered and efficiencies increased [8] [9]. Thin film solar cells such as Cadmium Telluride, Gallium Arsenide, Copper Indium Gallium Selenide, organic, dye-sensitized [10], graphene, carbon nanotube [11], quantum dot solar cell

4

[12], and perovskite solar cells [13] have been documented to have higher efficiencies than the conventional silicon solar photovoltaics. Due to their high absorption coefficient, long charge diffusion duration, high carrier stability, bandgap tunability, high tolerance for defects, and solution processing, organic-inorganic halide perovskite solar cells (PSCs) have emerged as a possible candidate for high performance, low-cost renewable energy source [14] [15] [16] [17] [18]. Perovskite-based devices' power conversion efficiency (PCE) has risen dramatically from 3.8 percent in 2009 to 25.2 percent in 2019 [19].

1.4 Thesis Outline

Chapter two describes the basic semiconductor device physics including band structure of solids, p-n junction of solar cells, solar cell circuit model, and solar cell efficiency. In addition, a brief background of perovskite solar cells with details of the fundamentals of crystallization and supercritical fluids are included. In chapter three, a detailed report on the use of $scCO_2$ in annealing $CH_3NH_3PbI_3$ perovskite thin films is documented. Here, varying some parameters of $scCO_2$ (pressure, time, temperature) is used to determine its effect on the morphology of the perovskite film. In chapter four, the use of $scCO_2$ plus organic solvent to form a single-phase $scCO_2$ + cosolvent for annealing perovskite films is introduced. Here, varied cosolvents with different solubility and strength of their Hydrogen bond are used to investigate the strength of $scCO_2$ + cosolvent on the morphology of the perovskite film. Chapter five details the Current–Voltage (I-V) characteristics of perovskite solar cells with the active layer annealed with $scCO_2$. Thermal annealed active layers are also reported for comparison. Finally, in chapter six, the stability of perovskite devices processed with both thermal annealing and $scCO_2$ with an increase in humidity is reported.

References

1. U.S. Energy Information Administration, Use of energy explained, (2020). https://www.eia.gov/energyexplained/use-of-energy/

2. U.S. Energy Information Administration, U.S. energy facts explained (2020). https://www.eia.gov/energyexplained/us-energy-facts/

3. A. V. Rosa, J. C. Ordonez, Fundamentals of Renewable Energy Processes, Academic Press (2022) 1 – 46. doi.org/10.1016/B978-0-12-816036-7.00010-5

4. U.S. Energy Information Administration, Renewable energy sources, (2021). https://www.eia.gov/energyexplained/renewable-sources/

5. J. Mohtasham, Review Article – Renewable Energies, International Conference on Technologies and Materials for Renewable Energy, Environment and Sustainability, 74 (2015) 1289 – 1297. doi.org/10.1016/j.egypro.2015.07.774

6. R. Perez, M. Perez, A fundamental look at energy reserves for the planet, IEA/SHA Solar update, (2009) 1 – 3.

7. Renewables 2019 Global Status Report, Paris: REN21 Secretariat, page 41

8. R. D. Fan, Y. Huang, L. Wang, L. Li, G. H. J. Zheng, H. Zhou, The Progress of Interface Design in Perovskite-Based Solar Cells, Adv. Energy Mater., 2016, 1600460

9. F. Li, M. Liu, Recent efficient strategies for improving the moisture stability of perovskite solar cells, J. Mater. Chem. A, 5 (2017) 15447-15459.

10. M. A. Green, K. Emery, Y. Hishikawa, W. Warta and E. D. Dunlop, Solar cell efficiency tables (Version 45), Prog. Photovoltaics, 23 (2015) 1–9.

11. K Cui, S Maruyama, Multifunctional graphene and carbon nanotubes films for planar heterojunction solar cells, progress in energy and combustion science, 70 (2019) 1-21

12. Q. Wu, H. Zhao, F. Huang, J. Hou, H. Cao, Z. Liu, S. Peng, G.Cao, Impacts of Reduced Graphene Oxide in CdS/CdSe Quantum Dots Co-sensitized Solar Cells, J. Phys. Chem. C, 121 (2017) 18430-18438.

13. A. Miyata, A. Mitioglu, P. Plochocka, O. Portugall, J.T.W. Wang, S.D. Stranks, H.J. Snaith, R.J. Nicholas, Direct measurement of the exciton binding energy and effective masses for charge carriers in organic-inorganic tri-halide perovskites, Nat. Phys., 11 (2015) 582–587.

14. M.M Lee, J Teuscher, T Miyasaka, T. N Murakami, J.J Snaith, Efficient Hybrid Solar Cells Based on Meso-Superstructured Organometal Halide Perovskites, Science (80-.). 338 (2012) 643–647. doi:10.1126/science.1228604.

15. G.E. Eperon, S.D. Stranks, C. Menelaou, M.B. Johnston, L.M. Herz, H.J. Snaith, Formamidinium lead trihalide: A broadly tunable perovskite for efficient planar heterojunction solar cells, Energy Environ. Sci. 7 (2014) 982–988. doi:10.1039/c3ee43822h.

16. S.D. Stranks, G.E. Eperon, G. Grancini, C. Menelaou, M.J.P. Alcocer, T. Leijtens, L.M. Herz, A. Petrozza, H.J. Snaith, Electron-Hole Diffusion Lengths Exceeding Trihalide Perovskite Absorber, Science (80-.). 342 (2013) 341–344. doi:10.1126/science.1243982.

17. C. Kim, S. Ryu, J. Seo, S.I. Il Seok, W.S. Yang, J.H. Noh, N.J. Jeon, Y.C. Kim, S. Ryu, J. Seo, S.I. Il Seok, High-performance photovoltaic perovskite layers fabricated through intramolecular exchange, Science (80-.). 348 (2015) 1–12. doi:10.1126/science.aaa9272.

18. K.X. Steirer, P. Schulz, G. Teeter, V. Stevanovic, M. Yang, K. Zhu, J.J. Berry, Defect Tolerance in Methylammonium Lead Triiodide Perovskite, ACS Energy Lett. 1 (2016) 360–366. doi:10.1021/acsenergylett.6b00196.

19. NREL, Best Research-Cell Efficiency Chart, (2019). https://www.nrel.gov/pv/cell-efficiency.html.

CHAPTER 2

BACKGROUND

2.1 Solar Cell Physics

The photovoltaic effect allows photovoltaic devices or solar cells to transform light directly into electricity. This effect is based on photon absorption by a photoactive material, which generates electrons and holes, which are then spatially divided by the device's intrinsic asymmetry. This generates an electrical current as well as a potential difference, allowing the device to power an external circuit [1].

2.1.1 Band Structure of Solids

According to quantum mechanics, electrons in an atom exist in orbitals described by four quantum numbers, each of which satisfies the Schrodinger equation and has a well-defined energy. According to the Pauli Exclusion Principle, no two electrons should share all four quantum numbers, so electrons fill these orbitals in order of decreasing energy. Atom interactions are determined by the occupancy and form of these orbitals. The electron orbitals are represented as probability density clouds characterized by wave functions rather than particles with known position and momentum due to the Heisenberg Uncertainty Principle [2] [3] [4].

Independent atomic orbitals join to form molecular orbitals as two atoms are pulled together to form a molecule. When the wave functions of the molecular orbitals are in transition, a bonding orbital with a lower energy is formed. If they are out of phase, however, an antibonding orbital with a higher energy than the original atomic orbital is created. Figure 2.1 depicts this phenomenon, from the s-like and p-like atomic states to the p bonding and anti-bonding orbitals of the molecules. Finally, when a large number of atoms are brought together to form a solid, a

8

large number of new energy levels are created, resulting in a band-like spectrum of energy states. The atoms' s and p states combine to form bonding and anti-bonding molecular orbitals, which develop into the semiconductor's conduction and valence bands. and valence bands respectively. Conduction and valence bands are the highest and lowest populated bands, respectively. The band distance (E_g) is the energy difference between the bands [2].
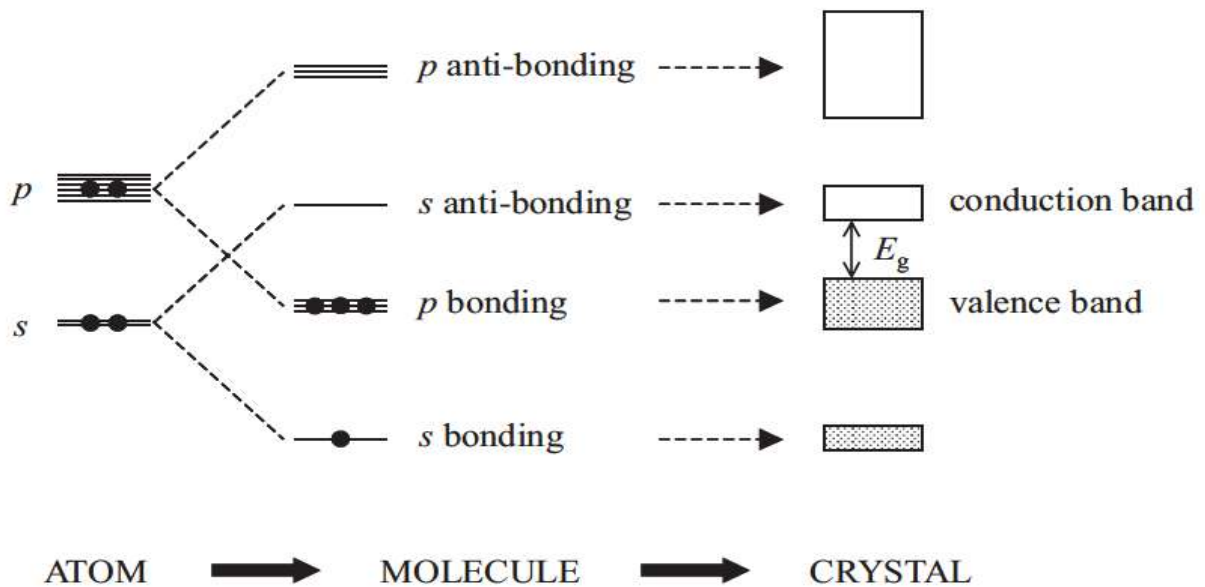
Figure 2.1: Schematic diagram of the electron levels in a covalent crystal made from four-valence atoms such as germanium or binary compounds such as gallium arsenide [2].

If the selection rules allow it, interband transitions between these bands would be feasible. During the transition, an electron absorbs a photon and moves from the lower energy band to the higher energy band. This will only happen if an electron is in the lower band's initial state. Furthermore, the Pauli Exclusion Principle requires that the upper band's final state be void. A photon, for example, excites an electron from a filled valence band to the empty conduction band of semiconductors and insulators. The conductivity of a solid is determined by the size of the band difference. Electrons can be excited into the conduction band more easily with smaller band

distances, resulting in higher conductivity. Solids with band gaps of 0.5 to 3eV are known as semiconductors, and those with band gaps of greater than 3eV are classified as insulators. [1] [2] [3] [4] [5].

Solid-state physics can theoretically explain the creation of bands by using Bloch functions to solve the Schrodinger equation for a periodic potential [5]. The Interband absorption rate depends on the band structure of the solid, whether direct or indirect. Figure 2.2 shows the Energy (E) – Momentum (k) diagram of a solid with a direct and indirect band gap. In the Brillouin field, the difference is between the relative locations of the conduction band minimum and the valence band limit. Both occur at the zone center where k = 0 in a direct gap material. The conduction band minimum in an indirect gap material, on the other hand, does not exist at k = 0, but rather at a different value of k, which is normally near the zone edge or close to it. The difference in the band gap's structure has significant implications for optical and electrical properties. To retain momentum, electrons cannot leap through indirect band gaps solely by absorption of photons; the transfer must also have a phonon. This complicates indirect band holes, such as those found in silicon [2] [4] [5].

Since electron states in real crystals are distinct and only a finite number of states occur within each energy band, the curves in the E-k diagram may be misleading. The actual number of electrons in a band is limited by the number of available states. Since there will be one electron with a negative wave number -k for every electron with a positive wave number k, a filled energy band will not result in electrical conductivity. Inside the band, this results in a net electron wavenumber of zero. And if an electric field is applied to the sample, there is no net electron momentum and hence no net electron flux. If the filled band is no longer complete and the empty

band is no longer empty, electrons may be promoted through the energy gap E_g by thermal or optical energy, resulting in electrical conduction [6].
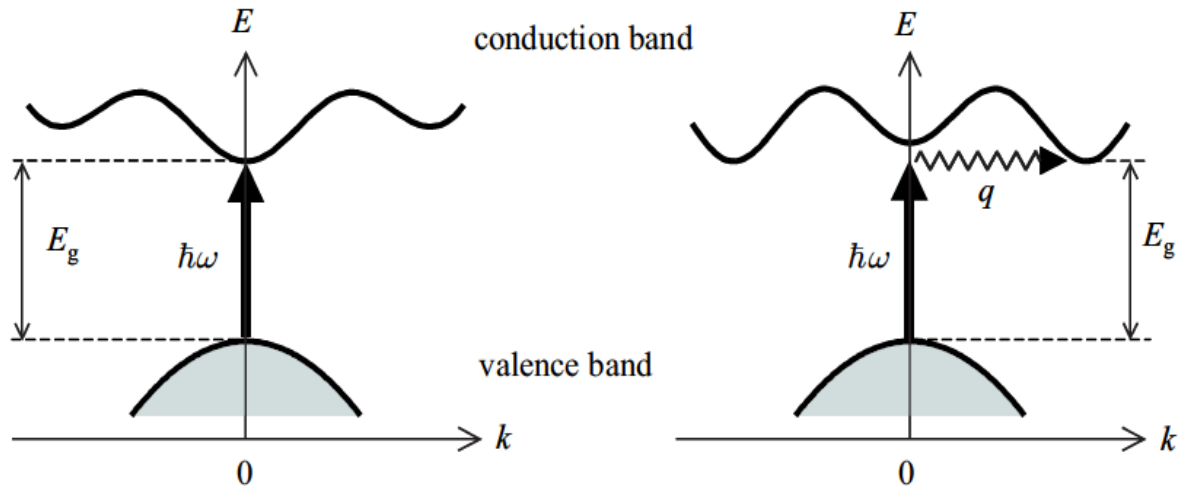
Figure 2.2: Interband transitions in solids direct band gap and indirect band gap. The vertical arrow represents the photon absorption process, while the wiggly arrow represents the absorption or emission of a phonon [2].

2.1.2 The p-n junction of solar cells

The room temperature diagram of a semiconductor in thermal equilibrium is seen in Figure 2.3. The Fermi energy is an imaginary horizontal line of energy E_f. This energy is described as the energy above which the probability of electron states being filled is less than 50% and below which the probability is greater than 50% [3]. Holes are the empty states in the valence band. Electron conductivity involves both valence band holes and conduction band electrons. Intrinsically semiconductors are pure semiconductors. Extrinsic semiconductors are formed when low amounts of impurity atoms are incorporated into a semiconductor, and the impurity type and concentration influence the electron and hole concentrations [5]. In n-type semiconductors, donor impurities

contribute electrons to the conduction band, while acceptor impurities donate holes to the valence band. Carriers with a low concentration in a certain semiconductor region are known as minority carriers, whereas carriers with a slightly higher concentration in the same region are known as majority carriers [6].
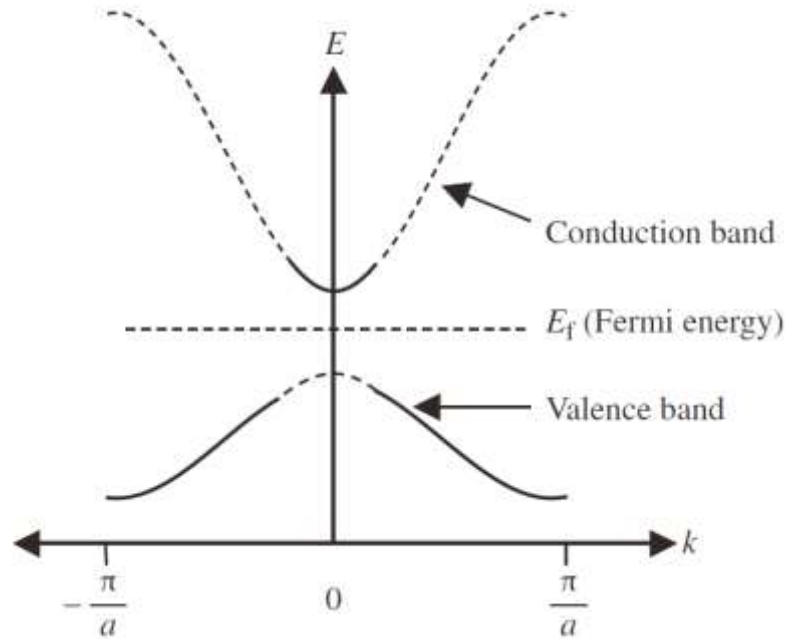
Figure 2.3: Room temperature semiconductor showing the partial filling of the conduction band and partial emptying of the valence band [6].

Bringing the p-type and n-type semiconductor together forms a p-n junction. The key components of a p-n junction diode include a metal anode, a p-type semiconductor, a p-n junction, a n-type semiconductor, and a metal cathode. Figure 2.4 shows how light enters the p-n junction and reaches the depletion region of the solar cell to generate electron-hole pairs. Minority carriers can drift through the depletion zone to become majority carriers in the n-majority and p-majority, resulting in drift currents. The presence of an electron and hole concentration gradient also drives diffusion currents, as majority carriers diffuse to the minority side [1] [2] [6].
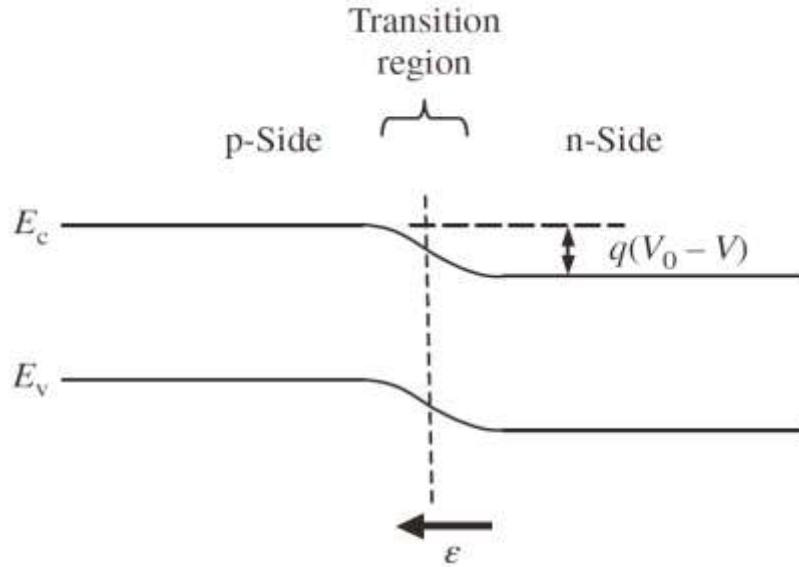
Figure 2.4: Diode band model with the application of a forward bias [6]

As seen in Figure 2.4, the band slope is induced by an electric field called a built-in electric field (qV_o), which occurs in the transition area of the p-n junction even though no external voltage is applied. The available energy can be exploited by lowering the potential barrier $q(V_o-V)$ that is needed to allow carrier drift across the depletion area. The semiconductor band gap is reduced by subtracting the magnitude of $q(V_o-V)$, reducing the usable energy distance between electrons and holes moving in n-type and p-type semiconductors, respectively. The solar cell's working voltage is reduced as a result of this. Excessive diffusion current will flow in the opposite direction of the desired drift current if $q(V_o-V)$ is too small [5] [6].

2.1.3 Solar Cell Circuit Model

The equivalent circuit of a solar cell using a single diode is shown in Figure 2.5. A solar cell can be represented in this way by a single diode, a current source in parallel with the diode

that represents the photo-generated current, and series and shunt resistance. Higher load resistance causes the diode to conduct more current, resulting in a greater potential gap between the terminals. Less resistive load, on the other hand, results in more current flowing into the external circuit. The current derived from a solar cell from an external load can be calculated as follows,

$$I = I_L - I_o \left[\exp\left(\frac{qV}{nkT}\right) - 1 \right] - \frac{V + IR_s}{R_{sh}} \qquad (2.1)$$

Where I_L is the photo-generated current, I_o is the reverse saturation current of the diode, n is the ideality factor of the diode, R_s and R_{sh} are series and shunt resistance respectively and V is the applied voltage across the solar cell [6].
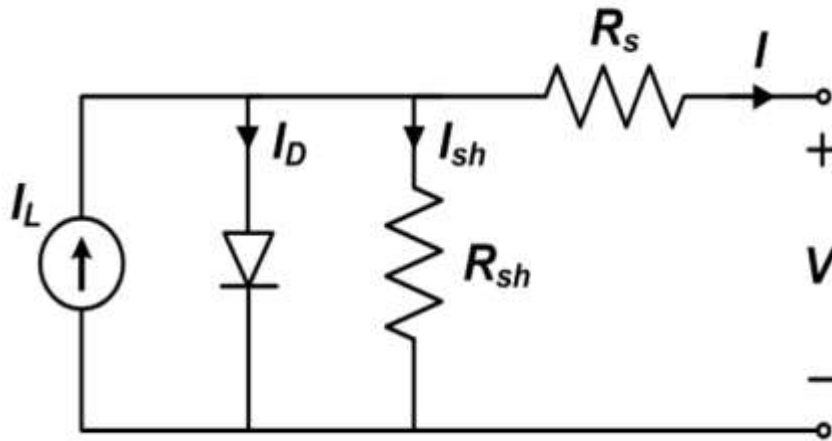
Figure 2.5: The equivalent circuit of a solar cell using a single diode model [7]

A two-diode model is normally used to characterize the solar cell accurately along with various sorts of recombination. With exposure to illumination, the current from the solar cell is given by,

$$I = I_L - I_{01} \left\{ \exp\left[\frac{q(V + IR_s)}{kT}\right] - 1 \right\} - I_{02} \left\{ \exp\left[\frac{q(V + IR_s)}{2kT}\right] - 1 \right\} - \frac{V + IR_s}{R_{sh}}. \qquad (2.2)$$

14

Two diodes are due to two types of recombination within the solar cell's bulk: band-to-band and trap-assisted recombination. The diode current is proportional to $e^{\frac{qV}{2kT}}$ at low bias around the device during low-level injection while the device is still depleted, where the ideality factor of the diode is 2. The diode current is proportional to $e^{\frac{qV}{kT}}$ at higher bias around the device with high-level injection, where the ideality factor of the diode is 1. The photo-generated current is negative under illumination until the bias is high enough for a positive current to flow through the device [7].

2.1.4 Solar Cell Efficiency

Place, time of year, weather conditions, and the orientation of the sun in the sky all affect solar irradiance. Devices are illuminated with the Air Mass 1.5 (AM 1.5) range for standardization of measuring solar cells, which corresponds to the sun at a zenith angle of 48.2° at an intensity of $1000 \mathrm{Wm}^{-2}$ [1] [2] [6]. The device's current is produced by changing the voltage across it, and the current density is widely reported. The current density of a solar cell measured under AM 1.5 illumination is seen in Figure 2.6, along with the normal diode reaction expected by the diode equation. If there is no applied bias, the maximum current or short circuit current (J_{sc}) occurs, resulting in a short circuit. At the open-circuit voltage (V_{oc}), the device's current reduces until it approaches zero. As seen in Figure 2.6, the device's output power is determined by multiplying the current and voltage at each point. The highest power point is reached as power reaches its height. The power conversion efficiency (η) can be determined as,

$$\eta = \frac{J_{mp}V_{mp}}{P_s} \tag{2.3}$$

Where J_{mp} and V_{mp} are the current and voltage at the maximum power point. Multiplying them will yield the maximum power point. P_s is the incoming power density of light ($1000 Wm^{-2}$). In addition, the maximum power point can be related to the V_{oc} and J_{sc} by the fill factor (FF) as,

$$FF = \frac{J_{mp}V_{mp}}{J_{sc}V_{oc}} \qquad (2.4)$$
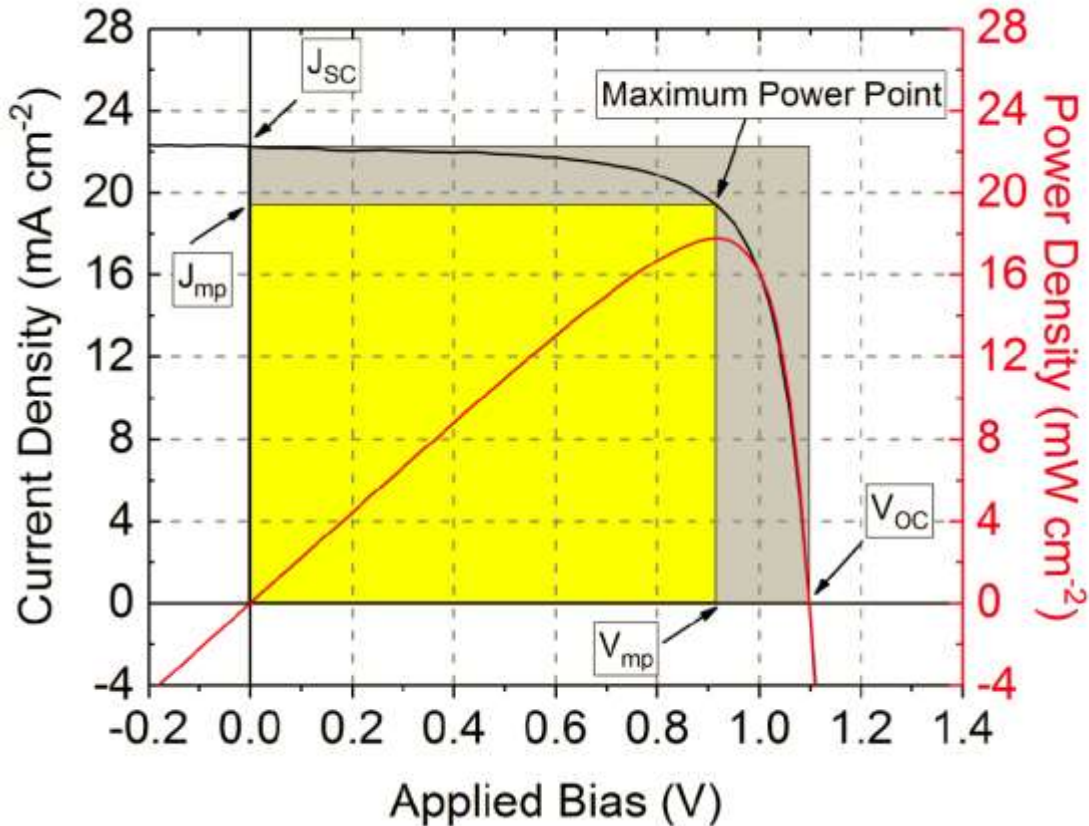
Figure 2.6: Plot of Solar Cell Current-Voltage characteristics [8]

As seen in Figure 2.6, an ideal system with no parasitic losses would have a fill factor of 100 percent, but actual devices have lower fill factors due to series and shunt resistance. The gradient of the curve at the open-circuit will decrease as series resistance in devices increases, decreasing the device's maximal power point and FF. The gradient of the curve at the short circuit

16

will become progressively negative as the device's shunt resistance decreases, lowering the FF. The combination of Equations 2.3 and 2.4, four metrics are used to measure device performance,

$$\eta = \frac{J_{sc}V_{oc}FF}{P_s} \qquad (2.5)$$

2.2 Perovskite Solar Cells

2.2.1 Perovskite material
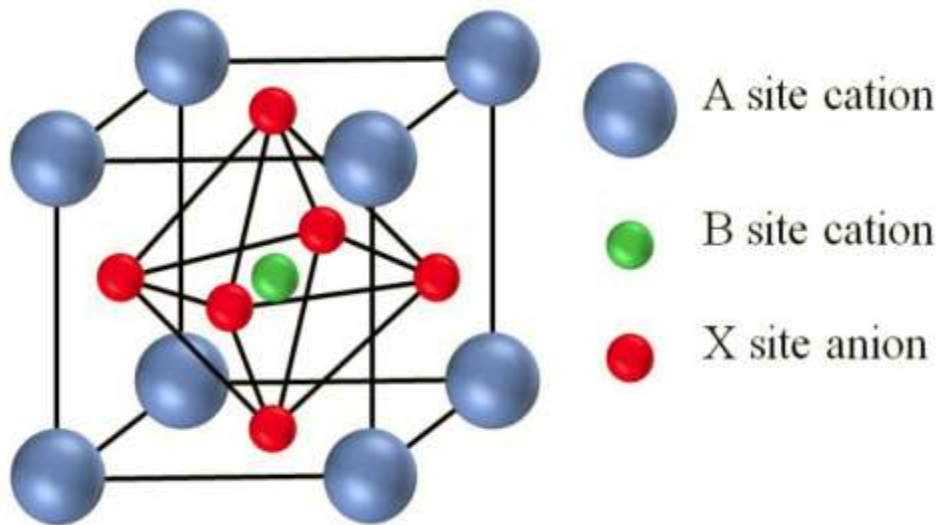
Figure 2.7: Diagram of perovskite crystal structure [8]

The crystal structure of perovskite is that of calcium titanate ($CaTiO_3$). Perovskite refers to the ABX_3 structure (usually A is organic ammonium such as methylammonium, B is a cation such as lead and X is a halide such as chlorine, or mixed halides) having PCE from 3.8% in 2009 [9] to a certified record of 25.5% in 2019 [10]. The typical crystal structure of perovskite is shown in Figure 2.7. The most efficient monolithically combined perovskite-silicon tandems have a 26 percent efficiency [11]. Oxford PV recently released a 29.5 percent PCE certified

perovskite/silicon tandem solar cell [12]. Perovskite also has a strong absorption coefficient [13], a low exciton binding energy [14], a high carrier mobility [15], a broad carrier diffusion length [16], band gap tenability [17], and a high defect tolerance [18], making it an optoelectronic material uniquely suitable for use in photovoltaic devices.
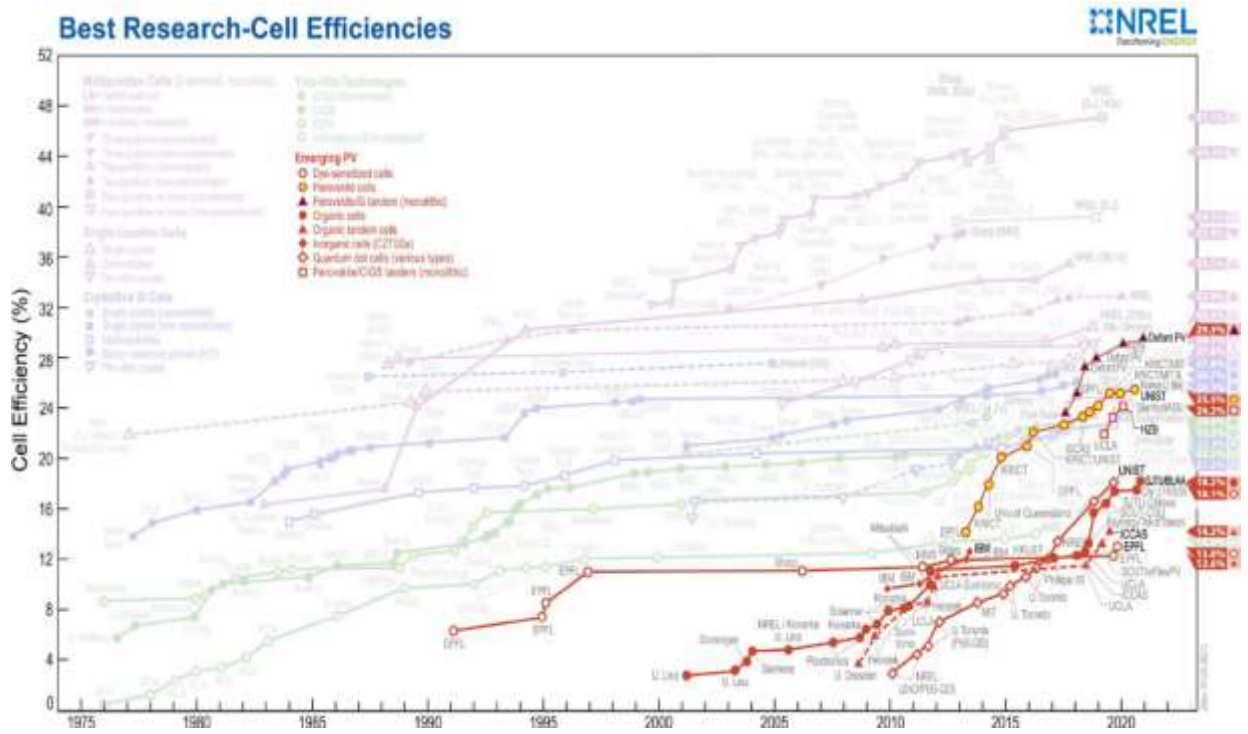
Figure 2.8: Comparison of perovskite solar cells with different emerging solar PV technologies

[10]

Organic-inorganic hybrid perovskite solar cells have a high power conversion efficiency (PCE) and low-cost solution-based processing, making them a promising candidate for low-cost renewable energy. Figure 2.8 depicts the best research-cell efficiencies of different new solar cells, as well as perovskite solar cells' exponential development [10]. In terms of perovskite solar cells, the potential is enormous. Perovskite compounds, on the other hand, have certain drawbacks, such

18

as poor durability while exposed to moisture, rising temperatures, and ultraviolet radiation. Due to these drawbacks, perovskite solar cells degrade more quickly than silicon solar cells. Lead is also used as a perovskite material. During the fabrication and disposal procedures, the toxicity of Pb^{2+} ions on the atmosphere and the human body is also an issue. To mitigate toxicity, lead in PSCs is now substituted with elements such as Tin [19] [20] [21].

Perovskites have a high absorption coefficient since they are also direct band gap semiconductors [22]. However, there is some evidence that some perovskites may show a marginally indirect band gap by Rashba Splitting due to the rotation of methylammonium cations [22] [23]. By blocking radiative recombination, this is expected to increase charge carrier lifetimes. Perovskites have been shown to have carrier mobility as high as 17.8 cm^2/(V.s) [24] [25], with remarkable diffusion distances exceeding 100 microns in single crystals [26]. The crystal structure of perovskite films is expected to contain a significant number of vacancy and interstitial defects [27]. Many of these deficient states, fortunately, exist beyond the band gap, preventing them from functioning as non-radiative recombination centers [28]. This explains why PSCs have such low voltage losses, with the best instruments showing open-circuit voltages just 400 mV below the band gap [29] [30]. These properties allow hundreds of nanometer-thick polycrystalline films to absorb photons and pass charge efficiently.

2.2.2 Architecture of Perovskite Solar Cells

There are two types of PSC architecture as shown in Figure 2.9. The first is the n-i-p type, an n-type or electron transport layer (ETL) while the second is a p-i-n, a p-type or hole transport layer (HTL). Examples of n-type materials are TiO_2 and ZnO and spiro-OMeTAD for p-type [31] [18]. For the n-i-p device, light penetrates through the ETL into the perovskite layer whereas, for the p-i-n, light passes through the HTL (E.g. NiO and PEDOT: PSS). Perovskite solar cell consists

of six layers namely; substrate, the perovskite absorber layer, ETL, HTL, bottom contact (metal electrode), and top contact (transport conducting layer). The perovskite material is the absorbing layer, which is crammed between ETL and HTL. The conductivity and charge transfer are determined by the doping concentration in the transport layer. To fabricate highly efficient PSCs, the ETL must have a low work function, a low recombination rate, and a high conductivity. To extract holes, the HTL is present between the light-absorbing substrate and the metal electrode [9] [31] [32] [33].
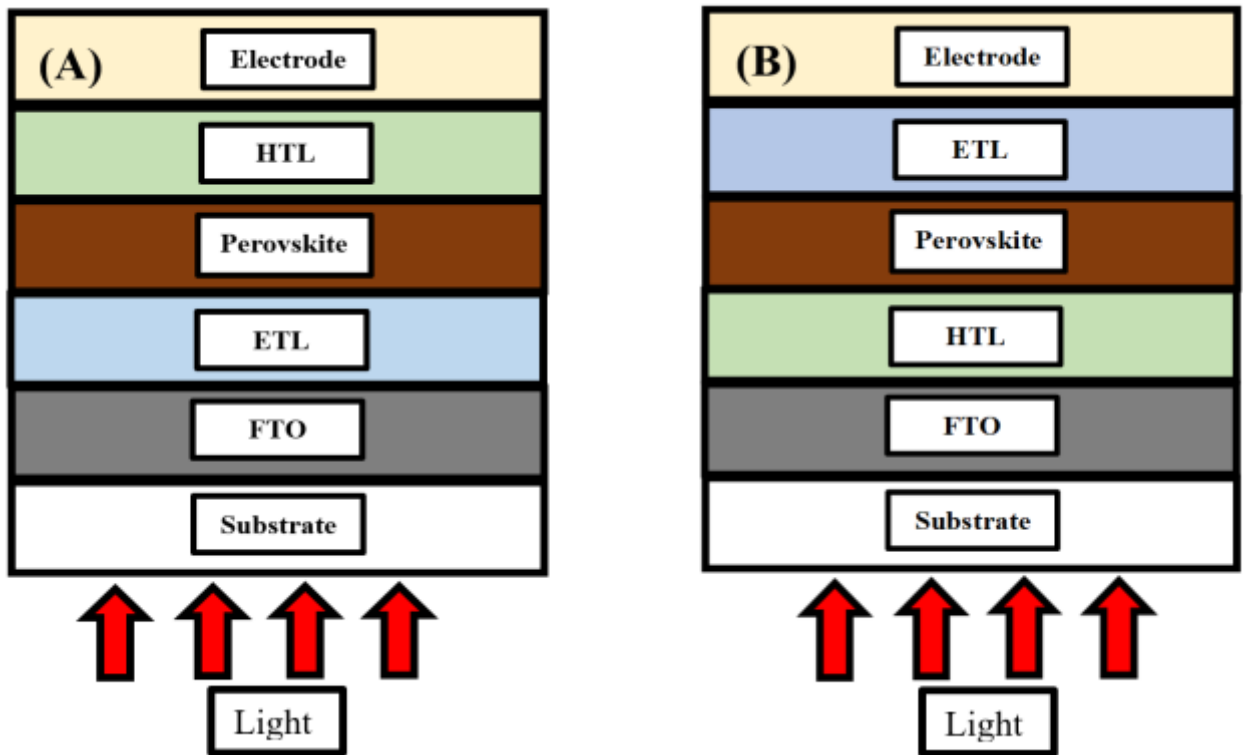
Figure 2.9: (A) n-i-p type perovskite solar cell architecture (B) p-i-n type perovskite solar cell architecture.

PSC structure should be chosen for high stability, low recombination, easy charge transfer, and no direct interaction with the perovskite and the metal contact. During the solar cell fabrication

20

phase, planar, mesoscopic, or nanostructured layers of ETM and hole transport materials are deposited. Conducting polymers are used in a wide range of applications, including photovoltaics, flexible or portable electronics, displays, and other electronic instruments. Due to poor intermolecular overlap of electronic orbitals and a higher degree of disorder, these polymers behave as semiconductors with a special charge transfer rate, narrow electronic band gap, and limited charge carrier mobility. Polymers are a good candidate for solar cell fabrication as ETL or HTL materials because of these properties. PCBM, PEDOT:PSS, P3HT, and other conducting polymer ETL and HTL products [9] [31] [33].

2.2.3 Solution Processing

One of the reasons for the eclectic interest in PSCs is their solution and vapor processability. There are several ways of producing perovskite thin films. Some of these techniques are described and shown in Figure 2.10. One-step solvent deposition: An organic and inorganic solution is coated on a layer, accompanied by annealing to form perovskite. It is both inexpensive and simple to execute. However, its low film quality limits production, and the solvent options for simultaneously dissolving both components are minimal [34] [35]. Two-step solvent-based processing: an inorganic component solution is deposited on a layer, followed by an organic component solution coating (or immersion) and annealing. As compared to one-step approaches, this produces better photovoltaic efficiency. However, compared to vacuum methods, there is less power over film thickness [36] [37] [38] [39] [40].

Dual-source vapor deposition: Co-evaporation of organic and inorganic elements followed by annealing. They form greater film uniformity than solution methods, resulting in higher efficiencies. However, the vacuum process needs a lot of resources, and it's difficult to regulate the deposition speeds of both components at the same time [41] [42]. Sequential vapor deposition

21

creates a bilayer coating of inorganic and organic elements, which is then thermally annealed to form perovskite. They remove the issues associated with one-step deposition [43] [44]. However, the vacuum process necessitates a large amount of energy, raises costs, and limits mass manufacturing. Process of vapor-assisted solution: The inorganic component is deposited first, followed by an increased temperature exposure to the organic component vapor. The integration of vapor and solution-based methods produces higher-quality films [45] [46] [47] [48]. The vacuum mechanism, on the other hand, necessitates a lot of electricity.
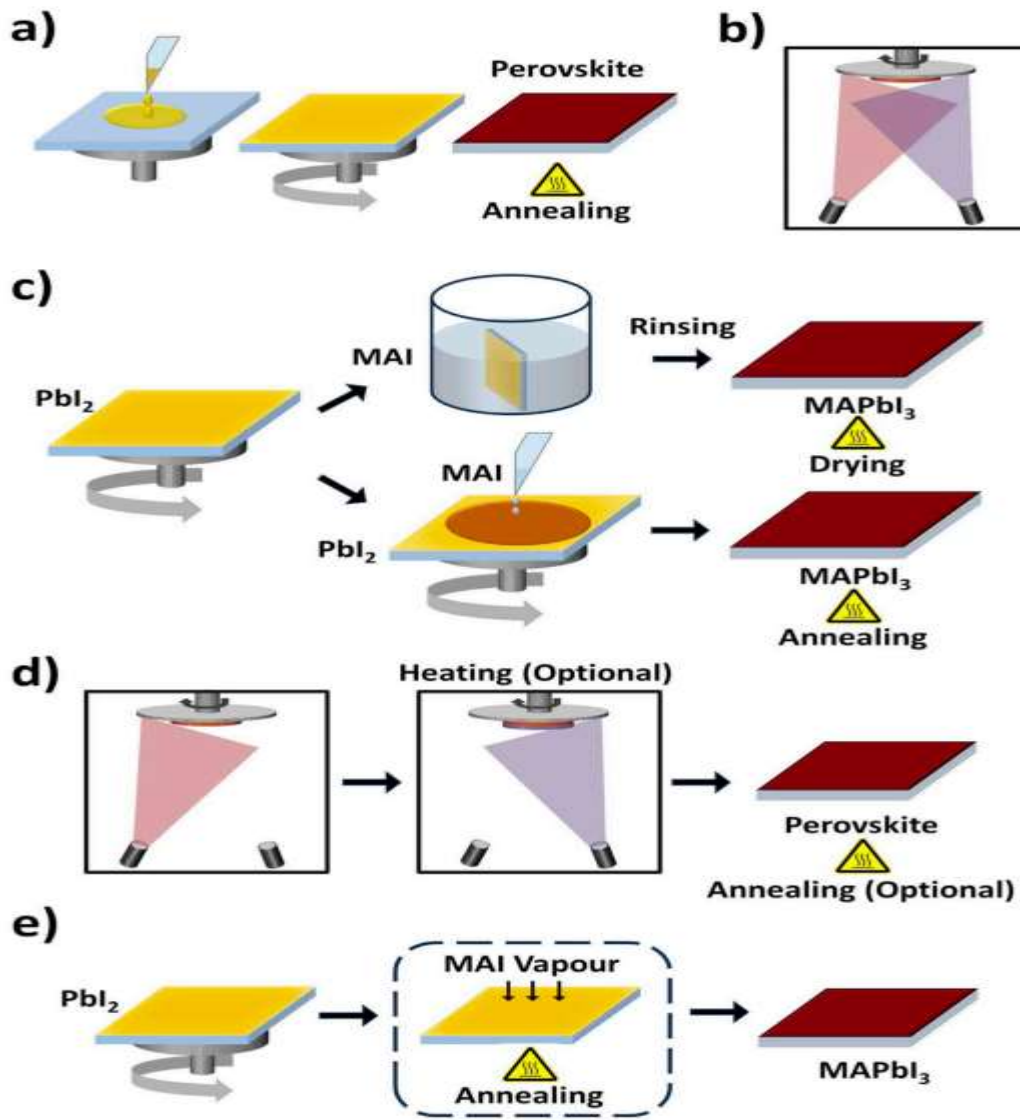
Figure 2.10: Demonstration of varied perovskite deposition methods a) solution-based one step method b) co-evaporation c) solution-based two-step method d) sequential evaporation e) vapor-assisted solution process (VASP) [49].

Spin coating is commonly used for lab-scale applications, resulting in narrow areas with high efficiency PSCs. A small amount of solution is applied to the layer, which is then accelerated to several thousand revolutions per minute (rpm). A hydrophilic surface is required for greater uniformity, and the shear forces caused by the substrate's rotation allow the precursor to scatter over the surface, leaving behind a thin layer. Post-deposition annealing is used to obtain solid-state crystallization and solvent elimination from the film. The final thickness of the is approximated by [50],

$$ t = \frac{1}{\sqrt{\omega}} \tag{2.6} $$

Where t is the thickness of the resultant film and ω is the spin speed. Equation 2.6 is a simple correlation but many researchers use other correlations such as Emsie, Bonner, Peck Model, to predict film thickness without experimental data [51].

2.2.4 Scalability and Stability

Organic-inorganic hybrid perovskite materials' special properties and ease of fabrication, as well as their excellent system performance, hold great promise for the efficient commercialization of PSCs. The spin-coating process is currently commonly used in the preparation of PSCs. However, it is difficult to prepare a high-quality perovskite film with a large area, and the precursor solution is only used to a small extent. As a result, it is unsuitable for large-scale industrial development. Despite extensive efforts

to investigate a suitable large-scale fabrication system (including roll-to-roll technique, spray coating, doctor-blade coating, and so on), the PCEs of the manufactured solar cells remain lower than those of spin-coated devices. As a result, it is critical to take steps to improve the PCEs of PSCs produced by upscaling-tolerant deposition processes, particularly given that the output of solar cells is largely determined by the quality of the perovskite crystal films. There have been many scalable investigated approaches including Inkjet printing [52], Slot-die coating [53], Doctor-blade coating [54], Spray coating [55], Brush-painting [56], Electrospray coating [57], and many others (Drop casting, Pneumatic spray coating, hand spray coating, ultrasonic coating) [58].

There are still some challenges to address for the scalable processing of perovskite thin films: low performance of devices with a large active area as well as poor film quality, precursor solutions with uncontrollable reproducibility are usually a complication for commercialization due to high nucleation and growth rates of perovskites crystals, and low raw material usage. As a result, the current focus of perovskite research is on developing dependable equipment and managing precursor solution properties to allow high-quality large-scale manufacturing using low-cost materials, environmentally sustainable processing, effective solution use, and enhanced PCE [58].

Despite their high performance, PSCs have a number of issues, including hysteresis, lead toxicity, and long-term stability deterioration of perovskite crystals at high temperatures, high recombination, and scalability. Long-term stability is the most critical concern with PSCs, owing to the chemical oxidation of perovskite materials in atmospheric conditions. $CH_3NH_3PbI_3$ is the universally used light absorber in PSCs but unfortunately, it shows severe moisture instability. Numerous report show that the $CH_3NH_3PbI_3$ degrades directly to PbI_2 with exposure to both UV irradiation and air. After reaching moisture to the perovskite layer, the color of the perovskite layer changes gradually to yellow because of the decomposition of $CH_3NH_3PbI_3$ into PbI_2, MA, and HI.

It should be mentioned that oxygen and UV radiation can also influence the stability of PSCs, but to a far lesser extent than moisture [59] [60].

So far, the highest efficiency PSCs have been obtained with a lead-based perovskite. Lead, on the other hand, poses a significant danger to human wellbeing and the overall protection of the environment. One of the problems confronting the PSC industry is lead toxicity [61]. Since perovskites are unstable, it is simple to decompose them into a moderately water-soluble carcinogen (PbI_2) in a humid atmosphere or under high UV radiation. It is worth noting that the decomposition procedure is permanent. While proper device encapsulation will effectively control lead toxicity, it can also increase the device's expense. There are lead-based PSCs on the market that are already in compliance with the marketplace's stringent environmental legislation. As a result, low-toxicity perovskite products for PSCs have received a lot of interest. The most powerful approach is to fully replace lead with low toxicity elements such as Sn, Bi, Sb, and Cu, among others.

The most promising non-toxic material for perovskites is a Sn-based halide perovskite ($CH_3NH_3SnX_3$, X = Cl, Br, I). It has a 1.23 eV direct optical band difference. The most difficult thing with a Sn-based halide perovskite is that divalent Sn^{2+} is easily oxidized into the more solid Sn^{4+}, resulting in a high degree of Sn^{4+} doping in Sn-based perovskite films and Sn vacancies [62]. This would result in extreme charge recombination in PSCs. SnF_2 was implemented to prevent oxidation of Sn^{2+} and to fill vacancies in tin, for example, to suppress charge recombination [63]. However, SnF_2 concentration is difficult to monitor, and an excess of SnF_2 will reduce system efficiency. Sn-based low toxic perovskite solar cells continue to lag well behind Pb-based perovskite solar cells in terms of PCEs [58].

2.3 Supercritical Fluids
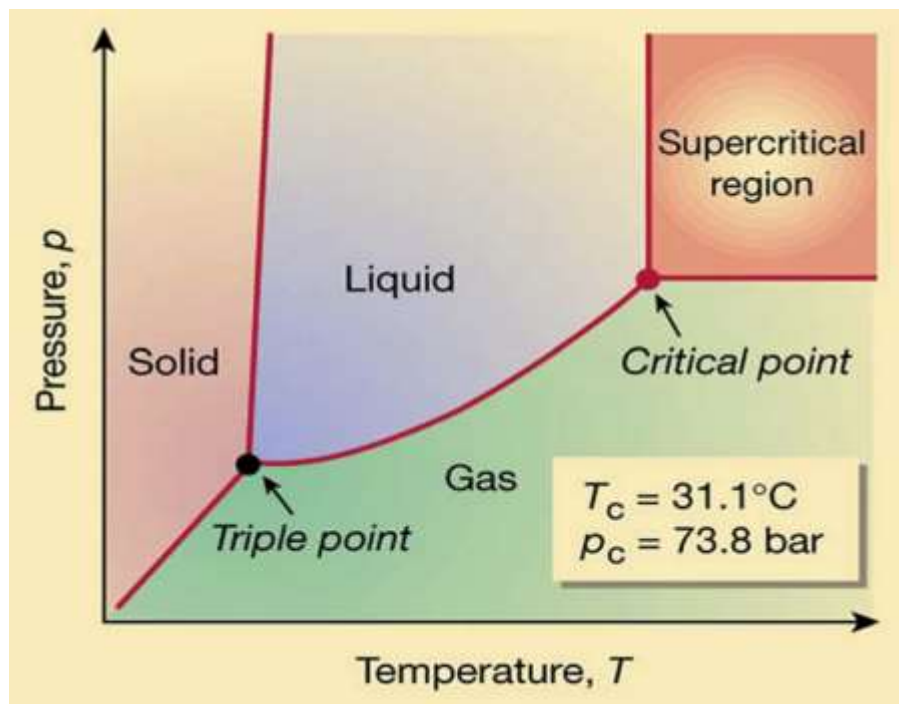
Figure 2.11: Carbon dioxide phase diagram [76].

Fluids above its critical point (T_c,P_c) are in the supercritical region as shown in Figure 2.11 are known as Supercritical Fluids (SCFs). The benefits of SCFs over other fluids or solvents stem largely from their physicochemical properties, which are intermediate between a gas and a liquid and are readily tunable with temperature and pressure changes. As fluids are compressed and heated past the critical point, they turn into a single-phase supercritical fluid with liquid-like solvation strength (liquid density and viscosity) and gas-like diffusion (gas diffusion coefficient) [64]. Table 2.1 compares the thermophysical properties of gas, SCF, and liquid.

Fluid Properties	Gas	SCF	Liquid
Density (gcm^{-3})	$0.6 - 2\times 10^{-3}$	$0.2 – 0.9$	$0.6 – 1.6$
Diffusivity $(m^2 s^{-1})$	$1 - 4\times 10^{-5}$	$2 - 7\times 10^{-8}$	10^{-9}
Viscosity $(Pa.s)$	$1 - 3\times 10^{-5}$	$1 - 9\times 10^{-5}$	10^{-3}

Table 2.1: Comparison of characteristic physical properties of gases, SCFs and liquids [66]

Supercritical carbon dioxide $(scCO_2)$ is carbon dioxide above its critical point (31℃, 1071psi) as shown in Table 2.2 with other common fluids. They are non-toxic, cheap, accessible, non-flammable, and recyclable, and their high permeability allows for higher mass transfer rates by highly permeable nanostructures and thin films [65]. It is the most often used supercritical fluid because of its low critical temperature and pressure, which absorbs less energy. In materials manufacturing, it can function as a solvent, anti-solvent, solute, and reaction medium. It is a non-polar solvent with a large quadrupole moment and a polar C=O bond, which allows certain materials (e.g., carbonyl, hydroxide, or fluoride group) to dissolve [66]. Since 1950, $scCO_2$ has been studied and used in industry for decaffeination of coffee and hop extraction [67], manufacturing of 3D aerogels by extracting organic solvents from wet gels to aerogels [68], exfoliation and intercalation of layered materials [69] [70], coating processing [71] [72], and crystallization of nanostructure materials, thin films, and polymers [73] [74]. Wei et al demonstrated high surface area and electronic properties of dye-sensitized solar cells using supercritical fluid to process the mesoporous crystalline TiO_2 [75].

Fluid	T_c (°C)	P_c (MPa)	Remarks
Carbon dioxide	31.2	7.38	-
Ammonia	132.4	11.29	Toxic
Water	374.1	22.1	High T_c, corrosive
Ethane	32.5	4.91	Flammable
Propane	96.8	4.26	Flammable
Cyclohexane	279.9	4.03	High T_c
Methanol	240.0	7.95	High T_c
Ethanol	243.1	6.39	High T_c
Isopropanol	235.6	5.37	High T_c
Acetone	235	4.76	High T_c
Fluid	T_c (°C)	P_c (MPa)	Remarks
Carbon dioxide	31.2	7.38	-
Ammonia	132.4	11.29	Toxic
Water	374.1	22.1	High T_c, corrosive
Ethane	32.5	4.91	Flammable
Propane	96.8	4.26	Flammable
Cyclohexane	279.9	4.03	High T_c
Methanol	240.0	7.95	High T_c
Ethanol	243.1	6.39	High T_c
Isopropanol	235.6	5.37	High T_c
Acetone	235	4.76	High T_c

Table 2.2: Some SCFs critical properties [66]

2.4 Fundamentals of Crystallization

Understanding nucleation and crystal formation of perovskites is important to achieve a high quality homogenous perovskite film. Supersaturation of the perovskite precursor causes nucleation. A nucleus is modeled as a sphere with a condensed form, with its free energy described by thermodynamic terminology ruled by the classical theory of nucleation [77] [78] [79] [80]. Considering a nucleus with a radius r, the free energy $\Delta G(r)$ is defined as

$$\Delta G(r) = 4\pi r^2 \gamma + \frac{4}{3}\pi r^3 \Delta G_v \qquad (2.7)$$

where γ is the surface free energy per unit area. ΔG_v is the free energy per unit volume of a crystal and is expressed as

$$\Delta G_v = -\frac{RT \ln S}{V_m} \qquad (2.8)$$

where V_m is the molar volume of the monomer crystal. The monomer term refers to the smallest building unit of a crystal. Monomers may either crystallize or dissolve back into solution. Supersaturation levels (S) are classified as [M]/[M]$_o$, where [M]$_o$ is the bulk solid's equilibrium monomer concentration. ΔG_v is defined as the difference between the free energy of the monomer in the crystal and the free energy of the monomer in solution.

In Figure 2.12 - A, the surface and volume terms ($4\pi r^2 \gamma$ and $\frac{4}{3}\pi r^3 \Delta G_v$ respectively) determine the plot of the free energy of the nucleus. When S>1, the volume term helps in the forming of crystals by relieving the extra free energy of the monomers in the supersaturated solution. The surface concept, on the other hand, introduces an additional free-energy prerequisite for nuclei formation. Smaller nuclei than the critical radius (r_c) cannot expand more, but will re-dissolve into solution as monomers, lowering the free energy. Therefore, critical radius is the

threshold where the nuclei will not be dissolved but can expand further. The r_c can be calculated

from the relation $\frac{d\Delta G}{dr} = 0$ at $r = r_c$.

$$r_c = \frac{2\gamma V_m}{RT \ln S}.$$

(2.9)
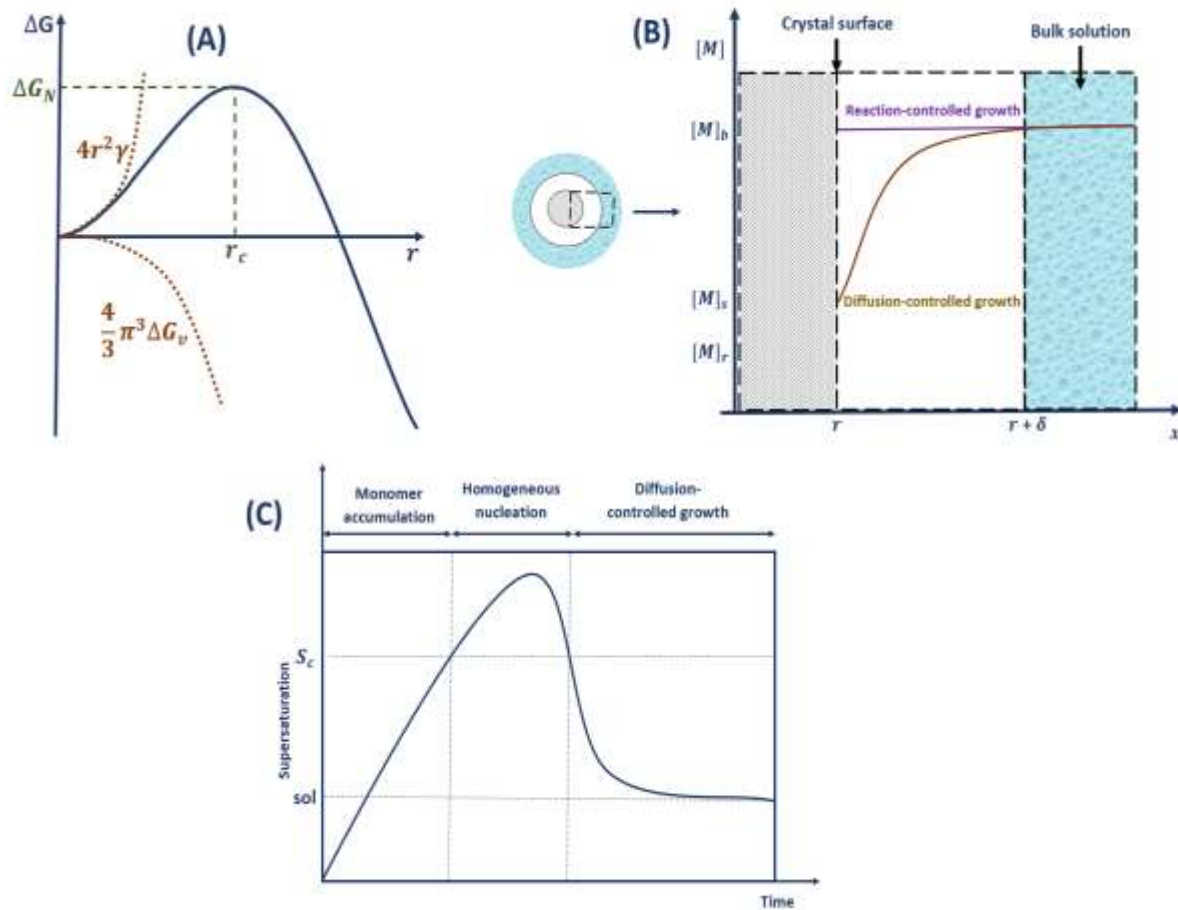
Figure 2.12: (A) Classical nucleation theory diagram - plot of change in free energy (ΔG) vs. particle radius (r) (B) Plot of monomer concentration as a function of distance (x) and schematic illustration of diffusion layer near the surface of a nanocrystal (C) Nucleation and growth dynamics from LaMer diagram. S_c is the critical saturation nucleation [79]

The nucleation rate can be described by the equation

$$\frac{dN}{dt} = A \exp\left[-\frac{\Delta G_N}{k_B T}\right] = A \exp\left[-\frac{16\pi\gamma^3 V_m^2}{3k_B^3 T^3 N_A^2 (\ln S)^2}\right] \qquad (2.10)$$

where N, A, k_B, N_A and T are the number of nuclei, the pre-exponential factor, the Boltzmann constant, Avogadro's number, and temperature respectively. According to Equation 2.10, the existence of an energy barrier (ΔG_N) for homogeneous nucleation is critical for controlling the size distribution in colloidal synthesis of nanocrystals. The rate of nucleation is highly influenced by saturation, temperature, and surface free energy. All of these parameters are important for producing high-quality perovskite films and can be influenced by post-deposition annealing.

After nucleation, crystal growth occurs in two steps, which are the transport of the monomers from the bulk solution onto the crystal surface and the reaction of the monomers on the surface. The first step begins with Fick's law of diffusion

$$j = -D\frac{d[M]}{dx} \qquad (2.11)$$

where j is the flux of the monomers and D is the diffusion coefficient. The concentration gradient along the surface of a spherical particle is depicted in Figure 1B. Let x be the radial distance from the particle's core and $[M]_s$ be the monomer concentration at the crystal's surface (x = r). The concentration exceeds the bulk concentration of the solution $[M]_b$ at a point well away from the particle (x = r + δ). As a result, the overall flux of the monomer onto the particle's surface can be calculated as,

$$J = 4\pi Dr([M]_b - [M]_s). \qquad (2.12)$$

Due to the mass balance, the total flux is equal to the monomer consumption rate by the surface reaction of the particle. In addition, the consumption rate of the monomer by the growth of the particle can be written as,

$$J = 4\pi r^2 k([M]_s - [M]_r)$$ (2.13)

where k is the reaction constant and $[M]_r$ is the solubility of the spherical particle of radius r. The Gibbs-Thomson effect describes how larger particles have lower solubility and expand faster than smaller ones. According to equations 2.12 and 2.13, the average particle growth is determined by either the diffusion mechanism or the surface reaction, as seen in Figure 2.12 - B. Diffusion-controlled growth improves the production of uniform size particles from the steady state of solute diffusion, while the surface reaction is so slow that the concentration of the monomer at the particle surface exceeds a value close to that of the bulk solution.

Figure 2.12 - C depicts the LaMer graph, which defines the change in concentration of the perovskite precursor as a function of time at a constant and isothermal solvent evaporation rate. It consists of three stages being, monomer accumulation in the solution until it reaches a critical value, then homogeneous nucleation creating a supersaturation environment, and finally diffusion-controlled crystal growth. Nucleation stops when the monomer concentration falls below the critical supersaturation value. As the monomer concentration falls below the solubility point, crystal growth ceases (sol).

Ostwald ripening, which depicts the fragmentation of small molecules and their re-deposition onto larger surface surfaces, is another process that can be used to illustrate the growth process of nanoparticles [80]. When particles of different sizes are distributed in a matrix in this model, precipitates compete for growth. Smaller particles dissolve readily due to their high

chemical potential, according to the Gibbs-Thompson principle. As a result, a concentration gradient can form among different-sized particles, allowing solute atoms to travel around in the matrix. At this point, the average radius of the particles increases.

The standard lab-scale spin coating process produces a small degree of supersaturation due to gradual evaporation of the perovskite precursor solvents, resulting in a low density of heterogeneous nuclei. However, as a function of solution supersaturation, the rate of crystal growth is relatively fast, resulting in rapid solute precipitation at regions with high surface energy. Because of the imbalance between nucleation and growth rate, huge dendritic perovskite structures form, resulting in low film quality and therefore poor PCE. As a result, achieving a high nucleation rate prior to crystal growth is important.

In summary, to crystallize perovskite thin films, crystallization regulation is key to obtaining a uniform, homogeneous, and quality film. At least one of these nucleation-growth processes including, solution chemistry engineering [81] [82] [83], interfacial engineering [84] [85] [86] [87], fast nucleation (e.g. antisolvent) [88] [89] [90] [91] [92] [93], slow crystallization (eg. Lewis acid-base adduct) [68] [69] [70] [71] [72] and post-deposition annealing (discussed in coming chapters) are used to simultaneously suppress crystal growth and facilitate nucleation. However, post-deposition annealing is paramount for not only complete crystallization but also helps to achieve grain morphology control, residue solvent removal, higher carrier mobility, and lower density of trap states.

References

1. J. Nelson, The Physics of Solar Cells, Imperial College Press, (2003). https://doi.org/10.1142/9781848161269_0001

2. M. Fox, Optical Properties of Solids, 2nd Edition, Oxford University Press, 2010.

3. M. Dressel and G. Grüner, Electrodynamics of Solids, Optical Properties of Electrons in Matter, Cambridge University Press, Cambridge (2002).

4. Y. Toyozawa, Optical Processes in Solids, Cambridge University Press, Cambridge (2003).

5. C. Kittel, Introduction to Solid State Physics, 8th Edition, Wiley, 2004.

6. A. Kitai, Principles of Solar Cells, LEDs and Related Devices: The Role of the PN Junction, Wiley & Sons Ltd, 2019

7. S. M. I. Hossain, Performance and stability of perovskite solar cells, Graduate Thesis and Dissertations (2018) 16379

8. J. E. Bishop, Development and Optimization of Efficient Spray – Coated Perovskite Solar Cells, 2019

9. A. Kojima, K. Teshima, Y. Shirai, T. Miyasaka, Organometal Halide Perovskites as Visible-Light Sensitizers for Photovoltaic Cells, J. Am. Chem. Soc. 131 (2009) 6050–6051. doi:10.1021/Ja809598r.

10. NREL, Best Research-Cell Efficiency Chart, (2019). https://www.nrel.gov/pv/cell-efficiency.html.

11. T. Duong, Y.L. Wu, H. Shen, J. Peng, X. Fu, D. Jacobs, E.C. Wang, T.C. Kho, K.C. Fong, M. Stocks, E. Franklin, A. Blakers, N. Zin, K. McIntosh, W. Li, Y.B. Cheng, T.P. White, K. Weber, K. Catchpole, Rubidium Multication Perovskite with Optimized Bandgap for

Perovskite-Silicon Tandem with over 26% Efficiency, Adv. Energy Mater. 7 (2017) 1–11. doi:10.1002/aenm.201700228.

12. O. PV, The perovskite-silicon tandem, (n.d.). https://www.oxfordpv.com/perovskite-silicon-tandem

13. H.J.S. M.M Lee, J Teuscher, T Miyasaka, T. N Murakami, Efficient Hybrid Solar Cells Based on Meso-Superstructured Organometal Halide Perovskites, Science (80-.). 338 (2012) 643–647. doi:10.1126/science.1228604.

14. A. Miyata, A. Mitioglu, P. Plochocka, O. Portugall, J.T.W. Wang, S.D. Stranks, H.J. Snaith, R.J. Nicholas, Direct measurement of the exciton binding energy and effective masses for charge carriers in organic-inorganic tri-halide perovskites, Nat. Phys. 11 (2015) 582–587. doi:10.1038/nphys3357.

15. G.E. Eperon, S.D. Stranks, C. Menelaou, M.B. Johnston, L.M. Herz, H.J. Snaith, Formamidinium lead trihalide: A broadly tunable perovskite for efficient planar heterojunction solar cells, Energy Environ. Sci. 7 (2014) 982–988. doi:10.1039/c3ee43822h.

16. C. Kim, S. Ryu, J. Seo, S.I. Il Seok, W.S. Yang, J.H. Noh, N.J. Jeon, Y.C. Kim, S. Ryu, J. Seo, S.I. Il Seok, High-performance photovoltaic perovskite layers fabricated through intramolecular exchange, Science (80-.). 348 (2015) 1–12. doi:10.1126/science.aaa9272.

17. S.D. Stranks, G.E. Eperon, G. Grancini, C. Menelaou, M.J.P. Alcocer, T. Leijtens, L.M. Herz, A. Petrozza, H.J. Snaith, Electron-Hole Diffusion Lengths Exceeding Trihalide Perovskite Absorber, Science (80-.). 342 (2013) 341–344. doi:10.1126/science.1243982.

18. K.X. Steirer, P. Schulz, G. Teeter, V. Stevanovic, M. Yang, K. Zhu, J.J. Berry, Defect Tolerance in Methylammonium Lead Triiodide Perovskite, ACS Energy Lett. 1 (2016) 360–366. doi:10.1021/acsenergylett.6b00196.

19. H-S. Kim, C-R. Lee, J-H. Im, K-B. Lee, T. Moehl, A. Marchioro, S-J. Moon, R. Humphry-Baker, J-H. Yum, J. E. Moser, M. Gratzel, N-G. Park, Lead iodide perovskite sensitized all-solid-state submicron thin film mesoscopic solar cell with efficiency exceeding 9%, Sci Rep 591 (2012) 1 - 7. DOI: 10.1038/srep00591

20. A. Toshniwal, V. Kheraj, Development of organic-inorganic tin halide perovskites: A review, Sol Energy 149 (2017) 54 - 59. DOI: 10.1016/j.solener.2017.03.077

21. T. A Berhe, W-N. Su, C-H. Chen, C-J. Pan, J-H. Cheng, j-M, Chen, M-C. Tsai, L-Y. Chen, A. A. Dubale, B-J. Hwang, Organometal halide perovskite solar cells: degradation and stability. Energy Environ Sci, 9 (2016) 323 - 356. doi.org/10.1039/C5EE02733K

22. C. Motta, F. El-Mellouhi, S. Kais, N. Tabet, F. Alharbi, S. Sanvito, Revealing the role of organic cations in hybrid halide perovskite $CH_3NH_3PbI_3$, Nat. Commun. 2015, 6, 7026. DOI: 10.1038/ncomms8026

23. T. Etienne, E. Mosconi, F. De Angelis, Dynamical Origin of the Rashba Effect in Organohalide Lead Perovskites: A Key to Suppressed Carrier Recombination in Perovskite Solar Cells?, J. Phys. Chem. Lett. 2016, 7, 1638.

24. N. K. Noel, B. Wenger, S. N. Habisreutinger, J. B. Patel, T. Crothers, Z. Wang, R. J. Nicholas, M. B. Johnston, L. M. Herz, H. J. Snaith, Highly Crystalline Methylammonium Lead Tribromide Perovskite Films for Efficient Photovoltaic Devices, ACS Energy Lett. 2018, 3, 1233.

25. T. J. Savenije, C. S. Ponseca, L. Kunneman, M. Abdellah, K. Zheng, Y. Tian, Q. Zhu, S. E. Canton, I. G. Scheblykin, T. Pullerits, A. Yartsev, V. Sundström, Thermally Activated Exciton Dissociation and Recombination Control the Carrier Dynamics in Organometal Halide Perovskite, J. Phys. Chem. Lett. 2014, 5, 2189.

26. Q. Dong, Y. Fang, Y. Shao, P. Mulligan, J. Qiu, L. Cao, Solar cells. Electron-hole diffusion lengths > 175 μm in solution-grown $CH_3NH_3PbI_3$ single crystals, J. Huang, Science. 2015, 347, 967.

27. J. M. Ball, A. Petrozza, Defects in perovskite-halides and their effects in solar cells, Nat. Energy 2016, 1, 16149.

28. K. X. Steirer, P. Schulz, G. Teeter, V. Stevanovic, M. Yang, K. Zhu, J. J. Berry, Defect Tolerance in Methylammonium Lead Triiodide Perovskite, ACS Energy Lett. 2016, 1, 360.

29. M. Saliba, T. Matsui, J.-Y. Seo, K. Domanski, J.-P. Correa-Baena, N. Mohammad K., S. M. Zakeeruddin, W. Tress, A. Abate, A. Hagfeldt, M. Gratzel, Cesium-containing triple cation perovskite solar cells: improved stability, reproducibility and high efficiency, Energy Environ. Sci. 2016, 9, 1989.

30. W. S. Yang, B.-W. Park, E. H. Jung, N. J. Jeon, Y. C. Kim, D. U. Lee, S. S. Shin, J. Seo, E. K. Kim, J. H. Noh, S. Il Seok, Iodide management in formamidinium-lead-halide-based perovskite layers for efficient solar cells, Science. 2017, 356, 1376. \doi: 10.1126/science.aan2301.

31. G.A Al-Dainy, S.E. Bourdo, V. Saini, B.C. Berry, A.S. Biris, Hybrid Perovskite Photovoltaic Devices: Properties, Architecture and Fabrication Methods. Energy Technology, 2017, 5, 373–401. doi.org/10.1002/ente.201600486

32. Z. Wei, H. Chen, K. Yan, S. Yang, Inkjet printing and instant chemical transformation of a CH3NH3PbI3/nanocarbon electrode and interface for planar perovskite solar cells. Angew Chem Int Ed, 2014, 53, 13239–13243. DOI: 10.1002/anie.201408638

33. F. Fabregat-Santiago, J. Bisquert, G.Garcia-Belmonte, G. Boschloo, A. Hagfeldt, Influence of electrolyte in transport and recombination in dye-sensitized solar cells studied by impedance spectroscopy. Sol Energy Mater Sol Cells, 2005, 87, 117– 131. DOI: 10.1016/j.solmat.2004.07.017

34. N.J. Jeon, J.H. Noh, Y.C. Kim, W.S. Yang, S.C. Ryu, S.I. Seok, Solvent engineering for high-performance inorganic-organic hybrid perovskite solar cells, Nat. Mater., 13 (2014), pp. 897-903.

35. N.J. Jeon, J.H. Noh, W.S. Yang, Y.C. Kim, S. Ryu, J. Seo, S.I. Seok, Compositional engineering of perovskite materials for high-performance solar cells, Nature, 517 (2015), p. 476480.

36. W.S. Yang, J.H. Noh, N.J. Jeon, Y.C. Kim, S.C. Ryu, J.W. Seo, S.I. Seok, High-performance photovoltaic perovskite layers fabricated through intramolecular exchange, Science, 348 (2015), pp. 1234-1237.

37. J. Burschka, N. Pellet, S.-J. Moon, R. Humphry-Baker, P. Gao, M.K. Nazeeruddin, M. Grätzel, Sequential deposition as a route to high-performance perovskite-sensitized solar cells, Nature, 499 (2013), pp. 316-319

38. B.-E. Cohen, S. Gamliel, L. Etgara, Parameters influencing the deposition of methylammonium lead halide iodide in hole conductor free perovskite-based solar cells, Apl. Mater., 2 (2014), p. 081502

39. C. Bi, Q. Wang, Y.C. Shao, Y.B. Yuan, Z.G. Xiao, J.S. Huang, Non-wetting surface-driven high-aspect-ratio crystalline grain growth for efficient hybrid perovskite solar cells, Nat. Commun., 6 (2015), p. 7747

40. G. Li, T.Y. Zhang, Y.X. Zhao, Hydrochloric acid accelerated formation of planar $CHCH_3NH_3PbI_3$ perovskite with high humidity tolerance, J. Mater. Chem. A, 3 (2015), pp. 19674-19678

41. Q.Q. Lin, A. Armin, R.C.R. Nagiri, P.L. Burn, P. Meredith, Electro-optics of perovskite solar cells, Nat. Photonics, 9 (2014), pp. 106-112

42. M.Z. Liu, M.B. Johnston, H.J. Snaith, Efficient planar heterojunction perovskite solar cells by vapour deposition, Nature, 501 (2013), pp. 395-398

43. A. Ng, Z.W. Ren, Q. Shen, S.H. Cheung, H.C. Gokkaya, G.X. Bai, J.C. Wang, L.J. Yang, S.K. So, A.B. Djurišić, W.W.-F. Leung, J.H. Hao, W.K. Chan, C. Surya, Efficiency enhancement by defect engineering in perovskite photovoltaic cells prepared using evaporated PbI_2/CH_3NH_3 I multilayers, J. Mater. Chem. A, 3 (2015), pp. 9223-9231

44. C.-W. Chen, H.-W. Kang, S.-Y. Hsiao, P.-F. Yang, K.-M. Chiang, H.-W. Lin, Efficient and uniform planar-type perovskite solar cells by simple sequential vacuum deposition, Adv. Mater., 26 (2014), pp. 6647-6652

45. J. Yin, H. Qu, J. Cao, H.L. Tai, J. Li, N.F. Zheng, Vapor-assisted crystallization control toward high performance perovskite photovoltaics with over 18% efficiency in the ambient atmosphere, J. Mater. Chem. A, 4 (2016), pp. 13203-13210.

46. Q. Chen, H.P. Zhou, T.B. Song, S. Luo, Z. Hong, H.S. Duan, L. Dou, Y.S. Liu, Y. Yang, Controllable self-induced passivation of hybrid lead iodide perovskites toward high performance solar cells, Nano Lett., 14 (2014), pp. 4158-4163

47. Q. Chen, H.P. Zhou, Z.R. Hong, S. Luo, H.S. Duan, H.H. Wang, Y.S. Liu, G. Li, Y. Yang, Planar heterojunction perovskite solar cells via vapor-assisted solution process, J. Am. Chem. Soc., 136 (2014), pp. 622-625

48. C. Ying, C.W. Shi, N. Wu, J.C. Zhang, M. Wang, A two-layer structured PbI_2 thin film for efficient planar perovskite solar cells, Nanoscale, 7 (2015), pp. 12092-12095.

49. A. Djurisic, F. Liu, H. Tam et al., "Perovskite solar cells - An ´ overview of critical issues," Progress in Quantum Electronics, vol. 53, pp. 1–37, 2017

50. R. G. Larson and T. J. Rehg, S. F. Kitsler and P. M. Schweizer, Liquid Film Coating., Chapman & Hall, 1st edn, 1997, ch. 14, pp. 709-734.

51. M. Pichumani, P. Bagheri, K.M. Poduska, W. Gonzalez-Vinas, A. Yethiraj, Dynamic, crystallization and structures in colloid spin coating, Soft Matter (9), 3220-3229 (2013); doi: 10.1039/C3SM27455A.

52. X. Peng , J. Yuan , S. Shen , M. Gao , A. S. Chesman , H. Yin , J. Cheng , Q. Zhang and D. Angmo , Perovskite and Organic Solar Cells Fabricated by Inkjet Printing: Progress and Prospects, Adv. Funct. Mater., 2017, **27** , 1703704. doi.org/10.1002/adfm.201703704

53. F. Di Giacomo , S. Shanmugam , H. Fledderus , B. J. Bruijnaers , W. J. H. Verhees , M. S. Dorenkamper , S. C. Veenstra , W. Qiu , R. Gehlhaar , T. Merckx , T. Aernouts , R. Andriessen and Y. Galagan , Up-scalable sheet-to-sheet production of high efficiency perovskite module and solar cells on 6-in. substrate using slot die coating, *Sol. Energy Mater. Sol. Cells*, 2018, **181** , 53 —59

54. J. Li , R. Munir , Y. Fan , T. Niu , Y. Liu , Y. Zhong , Z. Yang , Y. Tian , B. Liu and J. Sun, Phase Transition Control for High-Performance Blade-Coated Perovskite Solar Cells, *Joule*, 2018**,** 2 , 1313 —1330,

55. Y. S. Jung , K. Hwang , Y. J. Heo , J. E. Kim , D. Vak and D. Y. Kim, Progress in Scalable Coating and Roll-to-Roll Compatible Printing Processes of Perovskite Solar Cells toward Realization of Commercialization, Adv. Opt. Mater., 2018, **6** , 1701182

56. J.-W. Lee , S.-I. Na and S.-S. Kim, Efficient spin-coating-free planar heterojunction perovskite solar cells fabricated with successive brush-painting, *J. Power Sources*, 2017, 339 , 33 —40

57. Y. Jiang, C. Wu, L. Li, K. Wang, Z. Tao, F. Gao, W. Cheng, J. Cheng, X.Y. Zhao, S. Priya, W. Deng, All electrospray printed perovskite solar cells, Nano Energy. 53 (2018) 440–448. doi:10.1016/j.nanoen.2018.08.062.

58. F. Huang, M. Li, P. Siffalovic, G. Cao and J. Tian, From scalable solution fabrication of perovskite films towards commercialization of solar cells, Energy Environ. Sci., 2019, 12, 518

59. M.M. Byranvand, T. Kim, S. Song, G. Kang, S.U. Ryu, T. Park, p-Type CuI Islands on TiO2 Electron Transport Layer for a Highly Efficient Planar-Perovskite Solar Cell with Negligible Hysteresis, Adv. Energy Mater., 8 (2017), p. 1702235

60. Z. Wang, Z. Shi, T. Li, Y. Chen, W. Huang, Stability of Perovskite Solar Cells: A Prospective on the Substitution of the A Cation and X Anion, Angew. Chemie - Int. Ed., 56 (2017), pp. 1190-1212

61. F. Hao , C. C. Stoumpos , D. H. Cao , R. P. H. Chang and M. G. Kanatzidis, Lead-free solid state organic-inorganic halide perovskite solar cells, Nat. Photonics, 2014, **8** , 489 -494

62. H. Hu , B. Dong and W. Zhang , Low-toxic metal halide perovskites: opportunities and future challenges, J. Mater. Chem. A, 2017, 5 , 11436 —11449

63. S. J. Lee , S. S. Shin , Y. C. Kim , D. Kim , T. K. Ahn , J. H. Noh , J. Seo and S. I. Seok, Fabrication of Efficient Formamidinium Tin Iodide Perovskite Solar Cells through SnF_2–Pyrazine Complex, *J. Am. Chem. Soc.*, 2016, **138** , 3974 —3977

64. A. Kaleva, S. Heinonen, J.-P. Nikkanen, E. Levänen, Synthesis and crystallization of titanium dioxide in supercritical carbon dioxide (scCO2), IOP Conf. Ser. Mater. Sci. Eng. 175 (2017). doi:doi:10.1088/1757-899X/175/1/012034.

65. D. Sanli, S.E. Bozbag, C. Erkey, Synthesis of nanostructured materials using supercritical CO 2: Part I. Physical transformations, J. Mater. Sci. 47 (2012) 2995–3025. doi:10.1007/s10853-011-6054-y.

66. X. Zhang, S. Heinonen, E. Levänen, Applications of supercritical carbon dioxide in materials processing and synthesis, RSC Adv. 4 (2014) 61137–61152. doi:10.1039/c4ra10662h.

67. I. De Marco, S. Riemma, R. Iannone, Supercritical carbon dioxide decaffeination process: A Life Cycle Assessment study, Chem. Eng. Trans. 57 (2017) 1699–1704. doi:10.3303/CET1757284.

68. T.Y. Wei, C.H. Chen, H.C. Chien, S.Y. Lu, C.C. Hu, A cost-effective supercapacitor material of ultrahigh specific capacitances: spinel nickel cobaltite aerogels from an epoxide-driven sol-gel process, Adv. Mater. 22 (2010) 347–351. doi:10.1002/adma.200902175.

69. N.W. Pu, C.A. Wang, Y. Sung, Y.M. Liu, M. Der Ger, Production of few-layer graphene by supercritical CO2 exfoliation of graphite, Mater. Lett. 63 (2009) 1987–1989. doi:10.1016/j.matlet.2009.06.031.

70. Y. Wang, C. Zhou, W. Wang, Y. Zhao, Preparation of two dimensional atomic crystals BN, WS2, and MoS2 by supercritical CO2 assisted with ultrasound, Ind. Eng. Chem. Res. 52 (2013) 4379–4382. doi:10.1021/ie303633c.

71. J.M. Blackburn, D.P. Long, A. Cabañas, J.J. Watkins, Deposition of conformal copper and nickel films from supercritical carbon dioxide, Science (80-.). 294 (2001) 141–145. doi:10.1126/science.1064148.

72. A. Cabañas, D.P. Long, J.J. Watkins, Deposition of gold films and nanostructures from supercritical carbon dioxide, Chem. Mater. 16 (2004) 2028–2033. doi:10.1021/cm034739u.

73. M. Sajfrtová, M. Cerhová, V. Jandová, V. Dřínek, S. Daniš, L. Matějová, The effect of type and concentration of modifier in supercritical carbon dioxide on crystallization of nanocrystalline titania thin films, J. Supercrit. Fluids. 133 (2018) 211–217. doi:10.1016/j.supflu.2017.10.012.

74. H.E. Naguib, C.B. Park, S.W. Song, Effect of supercritical gas on crystallization of linear and branched polypropylene resins with foaming additives, Ind. Eng. Chem. Res. 44 (2005) 6685–6691. doi:10.1021/ie0489608.

75. M. Wei, K. Wang, M. Yanagida, H. Sugihara, M.A. Morris, J.D. Holmes, H. Zhou, Supercritical fluid processing of mesoporous crystalline TiO_2 thin films for highly efficient dye-sensitized solar cells, J. Mater. Chem. 17 (2007) 3888–3893. doi:10.1039/b706569h.

76. W. Leitner, Green chemistry: designed to dissolve, Nature, 2000, 405, 129–130, copyright (2000).

77. J.W. Mullin, Crystallization, Fourth Edition, Butterworth Heinemann, 2001

78. R. Strey, P.E. Wagner, Y. Viisanen, The Problem of Measuring Homogeneous Nucleation Rates and the Molecular Contents of Nuclei: Progress in the Form of Nucleation Pulse Measurements, J. Phys. Chem, 1994, 98, 7748 – 7758

79. S.G. Kwon, T. Hyeon, Formation Mechanisms of Uniform Nanocrystals via Hot-Injection and Heat-Up Methods, small, 2011, 7, 2685 – 2702

80. C. Liu, Y-B. Cheng, Z. Ge, Understanding of perovskite crystal growth and film formation in scalable deposition processes, Chem. Soc. Rev., 2020, 49, 1653 – 1687

81. P-W. Liang, C-Y. Liao, C-C. Chueh, F. Zuo, S.T. Williams, X-K. Xin, J. Lin, A. K-Y. Jen, Additive Enhanced Crystallization of Solution-Processed Perovskite for Highly Efficient Planar-Heterojunction Solar Cells, Adv. Mater. 2014, 26, 3748 – 3754

82. D.P. Mcmeekin, Z. Wang, W. Rehman, F. Pulvirenti, J.B. Patel, N.K. Noel, M.B. Johnston, S.R. Marder, L.M. Herz, H.J. Snaith, Crystallization Kinetics and Morphology Control of Formamidinium – Cesium Mixed-Cation Lead Mixed-Halide Perovskite via Tunability of the Colloidal Precursor Solution, Adv. Mater., 2017, 29, 1607039. doi:10.1002/adma.201607039.

83. G.E. Eperon, S.D. Stranks, C. Menelaou, M.B. Johnston, L.M. Herz, H.J. Snaith, Formamidinium lead trihalide: A broadly tunable perovskite for efficient planar heterojunction solar cells, Energy Environ. Sci. 7 (2014) 982–988. doi:10.1039/c3ee43822h.

84. A. Giuri, S. Masi, S. Colella, A. Kovtun, S.D. Elce, E. Treossi, A. Liscio, C.E. Corcione, A. Rizzo, A. Listorti, Cooperative Effect of GO and Glucose on PEDOT : PSS for High V OC and Hysteresis-Free Solution-Processed Perovskite Solar Cells, Adv. Funct. Mater. 2016, 26, 6985 - 6994. doi:10.1002/adfm.201603023.

85. Q. Xue, G. Chen, M. Liu, J. Xiao, Z. Chen, Z. Hu, Improving Film Formation and Photovoltage of Highly Efficient Inverted-Type Perovskite Solar Cells through the Incorporation of New Polymeric Hole Selective Layers, Adv. Energy Mater. 2016, 6, 1502021. doi:10.1002/aenm.201502021.

86. C. Liu, K. Wang, P. Du, T. Meng, X. Yu, S.Z.D. Cheng, X. Gong, High Performance Planar Heterojunction Perovskite Solar Cells with Fullerene Derivatives as the Electron Transport Layer, ACS Appl. Mater. Interfaces 2015, 7, 1153 - 1159. doi:10.1021/am506869k.

87. C. Bi, Q. Wang, Y. Shao, Y. Yuan, Z. Xiao, J. Huang, Non-wetting surface-driven high-aspect-ratio crystalline grain growth for efficient hybrid perovskite solar cells, Nat. Commun. (2015) 1–7. doi:10.1038/ncomms8747.

88. Y. Wang, J. Wu, P. Zhang, D. Liu, T. Zhang, L. Ji, X. Gu, Z. David, S. Li, Nano Energy Stitching triple cation perovskite by a mixed anti-solvent process for high performance perovskite solar cells, Nano Energy, 39 (2017) 616–625. doi:10.1016/j.nanoen.2017.07.046.

89. S. Paek, P. Schouwink, E.N. Athanasopoulou, K.T. Cho, G. Grancini, Y. Lee, Y. Zhang, F. Stellacci, M.K. Nazeeruddin, P. Gao, From Nano- to Micrometer Scale : The Role of Antisolvent Treatment on High Performance Perovskite Solar Cells, Chem. Mater. 2017, 2017, 29, 3490 - 3498. doi:10.1021/acs.chemmater.6b05353.

90. Y. Yu, S. Yang, L. Lei, Q. Cao, J. Shao, S. Zhang, Y. Liu, Ultrasmooth Perovskite Film via Mixed Anti-Solvent Strategy with Improved Efficiency, ACS Appl. Mater. Interfaces 2017, 9, 3667 - 3676. doi:10.1021/acsami.6b14270.

91. T. Bu, L. Wu, X. Liu, X. Yang, P. Zhou, X. Yu, T. Qin, Synergic Interface Optimization with Green Solvent Engineering in Mixed Perovskite Solar Cells, Adv. Energy Mater. 2017, 7, 1700578. doi:10.1002/aenm.201700576.

92. M. Xiao, F. Huang, W. Huang, Y. Dkhissi, Y. Zhu, J. Etheridge, A. Gray-weale, U. Bach, Y. Cheng, L. Spiccia, A Fast Deposition-Crystallization Procedure for Highly Efficient Lead Iodide Perovskite Thin-Film Solar Cells, Angew. Chem. Int. Ed. 2014, 53, 9898 - 9903. doi:10.1002/anie.201405334.

93. D. Gedamu, I.M. Asuo, D. Benetti, M. Basti, I. Ka, S.G. Cloutier, F. Rosei, R. Nechache, Solvent-Antisolvent Ambient Processed Large Grain Size Perovskite Thin Films for High-Performance Solar Cells, Sci. Rep. (2018) 1–11. doi:10.1038/s41598-018-31184-0.

94. J. Lee, S. Bae, Y. Hsieh, N. De, M. Wang, J. Lee, S. Bae, Y. Hsieh, N. De Marco, M. Wang, A Bifunctional Lewis Base Additive for Microscopic Homogeneity in Perovskite Solar Cells A Bifunctional Lewis Base Additive for Microscopic Homogeneity in Perovskite Solar Cells, Chem 3, 290 -302. doi:10.1016/j.chempr.2017.05.020.

95. J. Lee, H. Kim, N. Park, Lewis Acid − Base Adduct Approach for High Efficiency Perovskite Solar Cells, Acc. Chem. Res. 2016, 49, 311-319. doi:10.1021/acs.accounts.5b00440.

96. Y. Lin, L. Shen, J. Dai, Y. Deng, Y. Wu, Y. Bai, X. Zheng, π -Conjugated Lewis Base : Efficient Trap-Passivation and Charge-Extraction for Hybrid Perovskite Solar Cells, Adv. Mater. 2017, 29, 1604545. doi:10.1002/adma.201604545.

97. N. Ahn, D.Y. Son, I.H. Jang, S.M. Kang, M. Choi, N.G. Park, Highly Reproducible Perovskite Solar Cells with Average Efficiency of 18.3% and Best Efficiency of 19.7%

Fabricated via Lewis Base Adduct of Lead(II) Iodide, J. Am. Chem. Soc. 137 (2015) 8696–8699. doi:10.1021/jacs.5b04930.

CHAPTER 3

EFFECT OF SUPERCRITICAL CARBON DIOXIDE ON $CH_3NH_3PbI_3$ FILMS

3.1 Introduction

After depositing perovskite thin films from the precursor solution, thermal annealing through conduction (hotplate) [1] or convection (oven) [2] are typically used to induce solid-state crystallization resulting in high quality films with large grain sizes, fewer defects, and superior photovoltaic performance. Nonetheless, annealing at high temperatures usually above 100℃ have been reported to decompose the crystals thus reducing performance [3]. Due to this, other post-annealing methods have been explored such as solvent annealing [4] [5], microwave annealing [6], ultrasonic vibration annealing [7] [8], and hot-pressing annealing [9]. However, these approaches result in poor film quality, longer crystallization times and are sophisticated, thus not suitable for scalability. Complete crystallization and uniform perovskite film with no pinholes is needed to ensure excellent performance. In this chapter, we demonstrate complete crystallization, large grain size, and uniform perovskite thin films with $scCO_2$ annealing [10].

This chapter shows the effect of some key parameters of $scCO_2$ on the crystallinity and average grain size of $CH_3NH_3PbI_3$ thin films. The $scCO_2$ fluid behaves as an anti-solvent for perovskite thin films. The word anti-solvent is usually used in solution crystallization to denote a second solvent, which when added to the first solvent decreases the solubility of the solute. Here, we are using the more fundamental definition to define a solvent in which the product is insoluble. The perovskite thin film did not dissolve in the $scCO_2$ anti-solvent but enhanced solid-state reaction kinetics for complete crystallization.

3.2 Experimental Method

3.2.1 Material and precursor preparation

The perovskite precursor solution was synthesized by mixing a 1:1:1 molar ratio of 2.385g of methylammonium iodide (CH_3NH_3I) (98%, Sigma Aldrich), 6.915g of lead (II) iodide (PbI_2) (99.9985%, Alfa Aesar) and 1.063 mL of dimethyl sulfoxide (DMSO) (≥99.9%, anhydrous, sigma Aldrich) in 9.484mL of N,N-dimethylformamide (DMF) (≥99.8%, anhydrous, Sigma Aldrich) and 0.3mL of diethyl ether (anhydrous, Acros Organics). The solution was processed in an argon-filled glovebox, stirred at room temperature for 1 hour, and filtered with a 0.2μm syringe filter [11] [10].

3.2.2 $CH_3NH_3PbI_3$ perovskite thin film fabrication
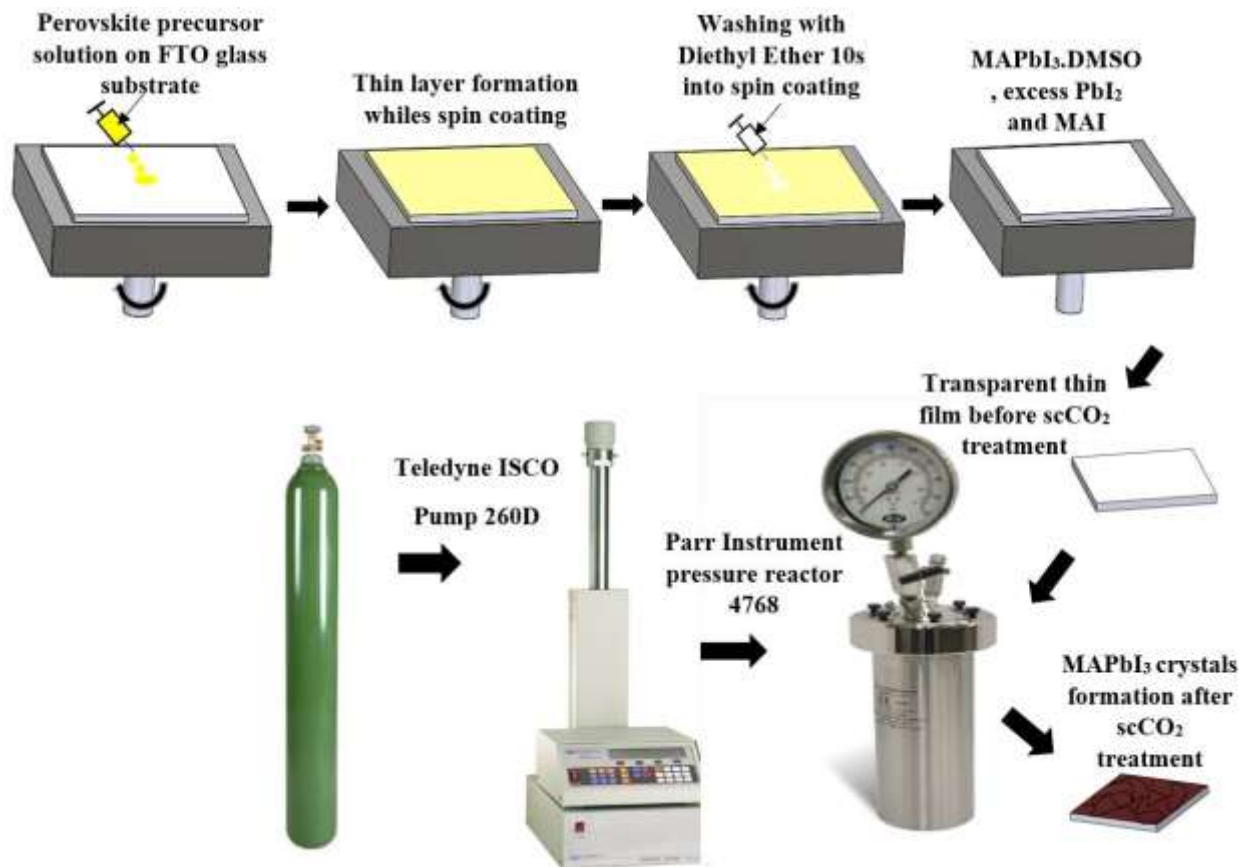
Figure 3.1: Diagram of the process used to prepare the perovskite thin film using scCO$_2$ post-annealing [10]

Fluorine-tin-oxide (FTO) substrate (12-14Ω, 1"×1"×2.2mm, MTI corporation) was cleaned with detergent, deionized water, acetone, and isopropyl alcohol. The precursor solution was spin coated onto the FTO glass slide at 6000rpm for 25sec. During the spin coating procedure, 0.5mL of diethyl ether was dripped onto the rotating surface at the sixth second into the 25 seconds rotation. The thin film was then placed into a pressure vessel (Parr Instrument Pressure Reactor 4768) and a syringe pump (Teledyne ISCO Pump 260D) was used to pressurize the CO_2 for perovskite crystallization. This experiment was carried out at different temperatures (ranging from 35℃ to 100℃) and pressures (8.27MPa (1200psi), 11.03 MPa (1600psi), 13.79MPa (2000psi)). We employed post-deposition annealing by thermal annealing as a control for comparison and baseline [10] [11].

3.2.3 $CH_3NH_3PbI_3$ Film characterization

The crystallographic properties of the perovskite were characterized by X-ray diffraction (XRD) scanning (PANalytical MPD X'pert Pro), using a Cu Kα ($\lambda = 1.5444$ nm) radiation source that operated at 45kV and 40mA. The X-ray diffractograms were obtained at a scan rate of 0.01°/s for 2θ values between 10° and 60°. The surface coverage and grain size were obtained using a scanning electron microscope (SEM) (Hitachi SU-70 FE-SEM) at 20kV and analyzed using the ImageJ software package. Optical spectrometry (transmission, reflection, absorption) of the films was conducted using a spectral response measurement system (PerkinElmer Lambda 35 UV/VIS Spectrometer).

3.3 Effect of different $scCO_2$ annealing pressure on $CH_3NH_3PbI_3$ thin film
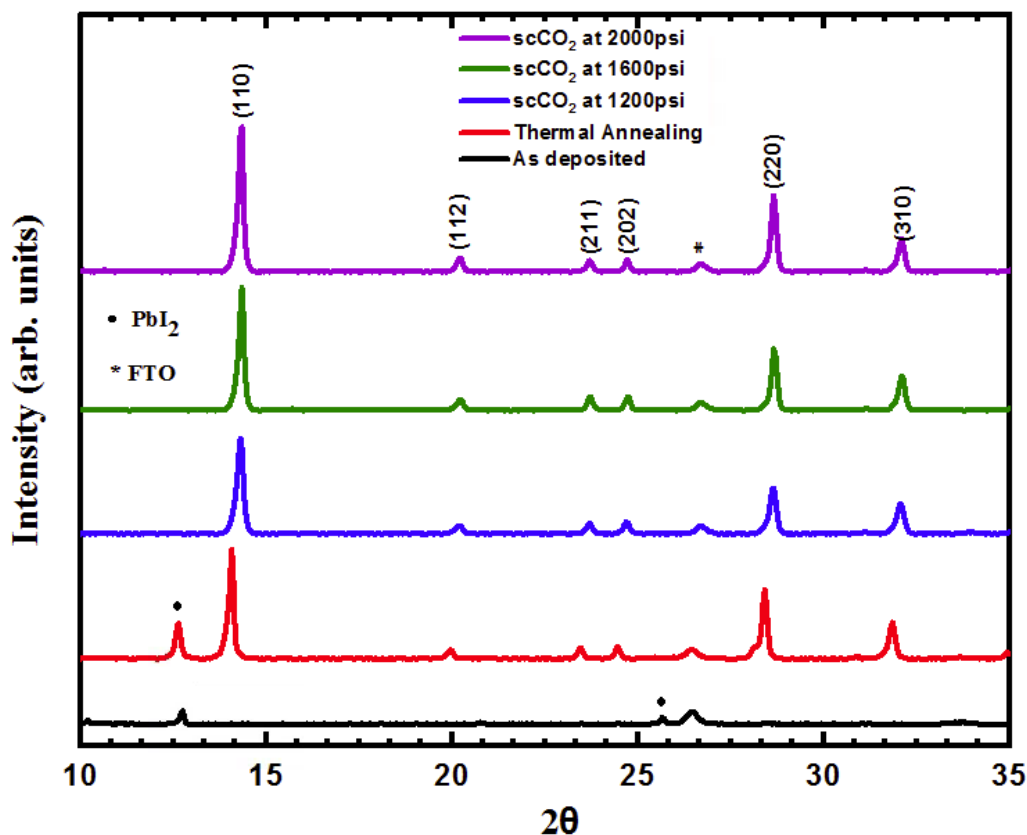
Figure 3.2: XRD patterns of perovskite thin film annealed for 15 minutes: (Black) as-deposited, (Red) thermal annealing at 45°C, (Green) $scCO_2$ annealing at (1200psi, 45°C), (Blue) $scCO_2$ annealing at (1600psi, 45°C) and (Magenta) $scCO_2$ annealing at (2000psi, 45°C)

Figure 3.2 shows XRD patterns at no annealing, thermal annealing at 45°C and $scCO_2$ annealing with different pressures. The pattern for as-deposited films or with no annealing exhibited (100) and (101) peaks, which were consistent with PbI_2 [12] [13], and the perovskite crystals did not form. With thermal annealing alone at 45°C, the typical peaks at 14.1°, 24.8°, 28.7°, and 32.2°, corresponding to the (110), (202), (220), and (310) of the tetragonal phase perovskite

were present. However, the PbI$_2$ peak was still present at (100), indicating incomplete crystallization. With scCO$_2$ annealing, there was complete crystallization of the perovskite film at pressures of 1200psi, 1600psi, and 2000psi with the no PbI$_2$ peaks present, which indicated elimination of impurities. With an increase in scCO$_2$ annealing pressure, the overall XRD pattern was similar, indicating no change in the perovskite phase and no degradation. It is known that the uniform perovskite films with oriented crystalline domains ensure high charge mobility necessary for high-performance solar cells [14].
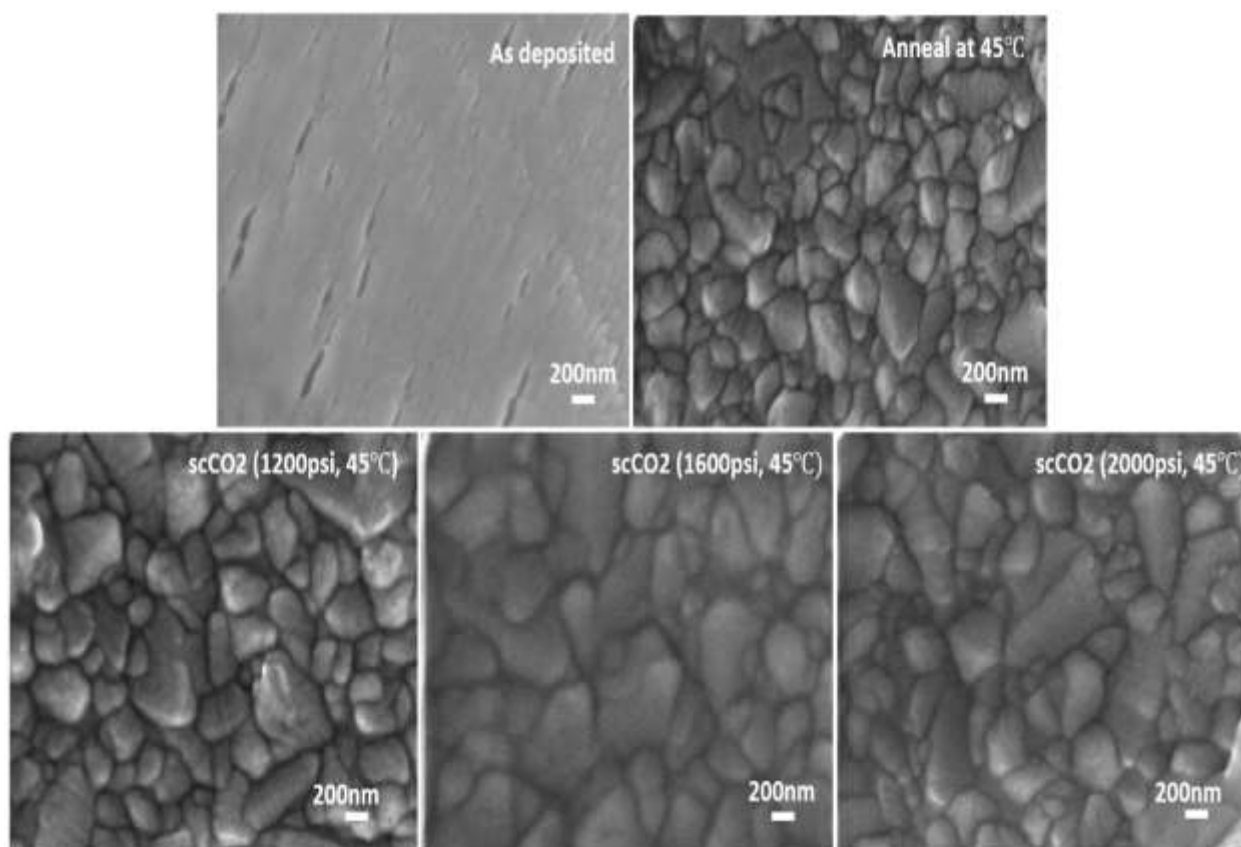
Figure 3.3: SEM images of the top surface of the thin film at different treatment conditions for 15 minutes and increase in pressure in the scCO$_2$ region

Figure 3.3 shows SEM images of the top surfaces of the thin films corresponding to no annealing, thermal annealing at 45°C, and $scCO_2$ annealing with different pressures. At no form of post-deposition annealing, there was no large grain formation and there were many pinholes, indicating a poor film quality. Visually, after deposition, the as-deposited film was transparent which indicated no formation of perovskite (dark brown visually). The morphology after thermal annealing at 100°C and annealing with $scCO_2$ showed grains consistent with perovskite [15] [16].
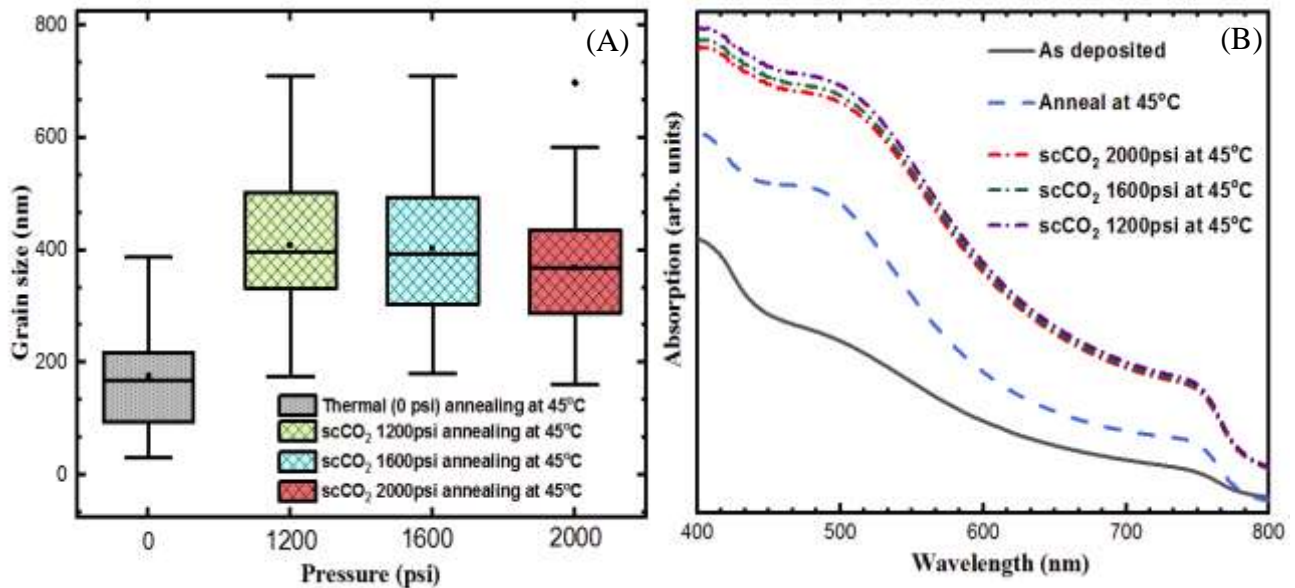
Figure 3.4: (A) Effect of $scCO_2$ annealing pressure on grain size, (B) Optical absorption spectra of the thin film at different $scCO_2$ annealing pressure conditions

The results showed a substantial increase in the average grain size when comparing thermal annealing to $scCO_2$ annealing all at the same temperature. The average grain size about 175nm with thermal annealing at 45 °C compared to about 400nm with $scCO_2$ annealing as shown in Figure 3.4 - A. At lower thermal annealing temperatures without the assistance of $scCO_2$, there was insufficient energy provided to the thin film for complete crystallization and grain growth as

confirmed with the XRD pattern. In terms of grain size and uniformity, increasing pressure during $scCO_2$ annealing did not yield major changes, thus showed no benefit in increasing pressure during annealing. Figure 3.4 - B shows the optical absorption spectra corresponding to no annealing, thermal annealing at 45℃ and $scCO_2$ annealing with different pressures. From the spectra, perovskite films with $scCO_2$ annealing showed better absorption than films treated with thermal annealing alone due to complete crystallization, larger grains, and greater film uniformity [17] [18].

3.4 Effect of different $scCO_2$ annealing time on $CH_3NH_3PbI_3$ thin film
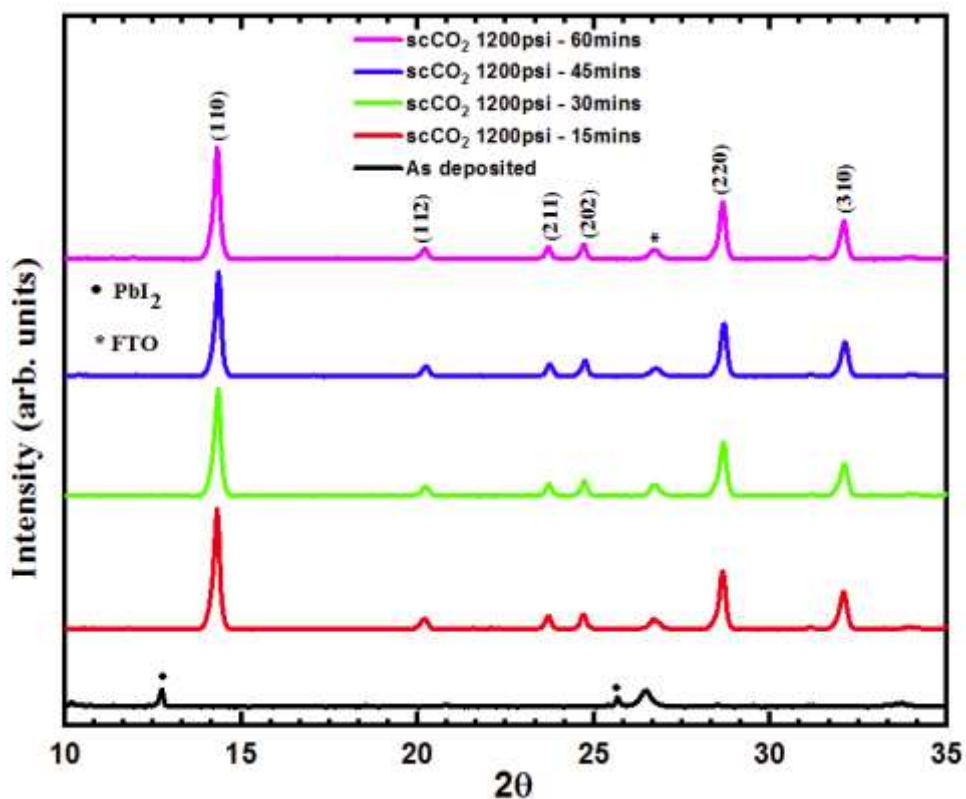
Figure 3.5: XRD patterns of perovskite thin film annealed for 1200 psi: (Black) as-deposited, (Red) $scCO_2$ annealing at (15 minutes, 45 ℃), (Green) $scCO_2$ annealing at (30 minutes, 45 ℃), (Blue) $scCO_2$ annealing at (45 minutes, 45 ℃) and (Magenta) $scCO_2$ annealing at (60 minutes, 45 ℃)

Figure 3.5 shows XRD patterns at different $scCO_2$ annealing times of perovskite films. At constant pressure in the $scCO_2$ annealing region, the tetragonal phase perovskites were present and were consistent through increasing times. There was no degradation of the perovskite with an increase in annealing time. The results suggested that annealing times above 15 minutes did not have a significant impact on the film quality.
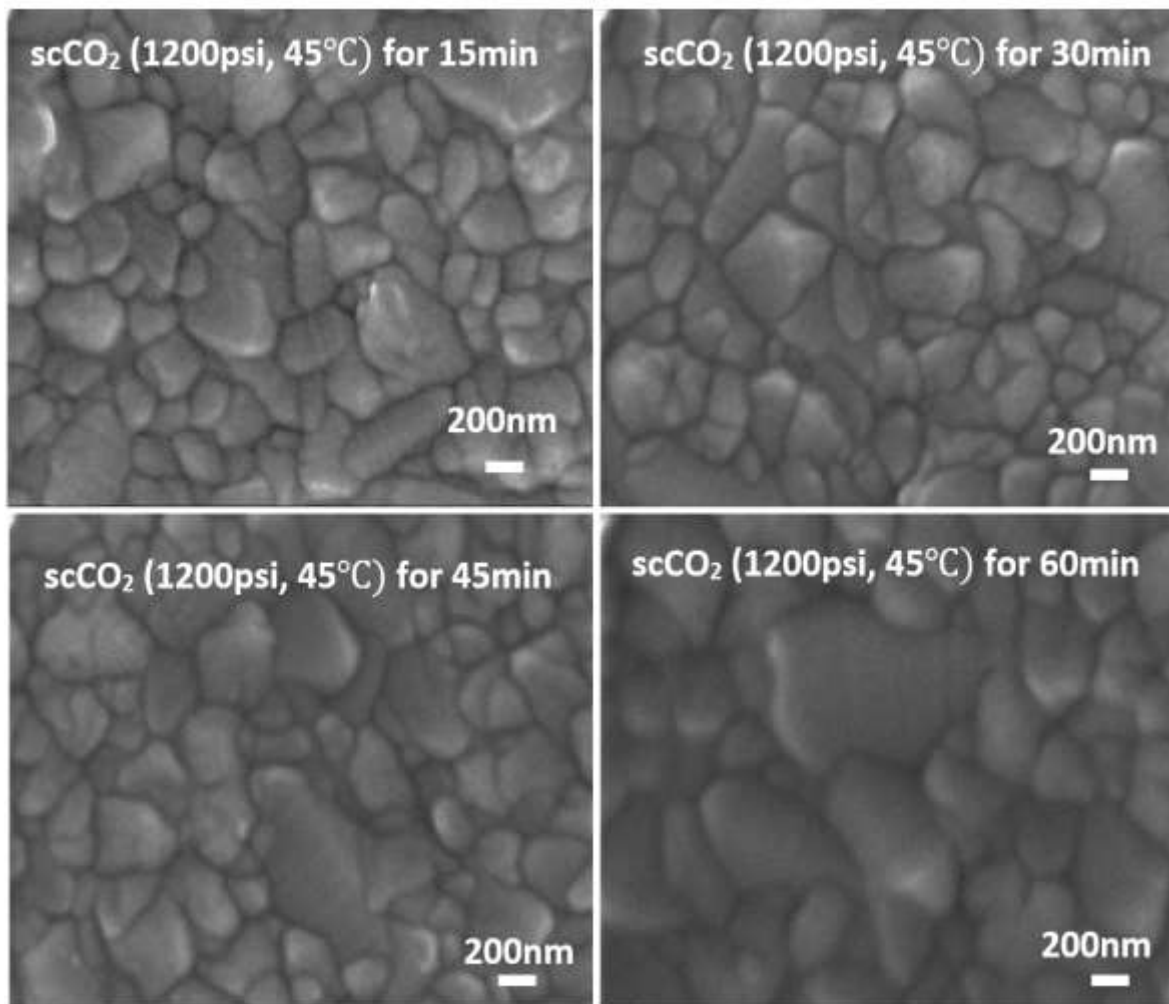
Figure 3.6: SEM images of perovskite films at different annealing times in the $scCO_2$ region

Figure 3.6 shows the SEM images of the top surfaces of perovskite films corresponding to an increase in $scCO_2$ annealing times at constant pressure. From these figures, it can be inferred that perovskite crystals are formed and are dense and uniform with $scCO_2$ annealing. Increasing time did not offer much change in the morphology of the perovskite thin films. The average grain size slightly increased as $scCO_2$ annealing time increased as shown in Figure 3.7 - A. The average grain size increased with $scCO_2$ annealing of 1200psi, 45°C from 408nm at 15 minutes treatment time to 444nm at 60 minutes treatment time.
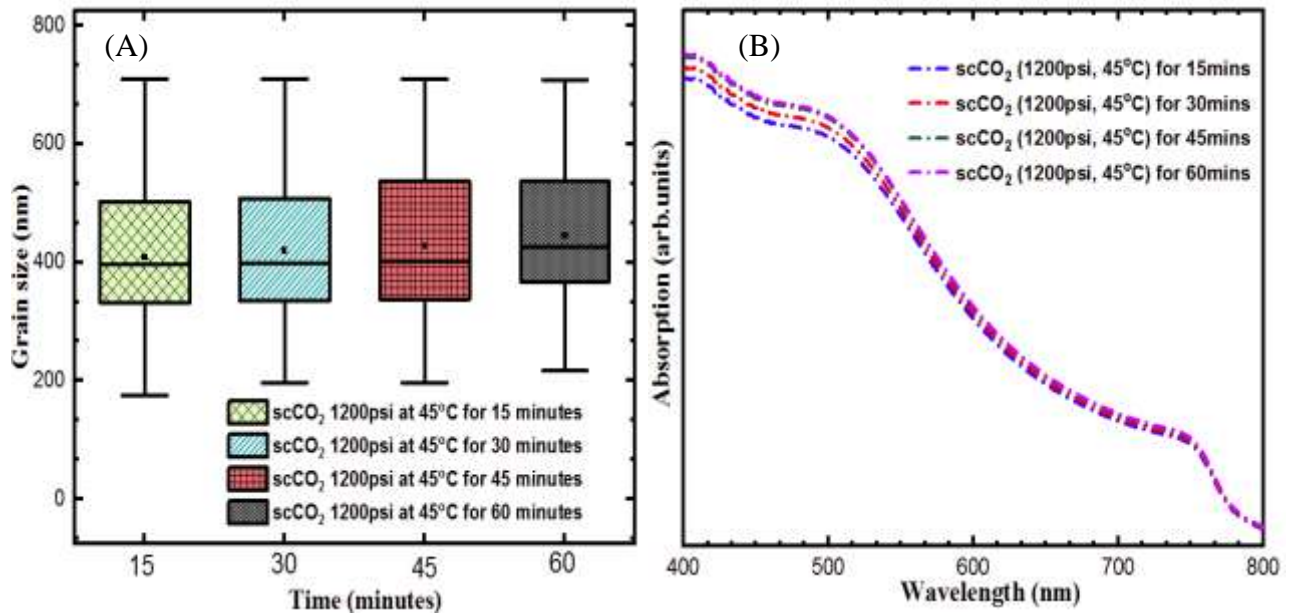
Figure 3.7: (A) Effect of $scCO_2$ annealing time on grain size, (B) Optical absorption spectra at different $scCO_2$ annealing times

Figure 3.7 - B shows the optical absorption spectra due to $scCO_2$ annealing at different times to investigate its effect. Increase in $scCO_2$ annealing time resulted in slightly better absorbance due to larger grain size and greater film uniformity. The structural and optical properties of perovskite prepared over a range of compositions at temperatures, 40°C to 190°C, for 30 minutes in

a dry nitrogen atmosphere were previously investigated [19]. 30 minutes was found to be sufficient to complete the reaction in the perovskite thin films at temperatures of about 100℃. However, below 100°C the reduced film quality and longer required annealing time made it impractical. In this work, the $CH_3NH_3PbI_3$ perovskite films prepared by $scCO_2$ showed complete crystallization at shorter treatment times and lower temperatures with no degradation.

3.5 Effect in increase in $scCO_2$ treatment temperature
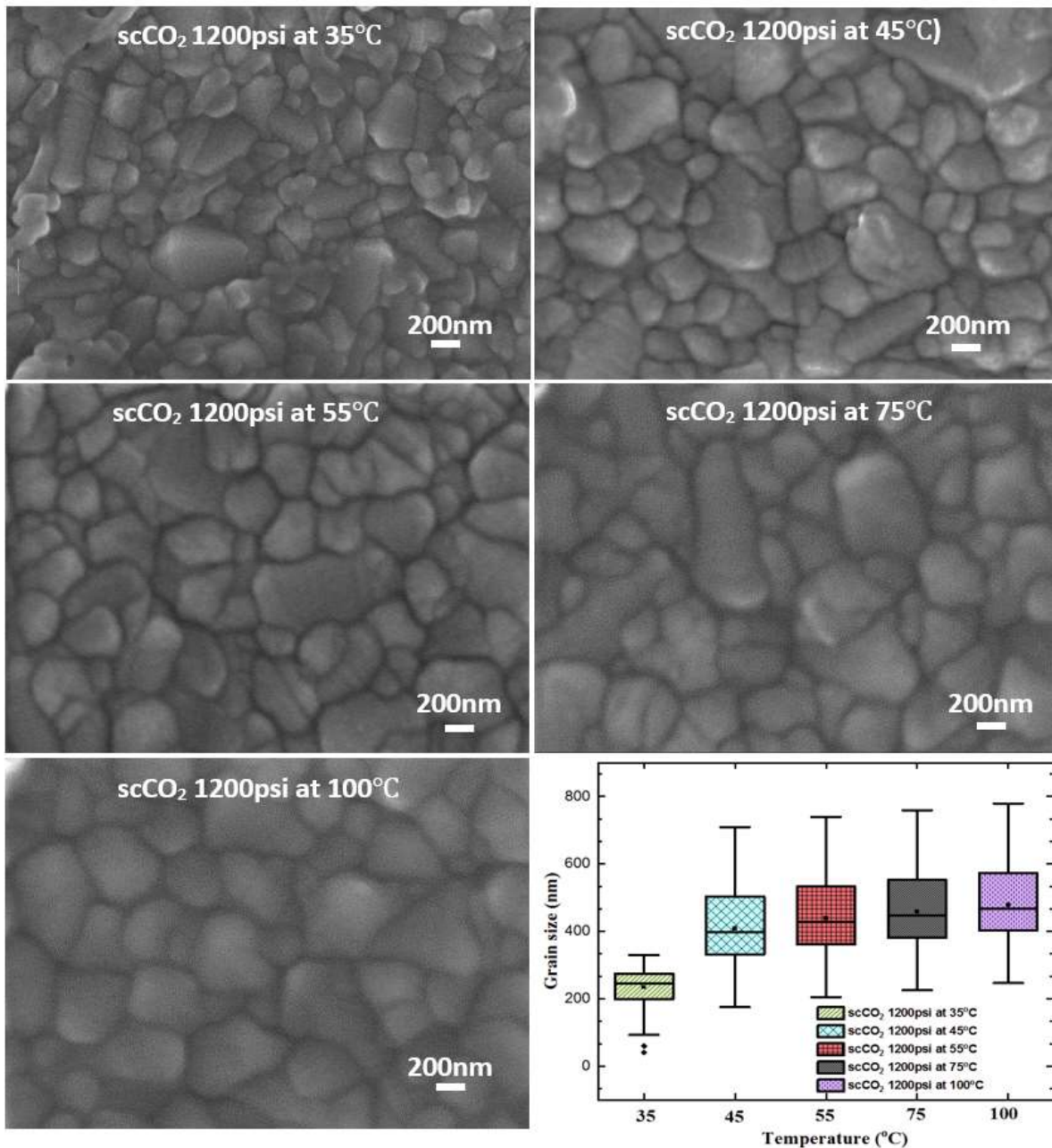
Figure 3.8: SEM images of the perovskite thin film with increasing $scCO_2$ annealing

temperatures for 15 minutes with corresponding average grain sizes

With increasing temperatures in the $scCO_2$ region, the average grain size increased slightly. The average grain size increased from 126nm at 35℃ to 404nm at 100℃ for 15 minutes annealing time. The average grain size increased from 234nm at 35℃ to 478nm at 100℃ for 15 minutes $scCO_2$ annealing time as shown in Figure 3.8. In another study, perovskite formation was investigated in the temperature range of 40–160 ℃ for solution-processed perovskites [20]. Gratzel and Snaith et al. investigated the effect of annealing temperatures on perovskite films prepared using spin coating and found that annealing at 100℃ would effectively reduce the time required for crystallization. Films annealed at temperatures lower than 100℃ showed slow conversion rates and additional absorption shoulders at lower wavelengths. Although annealing temperatures above 100℃ showed a much faster conversion of perovskite crystals, they exhibited low absorbance and decomposition [3]

References

1. Y. Jiang, C. Wu, L. Li, K. Wang, Z. Tao, F. Gao, W. Cheng, J. Cheng, X.Y. Zhao, S. Priya, W. Deng, All electrospray printed perovskite solar cells, Nano Energy. 53 (2018) 440–448. doi:10.1016/j.nanoen.2018.08.062.

2. G.E. Eperon, V.M. Burlakov, P. Docampo, A. Goriely, H.J. Snaith, Morphological control for high performance, solution-processed planar heterojunction perovskite solar cells, Adv. Funct. Mater. 24 (2014) 151–157. doi:10.1002/adfm.201302090.

3. A. Dualeh, N. Tétreault, T. Moehl, P. Gao, M.K. Nazeeruddin, M. Grätzel, Effect of annealing temperature on film morphology of organic-inorganic hybrid pervoskite solid-state solar cells, Adv. Funct. Mater. 24 (2014) 3250–3258. doi:10.1002/adfm.201304022.

4. Z. Xiao, Q. Dong, C. Bi, Y. Shao, Y. Yuan, J. Huang, Solvent Annealing of Perovskite-Induced Crystal Growth for Photovoltaic-Device Efficiency Enhancement, Adv. Mater. 26 (2014) 6503–6509. doi:10.1002/adma.201401685.

5. J. Liu, C. Gao, X. He, Q. Ye, L. Ouyang, D. Zhuang, C. Liao, J. Mei, W. Lau, Improved Crystallization of Perovskite Films by Optimized Solvent Annealing for High Efficiency Solar Cell, ACS Appl. Mater. Interfaces. 7 (2015) 24008–24015. doi:10.1021/acsami.5b06780.

6. K.-L. Wang, C.-C. Zhang, Y.-R. Jiang, H.-R. Liu, X.-M. Li, S.M. Jain, H. Ma, High-quality perovskite films via post-annealing microwave treatment, New J. Chem. (2019) 36–38. doi:10.1039/c8nj05941a.

7. Excitation of Wet Perovskite Films by Ultrasonic Vibration Improves the Device Performance, Appl. Sci. 8 (2018) 308. doi:10.3390/app8020308.

8. H. Xiong, F. Zabihi, H. Wang, Q. Zhang, M. Eslamian, Grain engineering by ultrasonic substrate vibration post-treatment of wet perovskite films for annealing-free, high performance, and stable perovskite solar cells, Nanoscale. 10 (2018) 8526–8535. doi:10.1039/c8nr00540k.

9. J. Xiao, Y. Yang, X. Xu, J. Shi, L. Zhu, S. Lv, H. Wu, Y. Luo, D. Li, Q. Meng, Pressure-assisted CH3NH3PbI3 morphology reconstruction to improve the high performance of perovskite solar cells, J. Mater. Chem. A. 3 (2015) 5289–5293. doi:10.1039/c4ta06700b.

10. G. Annohene, G.C. Tepper, The Journal of Supercritical Fluids Low temperature formation of $CH_3NH_3PbI_3$ perovskite films in supercritical carbon dioxide, J. Supercrit. Fluids. 154 (2019) 104604. doi:10.1016/j.supflu.2019.104604.

11. N. Ahn, D.Y. Son, I.H. Jang, S.M. Kang, M. Choi, N.G. Park, Highly Reproducible Perovskite Solar Cells with Average Efficiency of 18.3% and Best Efficiency of 19.7% Fabricated via Lewis Base Adduct of Lead(II) Iodide, J. Am. Chem. Soc. 137 (2015) 8696–8699. doi:10.1021/jacs.5b04930.

12. D. Shen, X. Yu, X. Cai, M. Peng, Y. Ma, X. Su, L. Xiao, D. Zou, Understanding the solvent-assisted crystallization mechanism inherent in efficient organic-inorganic halide perovskite solar cells, J. Mater. Chem. A. 2 (2014) 20454–20461. doi:10.1039/c4ta05635c.

13. D. Acuna, B Krishnan, S. Shaji, S. Sepulveda, J. L. Menchaca, Growth and properties of lead Iodide thin films by spin coating, Bull. Mater. Sci., Vol. 39, No. 6, October 2016, pp. 1453–1460. DOI 10.1007/s12034-016-1282-z

14. L. Etgar, P. Gao, Z. Xue, Q. Peng, A. K. Chandiran, B. Liu, M. K. Nazeeruddin, M. Gratzel, Mesoscopic $CH_3NH_3PbI_3$/TiO_2 Heterojunction Solar Cells. J. Am. Chem. Soc. 2012, 134, 17396−17399. dx.doi.org/10.1021/ja307789s

15. M. Li, B. li, G. Cao, J. Tian, Monolayer MAPbI3 film for high-efficiency solar cells via coordination and heating assistance process. J. Mater. Chem. A. 5 (2017).10.1039/C7TA06766F.

16. T. Song, Q. Chen. H. Zhou, C. Jiang, H. Wang, Y. Yang, Y. Liu, J. You. Perovskite solar cells: Film formation and properties. J. Mater. Chem. A. 3. (2015). 10.1039/C4TA05246C.

17. Y. Zhou, M. Yang, A.L. Vasiliev, H.F. Garces, Y. Zhao, D. Wang, S. Pang, K. Zhu, N.P. Padture, Growth control of compact CH3NH3PbI3 thin films via enhanced solid-state

precursor reaction for efficient planar perovskite solar cells, J. Mater. Chem. A. 3 (2015) 9249–9256. doi:10.1039/c4ta07036d.

18. Y. Wang, T. Zhang, F. Xu, Y. Li, Y. Zhao, A Facile Low Temperature Fabrication of High Performance $CsPbI_2Br$ All-Inorganic Perovskite Solar Cells, Sol. RRL. 2 (2018) 1-6. 1700180. doi:10.1002/solr.201700180.

19. Z. Song, S.C. Watthage, A.B. Phillips, B.L. Tompkins, R.J. Ellingson, M.J. Heben, Impact of Processing Temperature and Composition on the Formation of Methylammonium Lead Iodide Perovskites, Chem. Mater. 27 (2015) 4612–4619. doi:10.1021/acs.chemmater.5b01017.

20. N.J. Jeon, J.H. Noh, W.S. Yang, Y.C. Kim, S. Ryu, J. Seo, S. Il Seok, Compositional engineering of perovskite materials for high-performance solar cells, Nature. 517 (2015) 476–480. doi:10.1038/nature14133.

CHAPTER 4

EFFECT OF SUPERCRITICAL CARBON DIOXIDE PLUS ORGANIC COSOLVENT ON $CH_3NH_3PbI_3$ FILMS

4.1 Introduction

Supercritical carbon dioxide annealing of $CH_3NH_3PbI_3$ films promotes solid-state crystallization by reducing the energy barrier for molecular diffusion, thereby promoting crystal rearrangement into the low energy perovskite structure [1] [2] [3] [4]. In this chapter, the report is extended to include the addition of various organic cosolvents to the $scCO_2$ for post-deposition annealing of the $CH_3NH_3PbI_3$ perovskite films. The solvent power of $scCO_2$ is generally poor due to the low polarity of CO_2 molecules resulting in weak film-solvent interactions [5]. Joshi and Prausnitz proposed that the introduction of another solvent(s) (cosolvent or entrainer) to $scCO_2$ could form preferential intermolecular interactions with solutes and increase the solvent polarity [6]. This provided grounds for many studies for determining the solubility of different solutes in $scCO_2$ with different cosolvents experimentally [7] [8] and theoretically [9] [10]. The cosolvent effect promotes intermolecular interactions (such as dipole-dipole, dipole-induced dipole, or induced dipole-induced dipole interactions between the cosolvent and solute) and specific chemical interaction (E.g. hydrogen-bonding or charge transfer complex formation), [5] [11] [12].

The effect of $scCO_2$ + cosolvent annealing on the morphology, crystallinity, and optical absorption of $CH_3NH_3PbI_3$ perovskite films is reported in this chapter. The cosolvents used were fully soluble in $scCO_2$ at the concentrations used, thus forming a binary single-phase supercritical

fluid [11] [13] [14] [15]. To understand the influence of hydrogen-bonding interactions, the solvents were characterized qualitatively as poorly, moderately, or strongly hydrogen-bonded as shown in Table 4.1 [16]. To better comprehend the interactions of the cosolvent with the perovskite film, Table 4.1 also contains the results of solubility tests of the pure cosolvents with CH_3NH_3I and PbI_2. As expected, the weakly polar aromatic compounds (Toluene and Benzene) with the lowest propensity for hydrogen bonding were the weakest solvents to the perovskite film followed by the moderately polar (Tetrahydrofuran and Acetone) and more polar (alcohols and ethylene glycol) compounds.

Strength of H-bond	Solvent	PbI_2	CH_3NH_3I
Poor	Toluene	Not soluble	Not soluble
	Benzene	Not soluble	Not soluble
Moderate	Tetrahydrofuran	Partially soluble	Not soluble
	Acetone	Partially soluble	Not soluble
Strong	Ethanol	Not soluble	Completely soluble
	Methanol	Not soluble	Completely soluble
	Ethylene glycol	Partially soluble	Completely soluble

Table 4.1: Solubility test of organic solvents on CH_3NH_3I and PbI_2

4.2 Experimental Method

4.2.1 Materials and precursor preparation

Bone Dry 3.0 Grade Carbon Dioxide with siphon from Airgas was used. $CH_3NH_3PbI_3$ was synthesized by mixing a 1:1:1 molar ratio of 2.385g of methylammonium iodide (CH_3NH_3I) (98%,

Sigma Aldrich), 6.915g of lead (II) iodide (PbI_2) (99.9985%, Alfa Aesar), and 1.063 mL of dimethyl sulfoxide (DMSO) ($\geq$ 99.9%, anhydrous, Sigma Aldrich) in 9.484mL of N,N-dimethylformamide (DMF) ($\geq$ 99.8%, anhydrous, Sigma Aldrich) and 0.3mL of diethyl ether (anhydrous, Acros Organics). The solution was processed in an argon-filled glovebox, stirred at room temperature for 1 hour, and filtered with a 0.2μm syringe filter (Corning) [17]. Ethylene glycol (anhydrous, 99.8%, Sigma Aldrich), methanol (anhydrous, 99.8%, Sigma Aldrich), tetrahydrofuran (anhydrous, $\geq$ 99.9%, Sigma Aldrich), benzene (anhydrous, 99.8%, Sigma Aldrich), methanol (anhydrous, 99.8%, Sigma Aldrich), Toluene (H_2O 0.004%, Fisher Scientific and acetone, (99.8%, extra dry, Acros Organics) were used as cosolvent for the $scCO_2$.

4.2.2 $CH_3NH_3PbI_3$ perovskite thin film fabrication

Fluorine doped tin oxide (FTO) substrate (12-14Ω, 25mm×25mm×2.2mm, Ossila Limited) was cleaned with detergent, deionized water, acetone, and isopropyl alcohol. The precursor solution was spin coated onto the FTO glass slide at 6000rpm for 25sec. During the spin coating procedure, 0.5mL of diethyl ether was dripped on the rotating surface at the sixth second of the 25 seconds spinning. The perovskite film was placed in a pressure vessel (Parr Instrument Pressure Reactor 4768) and a different (V/V %) of cosolvent was added (0.2%, 0.4%, 0.8%, 1.2%, 1.6%, 2.0%). A syringe pump (Teledyne ISCO Pump 260D) was used to pressurize the CO_2 and cosolvent for crystallization. This experiment was carried out at 45℃ and 8.27 MPa (1200 psi) and a processing time of 15 minutes for each film. Films annealed in pure $scCO_2$ were used as a control for comparison and baseline. In our previous study on perovskite crystallization in pure CO_2 [18], the effect of temperature, pressure, and processing time were evaluated and it was concluded that increasing the temperature, pressure, or processing time in the supercritical fluid did not

significantly change the film morphology. Therefore, in this study, these parameters were fixed to determine the effect of the organic cosolvent. The setup is demonstrated in Figure 4.1.
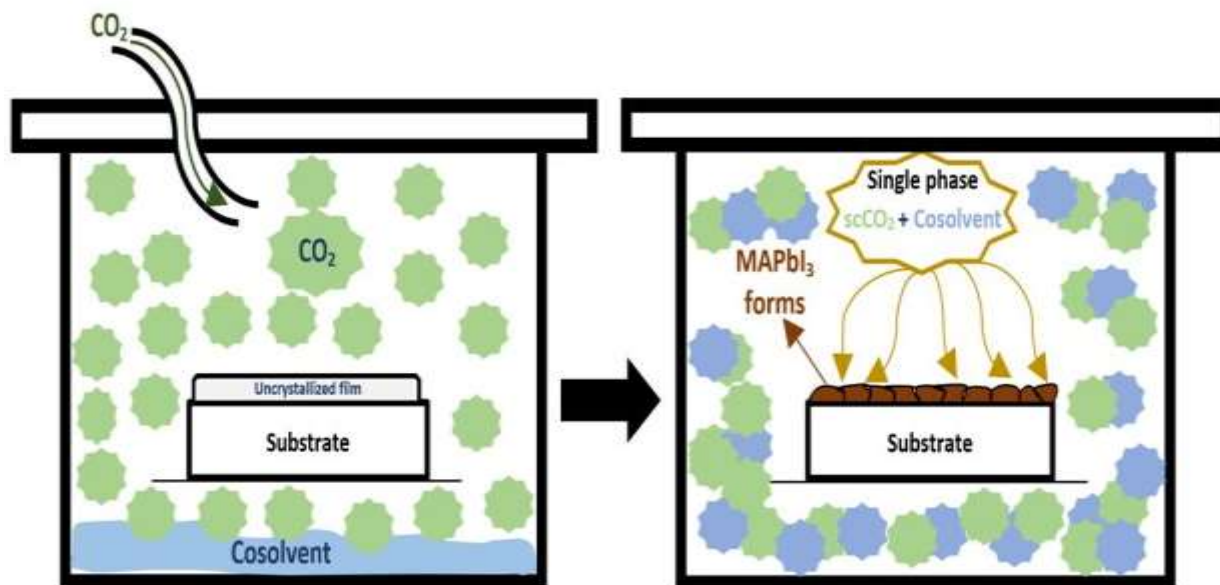
Figure 4.1: Demonstration of $scCO_2$ + Cosolvent setup for annealing $CH_3NH_3PbI_3$ films [18]

4.2.3 Film characterization

The crystallographic properties of the resulting perovskite films were characterized by X-ray diffraction (XRD) measurements (PANalytical MPD X'pert Pro), using a Cu Kα ($\lambda = 1.54$Å) radiation source that operated at 45kV and 40mA. The X-ray diffractograms were obtained at a scan rate of 0.01 °s^{-1} for 2θ values between 10° and 60°. The surface coverage, morphology, and grain size were obtained using a scanning electron microscope (SEM) (Hitachi SU-70 FE-SEM) at 20kV and analyzed using the ImageJ software package. Optical spectrometry of the films was conducted using a spectral response measurement system (PerkinElmer Lambda 35 UV/VIS).

4.3 Effect of Poorly Hydrogen-bonded solvents (Toluene and Benzene)

$CH_3NH_3PbI_3$ film surface morphology after annealing in $scCO_2$+Toluene at different volume ratios was analyzed with SEM images. Figure 4.2 shows the morphology of a film annealed in pure $scCO_2$ without any cosolvent resulted in uniform and high quality films as reported previously [18]. It also shows the morphology of films annealed in $scCO_2$ with the toluene co-solvent at various volume fractions. The addition of toluene did not dissolve either PbI_2 or CH_3NH_3I, but produced measurable changes to the resulting film morphology and average grain size. The grain size distribution of the films annealed in pure $scCO_2$ and $scCO_2$ +Toluene is also shown in Figure 4.2. The average grain size for pure $scCO_2$ was about 400nm. The average grain size of films annealed in $scCO_2$ +Toluene from 0.2 – 0.8 (V/V %) was comparable to that of pure $scCO_2$. However, the average grain size increased dramatically from around 400nm to about 750nm at 1.6 (V/V %) and quickly dropped down to about 400 nm at 2.0 (V/V %). At this time, we do not have an explanation for this trend.

The effect of co-solvent on the film crystallinity was studied using XRD. Figure 4.3 - A shows that the diffraction peaks (phase) after annealing with $scCO_2$ +Toluene annealed remained similar to those of using $scCO_2$ without any cosolvent. Complete crystallization was observed for all samples with no visible PbI_2 peak. The diffraction peaks at 14.1°, 24.8°, 28.7°, and 32.2°, corresponded to the (110), (202), (220), and (310) planes of crystalline $CH_3NH_3PbI_3$, respectively with a tetragonal crystal structure [1] [19] [20] [21]. Figure 4.3 - B shows the optical absorption spectra for the addition of toluene co-solvent. The overall shape of the absorption spectra for both co-solvents was similar to pure $scCO_2$ indicating that, the weak hydrogen-bonding interactions of the toluene with the film did not chemically alter the crystal structure or bandgap. The absorption spectra of the films annealed in the toluene co-solvent exhibited a strong and somewhat random

deviation from the pure $scCO_2$ film, particularly at the shorter wavelengths. Surprisingly, the 1.6% (v/v) toluene film with the largest grain size exhibited lower optical absorption than pure $scCO_2$ at shorter wavelengths.
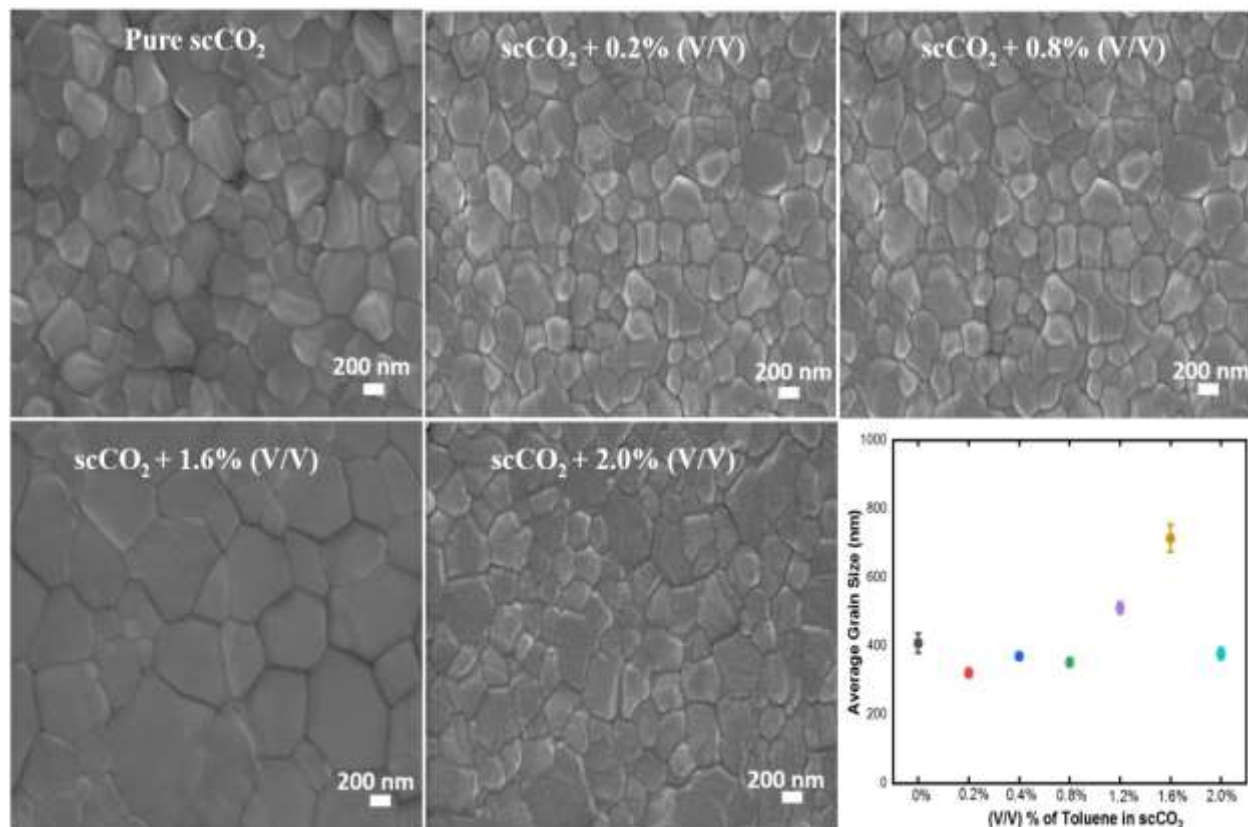
Figure 4.2: SEM images of the top surface of the perovskite film processed at varied $scCO_2$ + % (V/V) toluene with average grain size distribution

In Figure 4.4, SEM images of the $CH_3NH_3PbI_3$ films after annealing in pure $scCO_2$ and $scCO_2$ + Benzene are shown. The addition of different percent volume/volume ratios of benzene resulted in more subtle morphology changes. The average grain size of films with an increase in Benzene cosolvent in $scCO_2$ stayed in the 400nm – 450nm range, which was not a high deviation from the pure $scCO_2$ annealed films.
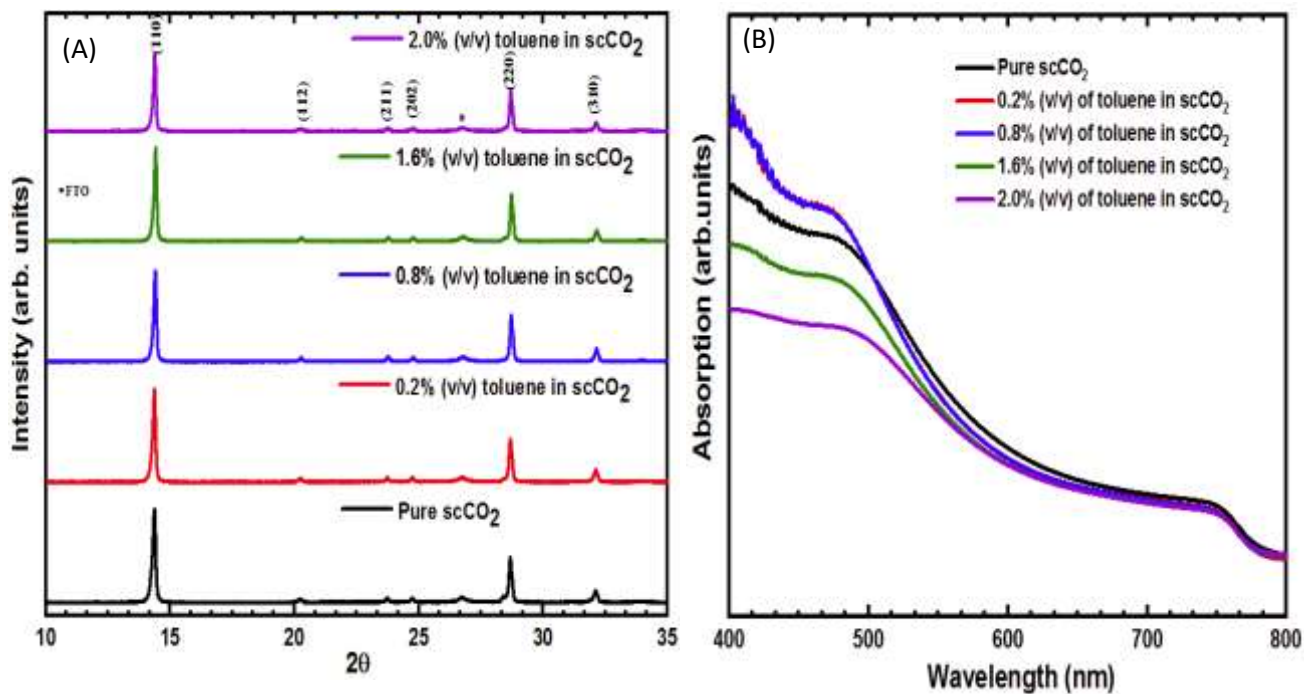
Figure 4.3: A: XRD patterns of the perovskite thin film with pure $scCO_2$ and different (V/V %) of toluene B: Optical absorption spectra of the thin film at different annealing conditions.

The effect of the Benzene co-solvent on the film crystallinity was studied using XRD. Figure 4.5 - A shows that the relative intensity of the diffraction peaks from the different planes did not change, implying that the crystal orientation of $scCO_2$ +Benzene annealed films did not change during annealing. Complete crystallization was observed for all samples with no visible PbI_2 peak. Figure 4.5 - B presents the optical absorption spectra for the benzene co-solvent in comparison to pure $scCO_2$. The overall shape of the absorption spectra was similar to pure $scCO_2$ indicating that the weak hydrogen-bonding interactions of benzene with the film do not chemically alter the crystal structure or bandgap. All of the films treated with the benzene co-solvent exhibited

stronger optical absorption at all wavelengths in comparison to pure $scCO_2$, which usually indicates

better film quality.
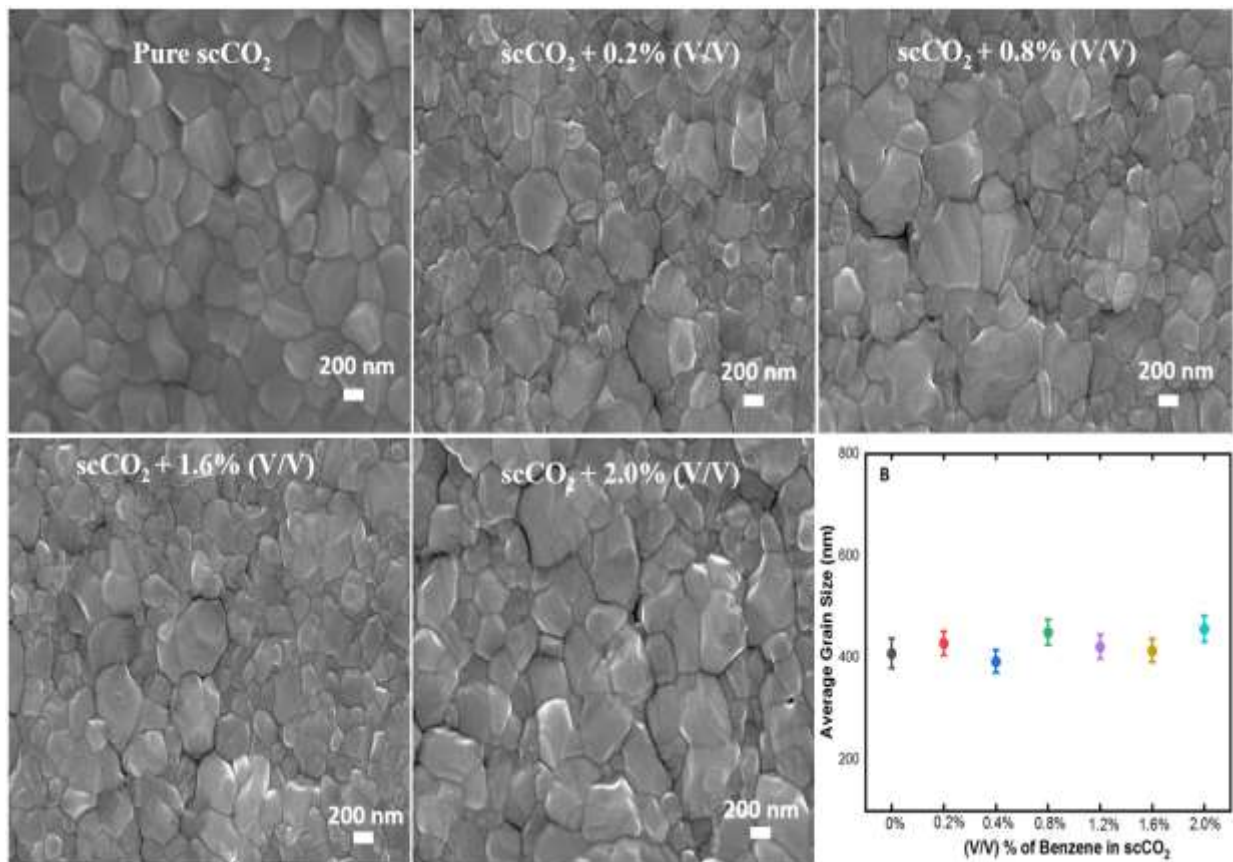
Figure 4.4: SEM images of the top surface of the perovskite film processed at varied $scCO_2$ + %

(V/V) benzene with average grain size distribution
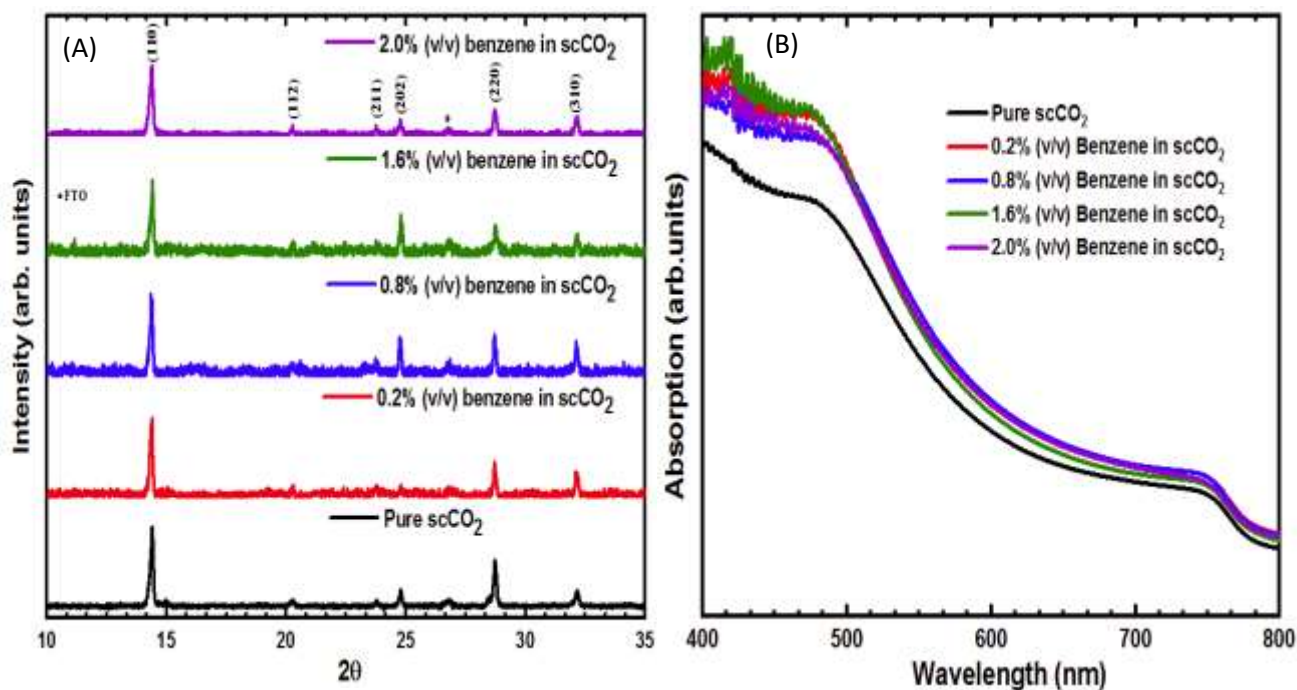
Figure 4.5: A: XRD patterns of the perovskite thin film with pure $scCO_2$ and different (V/V %) of Benzene B: Optical absorption spectra of the thin film at different annealing conditions

4.4 Effect of Moderately Hydrogen-bonded solvents (Tetrahydrofuran and Acetone)

Figures 4.6 and 4.7 shows SEM images of the top surfaces of the perovskite thin films after annealing in $scCO_2$ + THF and $scCO_2$ + Acetone. Earlier reports showed that as the concentration of PbI_2 in the perovskite film was reduced, the quality of the film uniformity was compromised leading to a porous film [22]. From the SEM images, we see a smooth and compact morphology with annealing in pure $scCO_2$. However, with the addition of THF and acetone, the morphology of the film was dramatically altered, with an increasing number of pinhole defects correlating with an increase in the percent volume of the cosolvent. This is most likely due to the selective interaction of these cosolvents with PbI_2. The morphology of $scCO_2$ + THF annealed films

appeared to be less defective with increasing cosolvent volume than that of acetone possibly due to the lower solubility parameter of the former resulting in a weaker interaction with PbI_2.
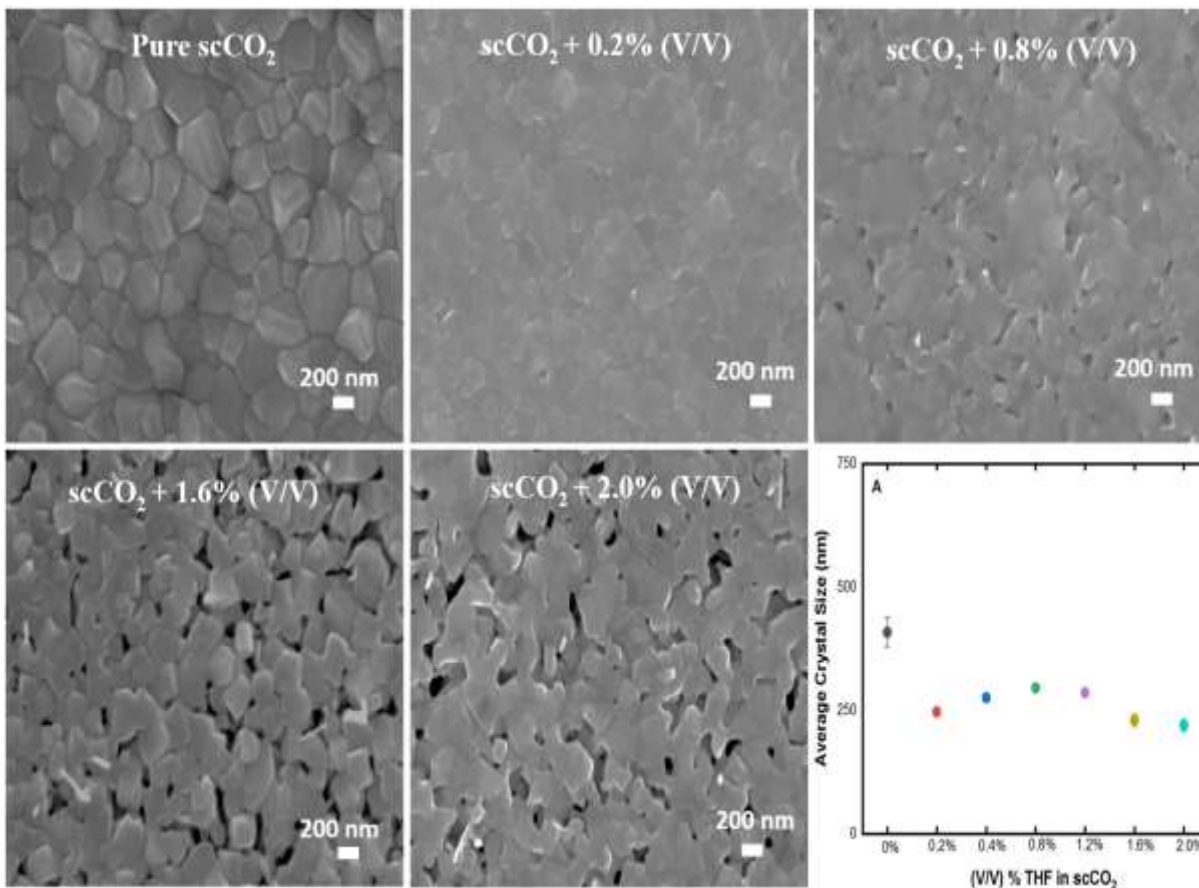
Figure 4.6: SEM images of the top surface of the perovskite film processed at varied $scCO_2 + \%$ (V/V) tetrahydrofuran with average grain size distribution

The grain size distribution of the films was obtained for pure $scCO_2$, $scCO_2 + THF$ and $scCO_2 +$ Acetone as shown in Figures 4.6 and 4.7. With the addition of THF and Acetone, the average grain size was slightly lower than that of pure $scCO_2$ films. This could be due to a disturbance of the interdiffusion of PbI_2 or CH_3NH_3I because of solubility interactions of the PbI_2

with the cosolvents. The film annealed in $scCO_2 + 2\%$ (v/v) acetone did show a larger average grain size, but inspection of the SEM image of that film showed the emergence of very large grains (cuboids) that appeared to be crystalline, but the overall film quality was poor.
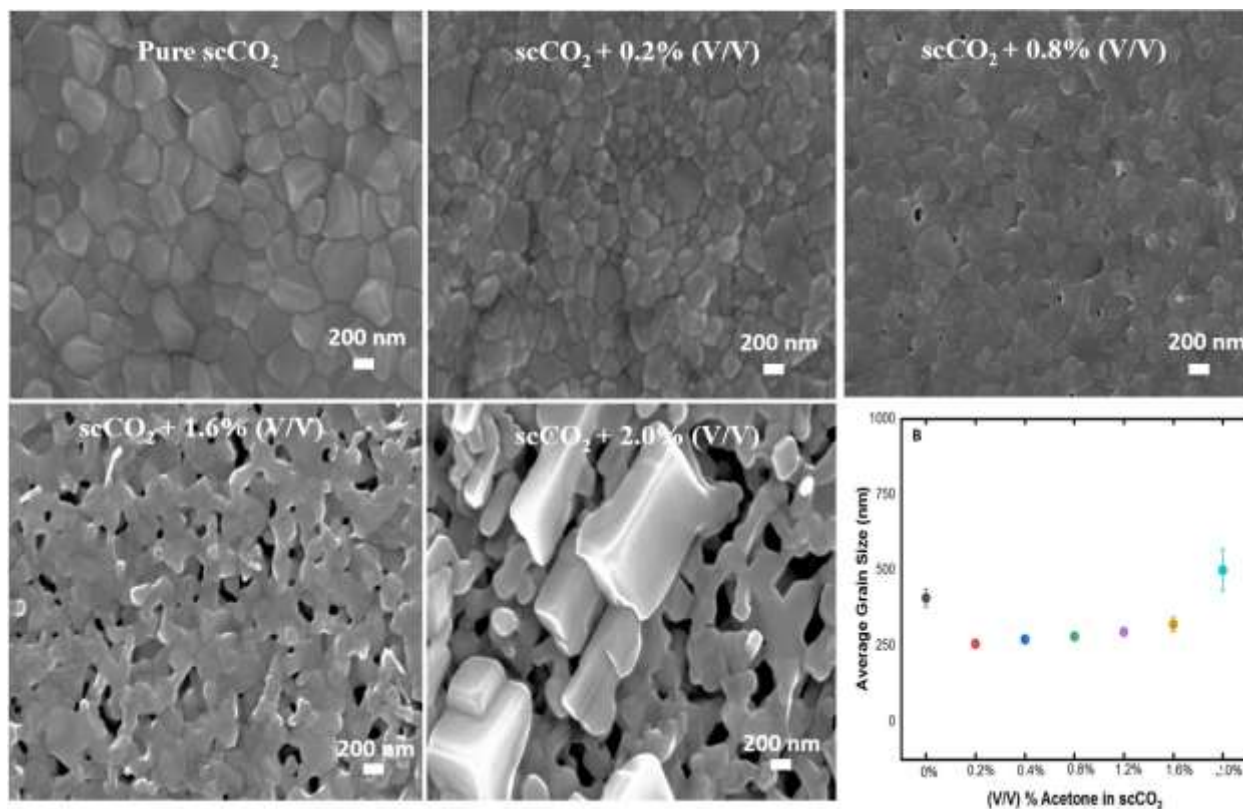
Figure 4.7: SEM images of the top surface of the perovskite film processed at varied $scCO_2 + \%$ (v/v) acetone with average grain size distribution

Figure 4.8 - A and Figure 4.9 - A shows the relative intensity of the diffraction peaks for $scCO_2 + THF scCO_2 +$ acetone processed films. The crystal structure did not change after annealing with these cosolvents. However, with a 0.8% (v/v) ratio of THF in $scCO_2$, the preferential orientation shifted from the (110) plane to the (202) plane. In addition, there was a similar shift in

72

1.6% (v/v) ratio of Acetone in $scCO_2$. The preferred reorientation in the perovskite film could be related to the nucleation dynamics during crystal formation with PbI_2 specific rearrangement [23] [24] [25]. These would then be possible due to the assistance of these moderately H-bonded cosolvents with the film causing crystal lattice distortion. However, the unsystematic reorientation to the (202) plane with increasing (v/v) cosolvent ratio is not understood at this moment.
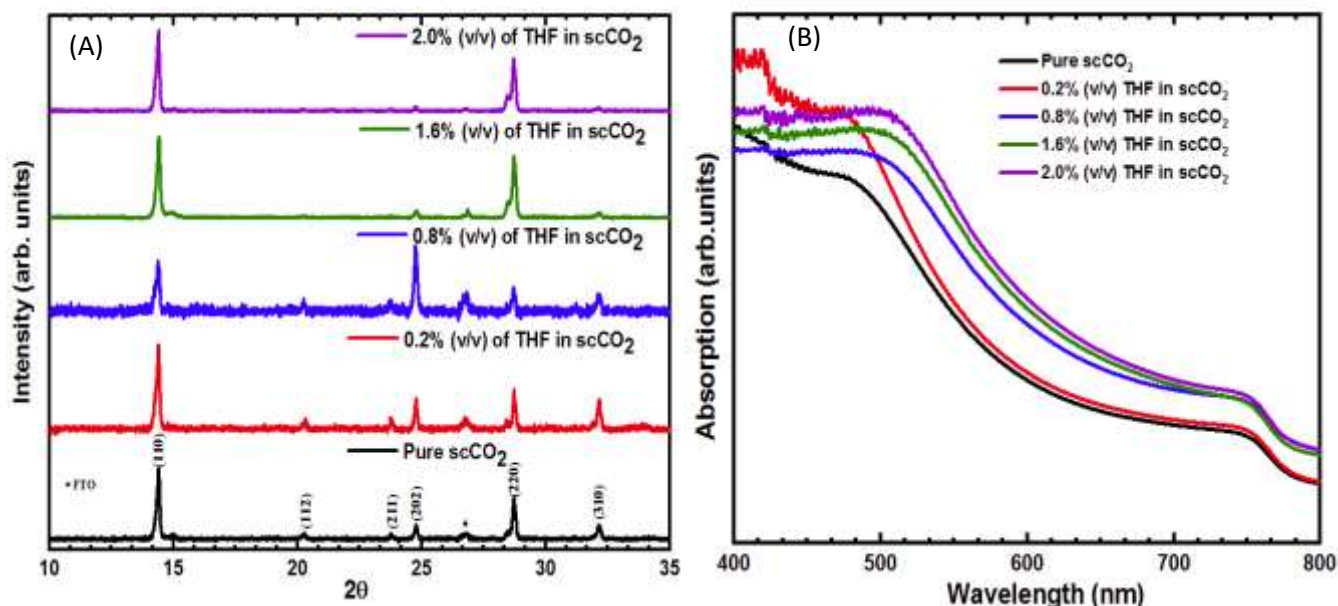
Figure 4.8: A: XRD patterns of the perovskite thin film with pure $scCO_2$ and different (v/v %) of tetrahydrofuran B: Optical absorption spectra of the thin film at different annealing conditions.

Figure 4.8 - B and Figure 4.9 - B presents the evolution of the optical absorption spectra. From this, we noticed a similar overall shape of the $scCO_2$ + THF and $scCO_2$ + acetone annealed films to that of pure $scCO_2$ indicating that the moderately hydrogen-bonded interactions of the THF and acetone did not chemically alter the crystal structure and bandgap. Although the film morphology was not smooth, with increasing volume percent of cosolvents, the absorption

increased relative to that of pure $scCO_2$. This could be attributed to scattering, which was not accounted for and/or possibly due to the moderately hydrogen-bonded cosolvent interactions resulting in a denser but less uniform film.
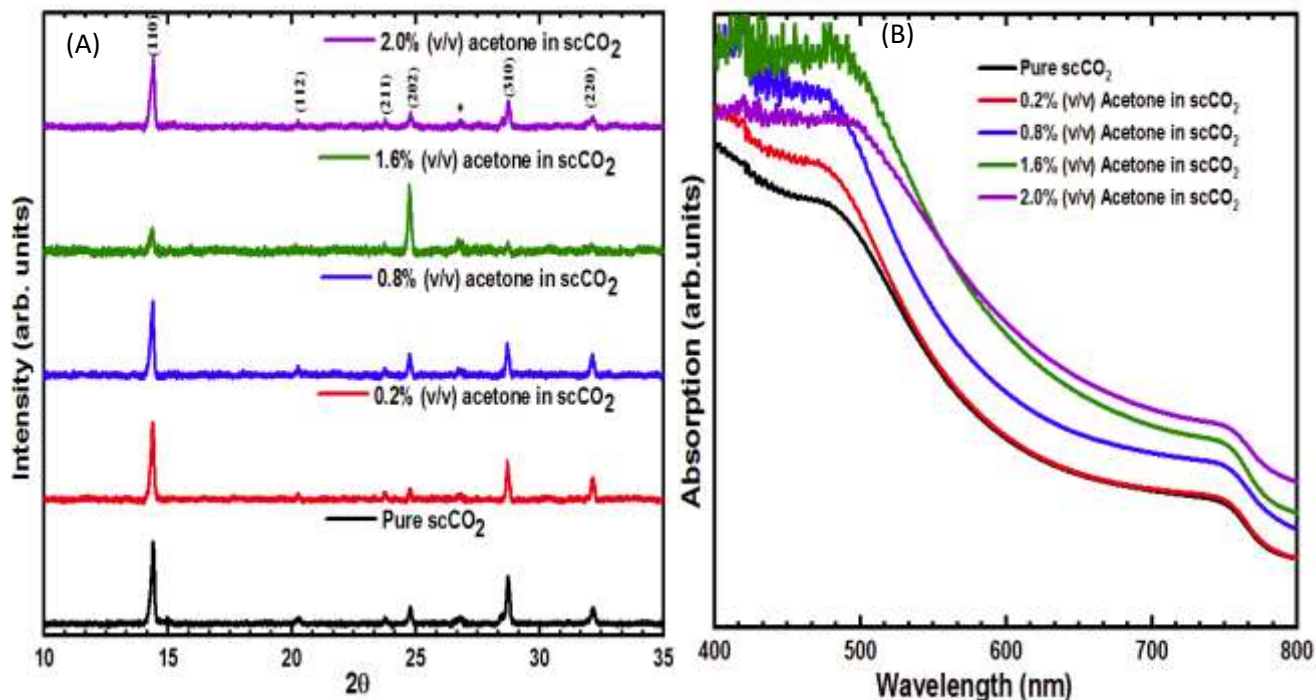
Figure 4.9: A: XRD patterns of the perovskite thin film with pure $scCO_2$ and different (v/v)% of acetone B: Optical absorption spectra of the thin film at different annealing conditions.

4.4 Effect of Strongly Hydrogen-bonded solvents (Ethanol, Methanol and Ethylene Glycol)

Figures 4.10, 4.11 and 4.12 show SEM images of the top surfaces of the perovskite thin films after annealing with $scCO_2$ + ethanol, $scCO_2$ + methanol, and $scCO_2$ + ethylene glycol respectively. The CH_3NH_3I precursor was soluble in each of these cosolvents and it has been shown that as the concentration of CH_3NH_3I was reduced, $CH_3NH_3PbI_3$ cuboids began to form [26]. The size of the cuboids increased with decreasing concentration of CH_3NH_3I with an average

dimension exceeding 1µm. From the figures, we see a smooth and compact morphology with annealing in pure $scCO_2$. However, with the addition of ethanol, methanol, and ethylene glycol cosolvent to $scCO_2$, we see diverse and noticeable changes in film morphology, ranging from smooth, compact, and homogeneous grains to cuboids, hexagonal grains, and large shapeless grains due to the strong hydrogen bonding interaction.
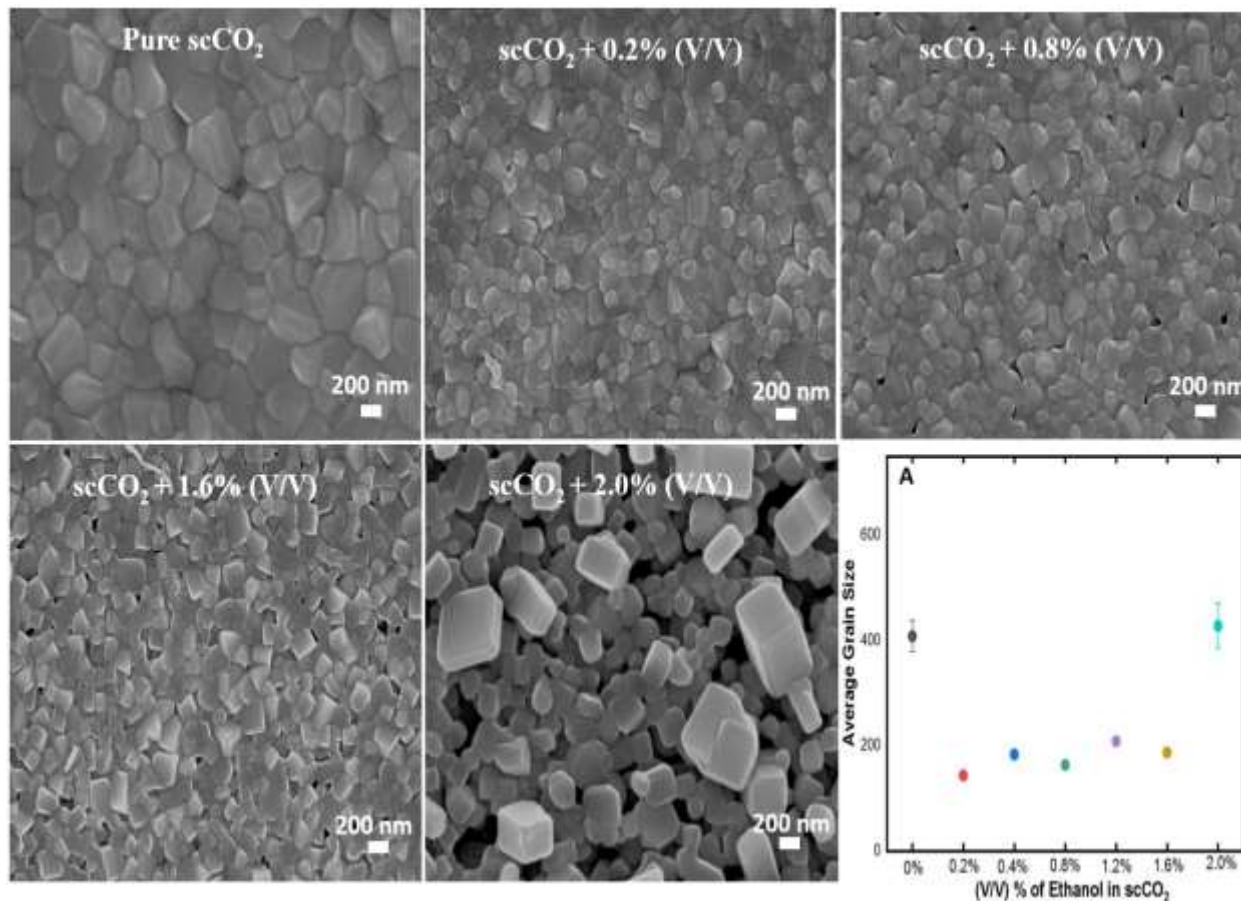
Figure 4.10: SEM images of the top surface of the perovskite film processed at varied $scCO_2$ + % (v/v) ethanol with average grain size distribution
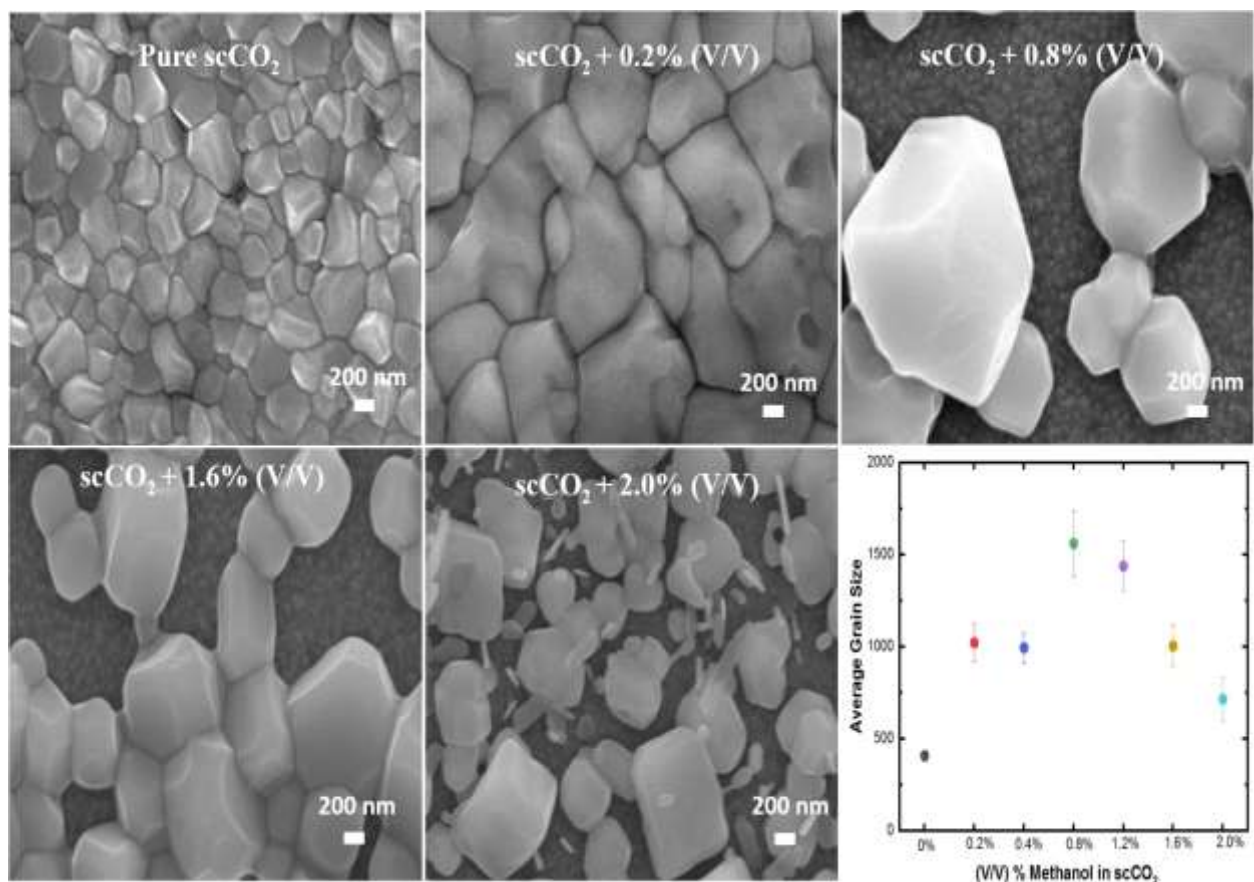
Figure 4.11: SEM images of the top surface of the perovskite film processed at varied $scCO_2$ + % (v/v) methanol with average grain size distribution

The formation of the cuboids in Figures 4.11 and 4.12 was likely due to the selective interactions of these cosolvents with CH_3NH_3I since it was soluble in them. PbI_2 is not soluble in ethanol and methanol and this could account for the smoothness of these films at low volume percent. However, as the volume percent increased, large micron-size rounded or cubic shapes emerged. Ethylene glycol is a weak solvent for PbI_2 and a solvent for CH_3NH_3I leading to a combined effect with solubility interactions with both precursors. It can be noted that as the

solubility parameter of these strongly hydrogen-bonded solvents increased (ethanol to methanol to ethylene glycol) the interactions with the film constituents increased leading to more dramatic changes in film morphology.
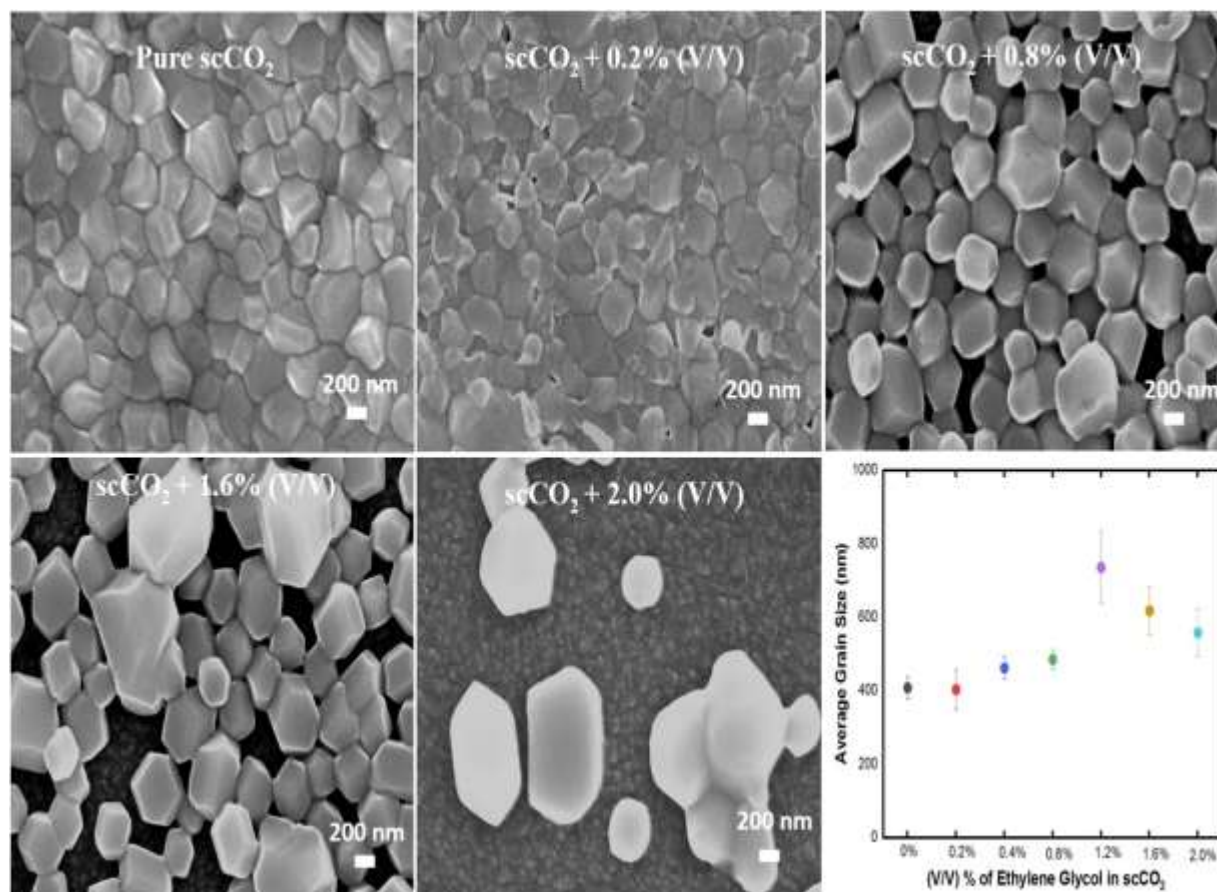
Figure 4.12: SEM images of the top surface of the perovskite film processed at varied $scCO_2$ + % (v/v) ethylene glycol with average grain size distribution

The grain size distribution of the films were obtained for pure $scCO_2$ processing and $scCO_2$ + ethanol, $scCO_2$ + methanol and $scCO_2$ +ethylene glycol as shown in Figures 4.10, 4.11, and 4.12. With the addition of ethanol, the average grain size is slightly lower than that of pure $scCO_2$ films

and jumps back up when the cuboids begin to form. When methanol and ethylene glycol were added, the average grain size increased but became non-uniform and riddled with defects.
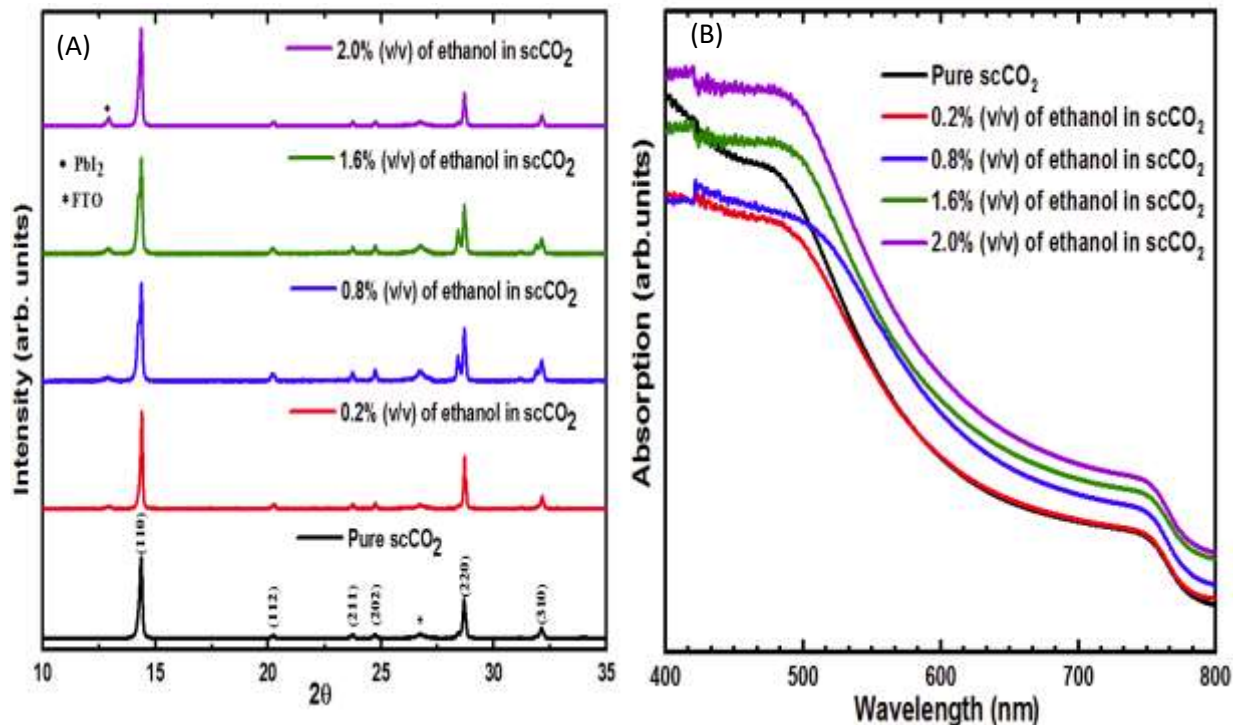
Figure 4.13: A: XRD patterns of the perovskite thin film with pure $scCO_2$ and different (v/v %) of Ethanol B: Optical absorption spectra of the thin film at ethanol annealing conditions.

Figures 4.13 – A, 4.14 – A, and 4.15 - A shows that the relative intensity of the X-ray diffraction peaks of $scCO_2$ +ethanol, $scCO_2$ +methanol, and $scCO_2$ +ethylene annealed films respectively. With ethanol, we noticed that the overall crystal structure was not compromised until at $scCO_2 + 0.8\%$ (v/v), the peak associated with PbI_2 became visible. It can be concluded that there is a strong chemical interaction of ethanol with the perovskite crystal, which initiates degradation. With methanol, all of the samples presented the same diffraction peaks corresponding to planes of

crystalline $CH_3NH_3PbI_3$. A significant peak located at 12.6° corresponding to the diffraction from (001) lattice plane of PbI_2 hexagonal polytype appears [27] [28]. It has been indicated that a little residual PbI_2 can bring about a passivation effect in PSCs to improve photovoltaic performance [29]. Nevertheless, in general, excess of PbI_2 has a negative impact and impedes carrier transport. With ethylene glycol, tetragonal crystal structure is seen up to 0.8% (v/v) ratio in $scCO_2$. Once the volume of ethylene glycol exceeded this point, we noticed that the dominant peak shifted from (110) to the (224) plane possibly due to CH_3NH_3I assisted reorientation of PbI_2 peak of (001) [30].
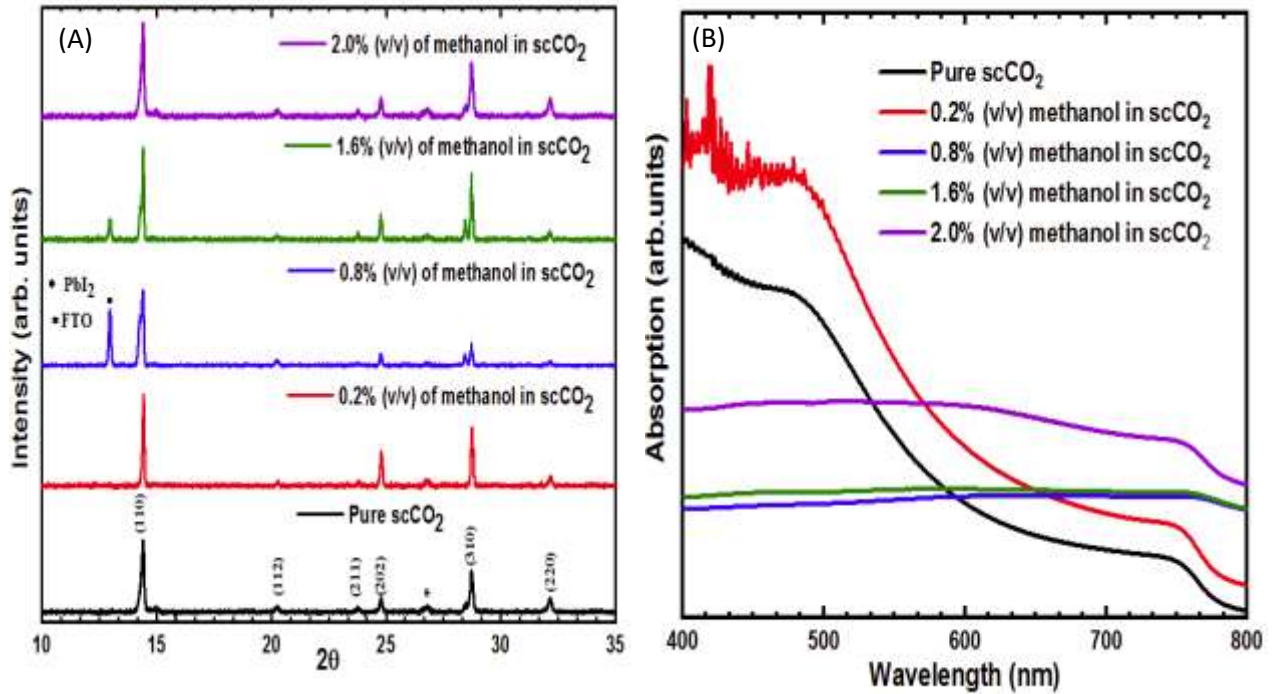
Figure 4.14: A: XRD patterns of the perovskite thin film with pure $scCO_2$ and different (v/v %) of Methanol B: Optical absorption spectra of the thin film at methanol annealing conditions.

Figures 4.13 – B, 4.14 – B, and 4.15 - B presents the evolution of the optical absorption spectra of $scCO_2$ + ethanol, $scCO_2$ + methanol, and $scCO_2$ + ethylene glycol processed films respectively. The overall shape of the optical absorption spectra for the ethanol cosolvent was similar to that of pure $scCO_2$ but did not follow a trend with increasing or decreasing cosolvent volume percent. Interestingly, for the films processed in both the methanol and ethylene glycol cosolvents, the films became optically transparent above a certain cosolvent volume percent. The XRD patterns for these films still showed the perovskite crystal structure, but the absorption spectra showed optical transparency at all wavelengths and no discernible band edge.
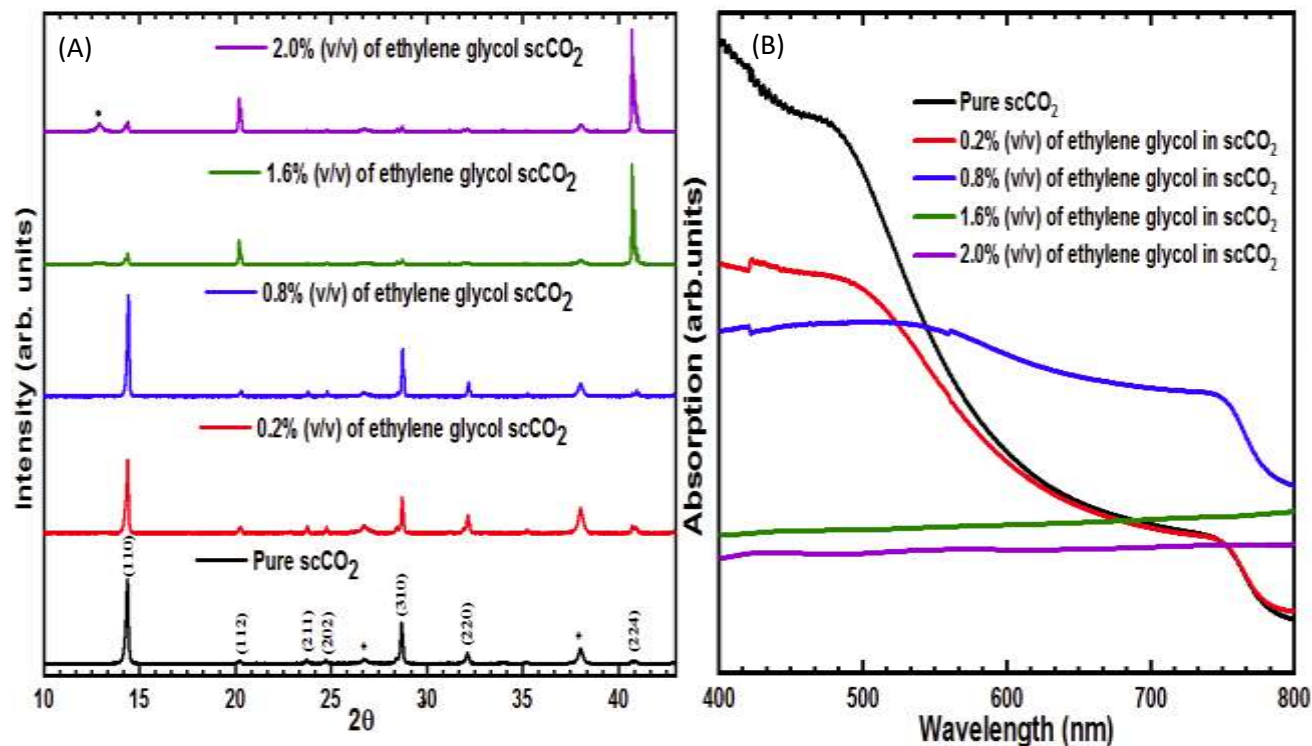
Figure 4.15: A: XRD patterns of the perovskite thin film with pure $scCO_2$ and different (v/v %) of ethylene glycol B: Optical absorption spectra of the thin film at ethylene glycol annealing conditions.

References

1. J. Luo, R.Z. Qiu, Z.S. Yang, Y.X. Wang Q.F Zhang, Mechanism and effect of g-butyrolactone solvent vapor post-annealing on the performance of a mesoporous perovskite solar cell, RSC Advances (2018) 724–731. doi:10.1039/c7ra10695e.

2. S.S. Dinachali, W. Bai, K. Tu, H.K. Choi, J. Zhang, M.E. Kreider, L. Cheng, C.A. Ross, Thermo-Solvent Annealing of Polystyrene-Polydimethylsiloxane Block Copolymer Thin Films, ACS Macro Letters 4 (2015) 500-504. doi:10.1021/acsmacrolett.5b00108.

3. T.P Lodge, M.C Dalvi, Mechanisms of chain diffusion in lamellar block copolymers, Physical R. Letters, 75 (1995) 657–660.

4. K.W. Gotrik, C.A. Ross, Solvothermal Annealing of Block Copolymer Thin Films, Nano Letters 13 (2013) 5117-5122. doi:10.1021/nl4021683.

5. H. Ren, J. Song, Q. Xu, J. Yin, Solubility of the silver nitrate in supercritical carbon dioxide with ethanol and ethylene glycol as double cosolvents: Experimental determination and correlation, Chinese J. Chem. Eng. 27 (2019) 400–404. doi:10.1016/j.cjche.2018.06.011

6. D.K Joshi, J.M Prausnitz, Supercritical Fluid Extraction with Mixed Solvents, AlChE Journal 30, (1984) 522–525.

7. R.G. Bitencourt, F.A. Cabral, A.J.A. Meirelles, Ferulic acid solubility in supercritical carbon dioxide, ethanol and water mixtures, J. Chem. Thermodyn. 103 (2016) 285–291. doi:10.1016/j.jct.2016.08.025.

8. S. Zhan, S. Li, Q. Zhao, W. Wang, J. Wang, Measurement and Correlation of Curcumin Solubility in Supercritical Carbon Dioxide, J. Chem. Eng. data 62 (2017) 1257-1263. doi:10.1021/acs.jced.6b00798.

9. D.L. Gurina, M.L. Antipova, E.G. Odintsova, V.E. Petrenko, The study of peculiarities of parabens solvation in methanol- and acetone-modified supercritical carbon dioxide by computer simulation, J. Supercrit. Fluids. 126 (2017) 47–54. doi:10.1016/j.supflu.2017.02.008.

10. Y. Ting, C. Hsieh, Prediction of solid solute solubility in supercritical carbon dioxide with organic cosolvents from the PR + COSMOSAC equation of state, Fluid Phase Equilib. 431 (2017) 48–57. doi:10.1016/j.fluid.2016.10.008.

11. M.P. Ekart, K.L. Bennett, S.M. Ekart, G.S. Gurdial, C.L. Liotta, C.A. Eckert, Cosolvent Interactions in Supercritical Fluid Solutions, ALChE Journal 39 (1993) 235-248.

12. D.L. Tomasko, B.L. Knutson, F. Pouillot, C.L. Liotta, C.A. Eckert, Spectroscopic study of structure and interactions in cosolvent-modified supercritical fluids, J. Phys. Chem. (1993) 11823–11834. doi:10.1021/j100147a041.

13. W. Wu, J. Ke, M. Poliakoff, Phase Boundaries of CO_2 + Toluene , CO_2 + Acetone, and CO_2 + Ethanol at High Temperatures and High Pressures, 2 (2006) 1398–1403. doi:10.1021/je060099a.

14. H. Yang, C. Zhong, Modeling of the solubility of aromatic compounds in supercritical carbon dioxide – cosolvent systems using SAFT equation of state, 33 (2005) 99–106. doi:10.1016/j.supflu.2004.05.008.

15. M. Skerget, L. Christoph, Vapor – liquid equilibrium of binary CO_2 – organic solvent systems, 43 (2008) 383–389. doi:10.1016/j.supflu.2007.07.020.

16. M. Chanda, Introduction to polymer science and chemistry, (pp 148), CRC Press, Florida, 2006.

17. N. Ahn, D.Y. Son, I.H. Jang, S.M. Kang, M. Choi, N.G. Park, Highly Reproducible Perovskite Solar Cells with Average Efficiency of 18.3% and Best Efficiency of 19.7% Fabricated via Lewis Base Adduct of Lead(II) Iodide, J. Am. Chem. Soc. 137 (2015) 8696–8699. doi:10.1021/jacs.5b04930.

18. G. Annohene, G.C. Tepper, Low temperature formation of $CH_3NH_3PbI_3$ perovskite films in supercritical carbon dioxide, J. Supercrit. Fluids. 154 (2019) 104604. doi:10.1016/j.supflu.2019.104604.

19. T. Oku, Crystal Structures of $CH_3NH_3PbI_3$ and related perovskite compounds used for solar cells, Solar Cells - New Approaches and Reviews, (2015) 78-98, http://dx.doi.org/10.5772/59284

20. Q. Chen, H. Zhou, Z. Hong, S. Luo, H. Duan, H. Wang, Y. Liu, G. Li, Y. Yang, Planar Heterojunction Perovskite Solar Cells via Vapor-Assisted Solution Process, J. Am. Chem. Soc (2014) 622–625. doi:10.1021/ja411509g.

21. G. Yang, C. Wang, H. Lei, X. Zheng, P. Qin, L. Xiong, X. Zhao, Y. Yan, G. Fang, Interface engineering in planar perovskite solar cells: energy level alignment, perovskite morphology control and high performance achievement, J. Mater. Chem. A (2017) 1658–1666. doi:10.1039/c6ta08783c.

22. Y. Wang, M. Zhong, L. Chai, Effects of the concentration of PbI_2 and CH_3NH_3I on the perovskite films and the performance of perovskite solar cells based on $ZnO\text{-}TiO_2$ nanorod arrays, Superlattices and Microstructures 123 (2018) 189–200. doi:10.1016/j.spmi.2018.07.024.

23. G. Zheng, C. Zhu, J. Ma, X. Zhang, G. Tang, R. Li, Y. Chen, L. Li, J. Hu, J. Hong, Q. Chen, X. Gao, H. Zhou, Manipulation of facet orientation in hybrid perovskite polycrystalline films by cation cascade, Nat. Commun. (2018) 1–11. doi:10.1038/s41467-018-05076-w.

24. F. Guo, B Zhang, J. Wang, H Bai, R. Guo, Y Huang, P Ren, Facile solvothermal method to synthesize hybrid perovskite $CH_3NH_3PbX_3$ (X = I , Br , Cl) crystals, Optical materials express 7 (2017) 4156–4162.

25. X. Guo, C. Mccleese, C. Kolodziej, A.C.S. Samia, Y. Zhao, C. Burda, Identification and characterization of the intermediate phase in hybrid organic-inorganic $MAPbI_3$ perovskite, Dalton Trans (2016) 3806–3813. doi:10.1039/c5dt04420k.

26. J. Im, I. Jang, N Pellet, M Gratzel, N Park, Growth of $CH_3NH_3PbI_3$ size for high-efficiency perovskite solar cells, Nat. Nanotechnol. 9 (2014) 927–932. doi:10.1038/nnano.2014.181.

27. W. Li, J. Fan, J. Li, Y. Mai, L. Wang, Controllable Grain Morphology of Perovskite Absorber Film by Molecular Self-Assembly toward Efficient Solar Cell Exceeding 17%, J. Am. Chem. Soc (2015) 10399–10405. doi:10.1021/jacs.5b06444.

28. D. Acuna, B. Krishnan, S. Shaji, S. Sepulveda, J.L Menchaca, Growth and properties of lead iodide thin films by spin coating, Bull. Mater. Sci. 9 (2016) 1453-1460. doi 10.1007/s12034-016-1282-z

29. Q. Chen, H. Zhou, T. Song, S. Luo, Z. Hong, H. Duan, L. Dou, Y. Liu, Y. Yang, Controllable Self-Induced Passivation of Hybrid Lead Iodide Perovskites toward High Performance Solar Cells, Nano Lett. 14 (2014) 4158-4163. doi:10.1021/nl501838y.

30. C. Xin, X. Zhou, F. Hou, Y. Du, W. Huang, B. Shi, C. Wei, Y. Ding, G. Wang, G. Hou, Y. Zhao, Y. Li, X. Zhang, Scalable and efficient perovskite solar cells prepared by grooved roller coating, J. Mater. Chem. A (2019), 7 1870–1877. doi:10.1039/c8ta10092f.

CHAPTER 5

DEVICE PERFORMANCE OF $CH_3NH_3PbI_3$ PEROVSKITE SOLAR CELLS PROCESSED IN SUPERCRITICAL CARBON DIOXIDE

5.1 Introduction

Liquid solvent and anti-solvent have been widely used for the crystallization of a wide variety of materials. However, this approach is challenging in thin film crystallization because the surface tension of the liquid leaves a residue upon removal, which severely damages the quality of the film. Therefore, most researchers utilize solvent vapor post-annealing (SVPA) to create the conditions for crystallization of perovskite films. Xiao et al. reported SVPA of Methylammonium Iodide (CH_3NH_3I) and Lead (II) Iodide PbI_2 by the use of DMF solvent vapor at 100℃ achieving PCE of 15.6% [1]. Lui et al. investigated solvent annealing with alcohol vapors at 100℃ using ethanol (13.3% PCE), isopropanol (11.2% PCE), and methanol (14.6% PCE) [2]. Li et al. reported $CH_3NH_3PbI_3-_xCl_x$ perovskite films using Chlorobenzene vapor annealing achieving an average PCE of 13.40% [3]. Luo et al. used γ-butyrolactone (GBL) SVPA at temperatures above 75℃ with a high PCE of 16.58% [4]. However, all of these SVPA approaches are still performed at relatively high annealing temperatures.

As previously reported in Chapters 3 and 4, we showed a novel low-temperature process for the crystallization of perovskite active layers in supercritical carbon dioxide ($scCO_2$) [5] [6]. The key advantage of $scCO_2$ is that it can transition from a high-density liquid-like solvent, where crystallization reactions take place, directly to a dilute gas without crossing a phase boundary and

thus, can be removed without damaging the film. We previously demonstrated that $scCO_2$ was an anti-solvent to the perovskite precursors and did not dissolve the film components. However, it promoted crystal rearrangement into the low-energy perovskite structure by reducing the energy barrier for molecular diffusion [5] [6] [7] [8] [9]. Due to its relatively low critical point (31.2℃, 7.38Mpa or 1070.4psi), no surface tension, liquid-like density, gas-like viscosity and diffusivity, and negligible solubility to the perovskite films, $scCO_2$ is an ideal, scalable, low temperature solvent for post-deposition annealing resulting in high quality perovskite photoactive layers [10].

In this chapter, we report the photovoltaic performance of $CH_3NH_3PbI_3$ perovskite solar cells where the photoactive layer was annealed in $scCO_2$ in comparison to identical solar cells processed using thermal annealing. A PCE of 17.22% was achieved under air mass global (AM 1.5G) spectrum with $scCO_2$ parameters of 1300psi and 50℃. By comparison, thermal annealing without $scCO_2$ yielded a PCE of 9.17% at 50℃.

5.2 Experimental Section

5.2.1 Device fabrication

Devices were prepared on 25mm by 25mm fluorine-doped tin oxide (FTO) glass substrates (Ossila, TEC 15). The substrates were cleaned extensively as follows; ultrasonic bath in 2% Hellmanex solution, rinsing with deionized water, ultrasonic bath in isopropanol for about 15 minutes, ultrasonic bath in acetone for about 15 minutes, rinsing acetone and isopropanol, and finally drying the isopropanol with dry air. The substrates were further plasma cleaned for 15 minutes.

The TiO_2 blocking layer (bl- TiO_2) was formed by spin coating 0.15 M titanium diisopropoxide dis(acetylacetonate) (Sigma-Aldrich, 75 wt% in isopropanol) in 1-butanol

(anhydrous, Sigma-Aldrich, 99.8%) onto the FTO glass substrate at 700 rpm for 8 sec, 1000 rpm for 10 sec and 2000 rpm for 40 sec, followed by drying at 125°C for 5 minutes [11] [12]. The mesoporous TiO_2 (mp-TiO_2) layer was deposited on the bl-TiO_2 by spin-coating a TiO_2 colloidal solution containing 0.6g of TiO_2 paste (30NR-D, Greatcell Solar) diluted in 5 ml of anhydrous ethanol solution at 2000rpm for 20 sec, followed by annealing at 540 °C for 1 hour. The substrate was further treated with 20mM aqueous $TiCl_4$ (> 98%, Sigma-Aldrich) solution at 90°C for 10 minutes, cleaned with deionized water, and then sintered at 500°C for 30 minutes [11] [12].

$CH_3NH_3PbI_3$ was synthesized by mixing a 1:1:1 molar ratio of 2.385g of methylammonium iodide (CH_3NH_3I) (98%, Sigma Aldrich), 6.915g of lead (II) iodide (PbI_2) (99.9985%, Alfa Aesar) and 1.063 mL of dimethyl sulfoxide (DMSO) (≥99.9%, anhydrous, Sigma Aldrich) in 9.484mL of N,N-dimethylformamide (DMF) (≥99.8%, anhydrous, Sigma Aldrich), and 0.3mL of diethyl ether (≥99.8% anhydrous, Sigma Aldrich). The solution was stirred for 1hr at room temperature and filtered with 0.2µm syringe filter (Corning). The solution was processed in an argon-filled glove box. The precursor solution was spin coated onto the substrate at 6000rpm for 25sec. 0.5mL of diethyl ether was dripped onto the rotating surface 6sec into the spinning. For thermally annealed films, the substrate was placed on a hotplate at 50°C and 100°C at 30 minutes respectively. For scCO$_2$ annealed films, the thin film was placed in a pressure vessel (Parr Instrument Pressure Reactor 4768) and a syringe pump (Teledyne ISCO Pump 260D) is used to pressurize the CO_2. After this, the substrate was blown with argon and dried in the glovebox at 50°C for 30 minutes [12] [13] [14].

65 µl of the spiro-MeOTAD solution, which was consisted of 72.3mg spiro-MeOTAD (Sublimed, Ossila), 28.8 µl of 4-tert-butyl pyridine (Ossila) and 17.5µl of lithium bis(trifluoromethanesulfonyl)imide (Li-TFSI) solution (520 mg Li-TSFI (Ossila) in 1ml

acetonitrile (Sigma–Aldrich, 99.8 %) in 1ml of chlorobenzene, was spin-coated on the perovskite

layer at 3000 rpm for 30 sec [15] [16]. Finally, the Ag electrode was deposited using electron beam

evaporation at a constant evaporation rate of 0.03nm/s through a shadow mask resulting in an

electrode thickness of approximately 100 nm. This is shown in Figure 5.1.
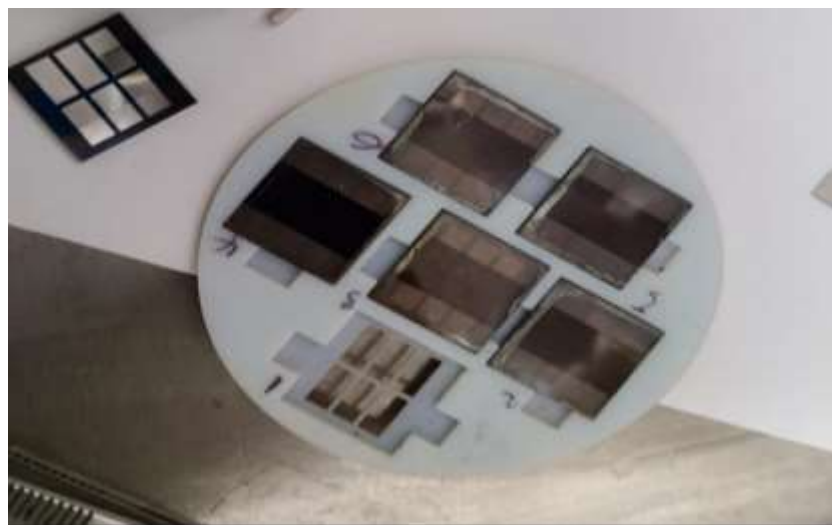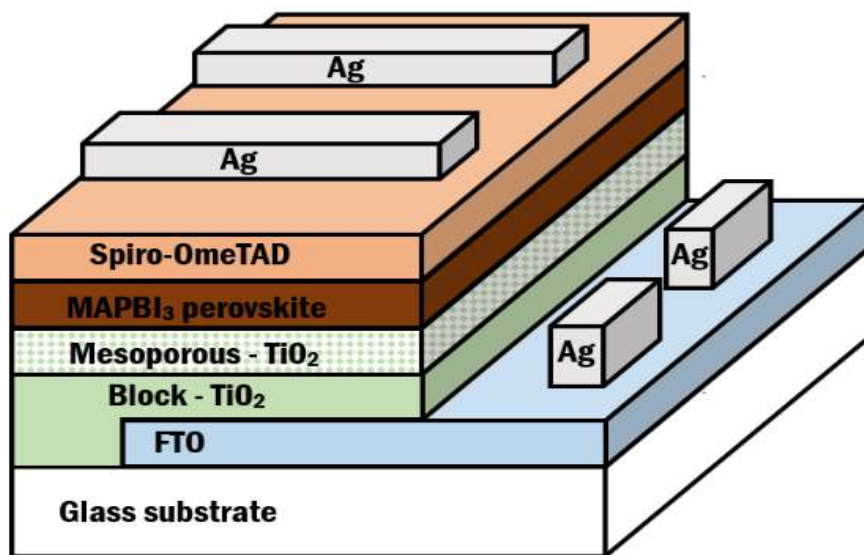
Figure 5.1: Illustration of $CH_3NH_3PbI_3$ perovskite solar cell architecture

5.2.2 Device characterization

Figure 5.2: Setup of Glovebox + Solar I-V System for characterizing $CH_3NH_3PbI_3$ perovskite

solar cells

The crystallographic properties of the perovskite films were characterized by X-ray diffraction (XRD) measurements (PANalytical MPD X'pert Pro), using a Cu Kα (λ =1.54 nm) radiation source that operated at 45 kV and 40 mA. The X-ray diffractograms were obtained at a scan rate of 0.01°/s for 2θ values between 10° and 60°. The surface coverage and grain size were obtained using a scanning electron microscope (SEM) (Hitachi SU-70 FE-SEM) at 20 kV and analyzed using ImageJ software package. Optical spectrometry (transmission, reflection,

absorption) of the films was conducted using a spectral response measurement system (PerkinElmer Lambda 35 UV/VIS Spectrometer). The cross-sectional view of the device was captured using Zeiss Auriga FIB-SEM. The J-V curves were measured by G2V optics small area Pico simulator at room temperature under AM 1.5G illuminations (100 mW/cm^2), and calibrated using a standard silicon solar cell device as shown in Figure 5.2. An aperture mask of 0.09cm^2 was used to define the device area as shown in Figure 5.3.
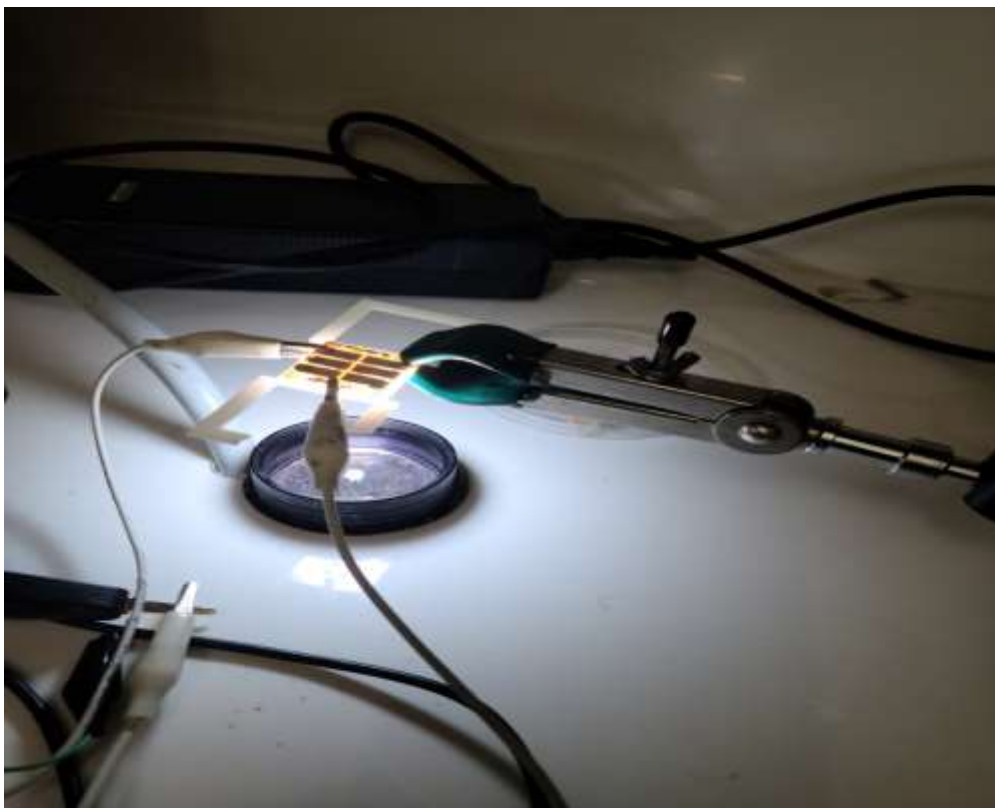
Figure 5.3: Illustration of Illumination of the perovskite solar cells in the glove box

5.3. Materials Characterization

Figure 5.4 shows SEM images of the top surfaces of perovskite films produced with thermal and with $scCO_2$ annealing. A hundred grains were used to calculate the average grain size

from several SEM images. The film thermally annealed at 50°C exhibited poor quality with observable pinholes and average grain size of 527.9 ± 167.7nm. Increasing the annealing temperature to 100°C eliminates the pinholes and increases the average grain size to 613.1 ± 212.8nm. The SEM image of the surface processed in $scCO_2$ at 50°C showed a smooth and pinhole-free with an average grain size of 632.3 ± 188.0nm. With $scCO_2$ annealing at 100°C, there was an improvement of the quality significantly as compared to thermal annealing at 100°C with an average grain size of 666.8 ± 257.6nm.
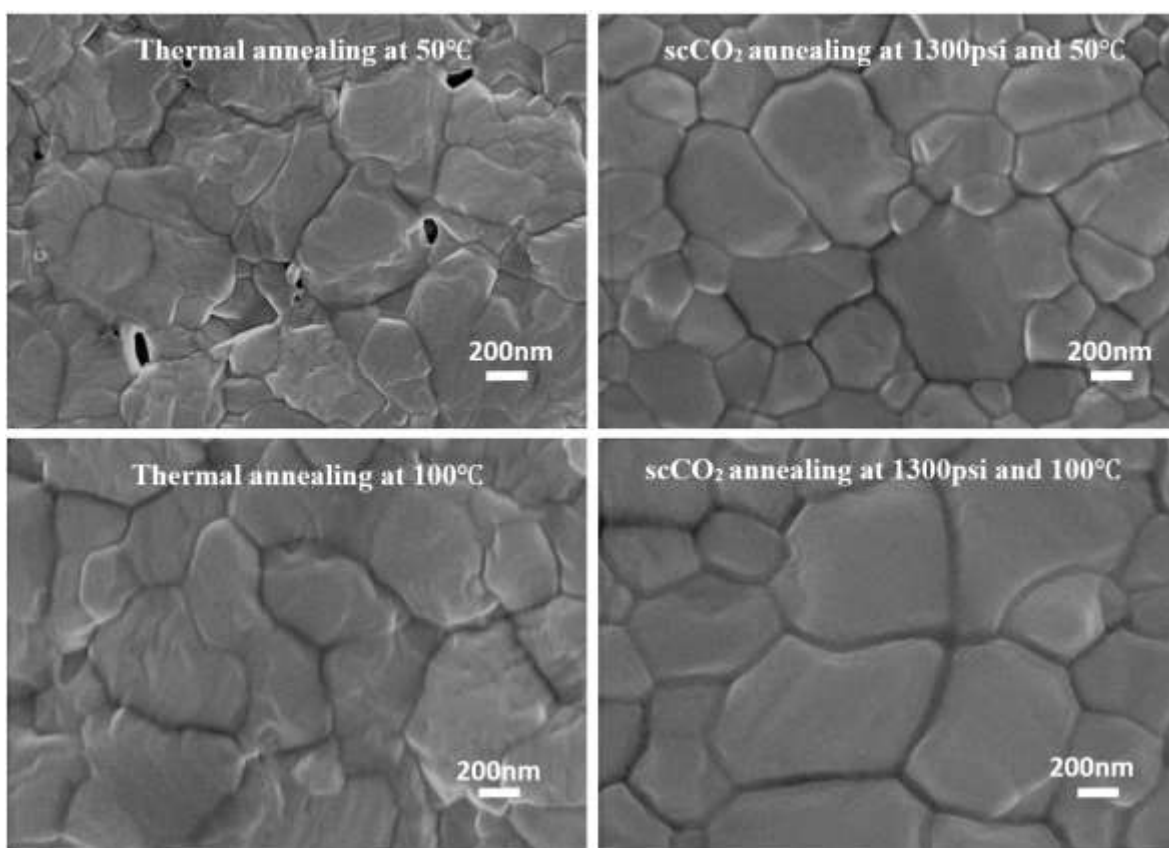
Figure 5.4: SEM images of the perovskite thin film at different annealing conditions for 30 minutes

.
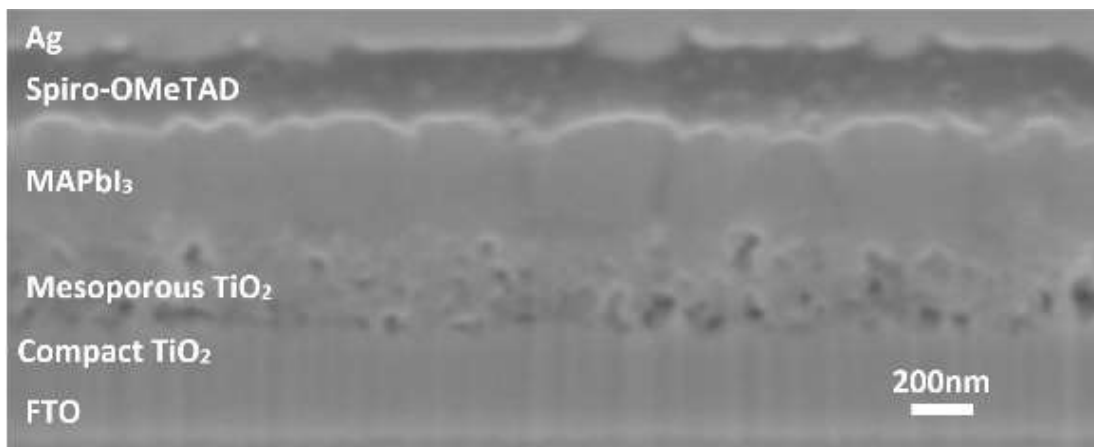
Figure 5.5: FIB-assisted cross-sectional SEM image of perovskite solar cell device processed

using $scCO_2$ at 50°C

The perovskite layers annealed with and without $scCO_2$ were incorporated into photovoltaic devices consisting of an FTO/bl-TiO$_2$/mp-TiO$_2$/CH$_3$NH$_3$PbI$_3$/spiro-MeOTAD/Ag configuration. Figure 5.5 is a FIB-assisted SEM cross-sectional image of a typical device produced in our laboratory. $CH_3NH_3PbI_3$ film was annealed at 50°C in $scCO_2$ and has a thickness of about 450nm. The blocking TiO$_2$ (bl-TiO$_2$) layer, mesoporous TiO$_2$ (mp-TiO$_2$), and spiro-MeOTAD layer are about 40nm, 300nm, and 200nm, respectively.

Figure 5.6 - A shows the optical absorption spectra for the four perovskite films processed under the conditions shown in Figure 5.4. The overall shape of the absorption spectra for all four was consistent with the standard perovskite absorption spectra [17] [18]. From the spectra, it can be seen that the perovskite film annealed at 50°C with $scCO_2$ exhibited an optical absorption spectra slightly better than the film processed 50°C by thermal annealing, presumably due to the larger grain size and improved film quality as shown in Figure 5.4. Films annealed at 100°C with

$scCO_2$ exhibited similar absorbance to those processed in $scCO_2$ at 50°C, and those annealed at 100°C without $scCO_2$.
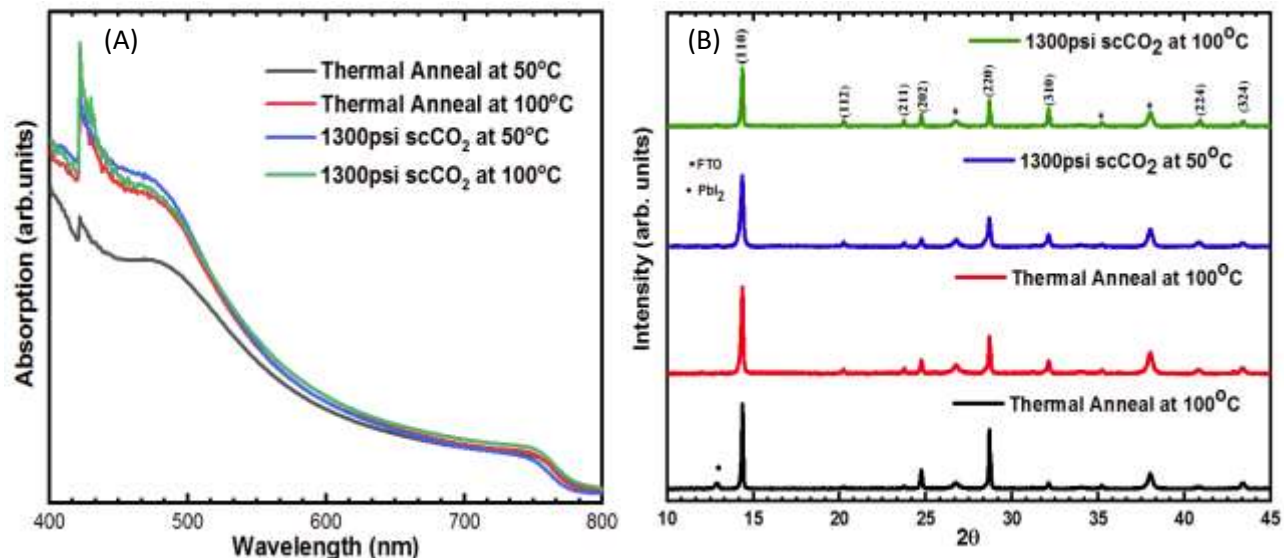
Figure 5.6: (A) Optical absorption spectra of the thin film at thermal annealing and $scCO_2$ annealing condition, (B) XRD patterns of the perovskite thin films [12]

Figure 5.6 - B shows XRD patterns of four perovskite films processed under the conditions of Figure 5.4. The XRD pattern of the film annealed at 50°C but without $scCO_2$ had a (100) peak consistent with PbI_2 impurities and incomplete crystallization [19]. The XRD spectra of the film annealed at 100°C without $scCO_2$ and the films processed $scCO_2$ at 50 °C and 100 °C showed complete crystallization with no visible PbI_2 peak. The diffraction peaks at 14.1°, 24.8°, 28.7°, and 32.2°, corresponding to the (110), (202), (220), and (310) planes of crystalline $CH_3NH_3PbI_3$, respectively with a tetragonal crystal structure were present [4] [20] [21].

5.4 Electrical Characterization
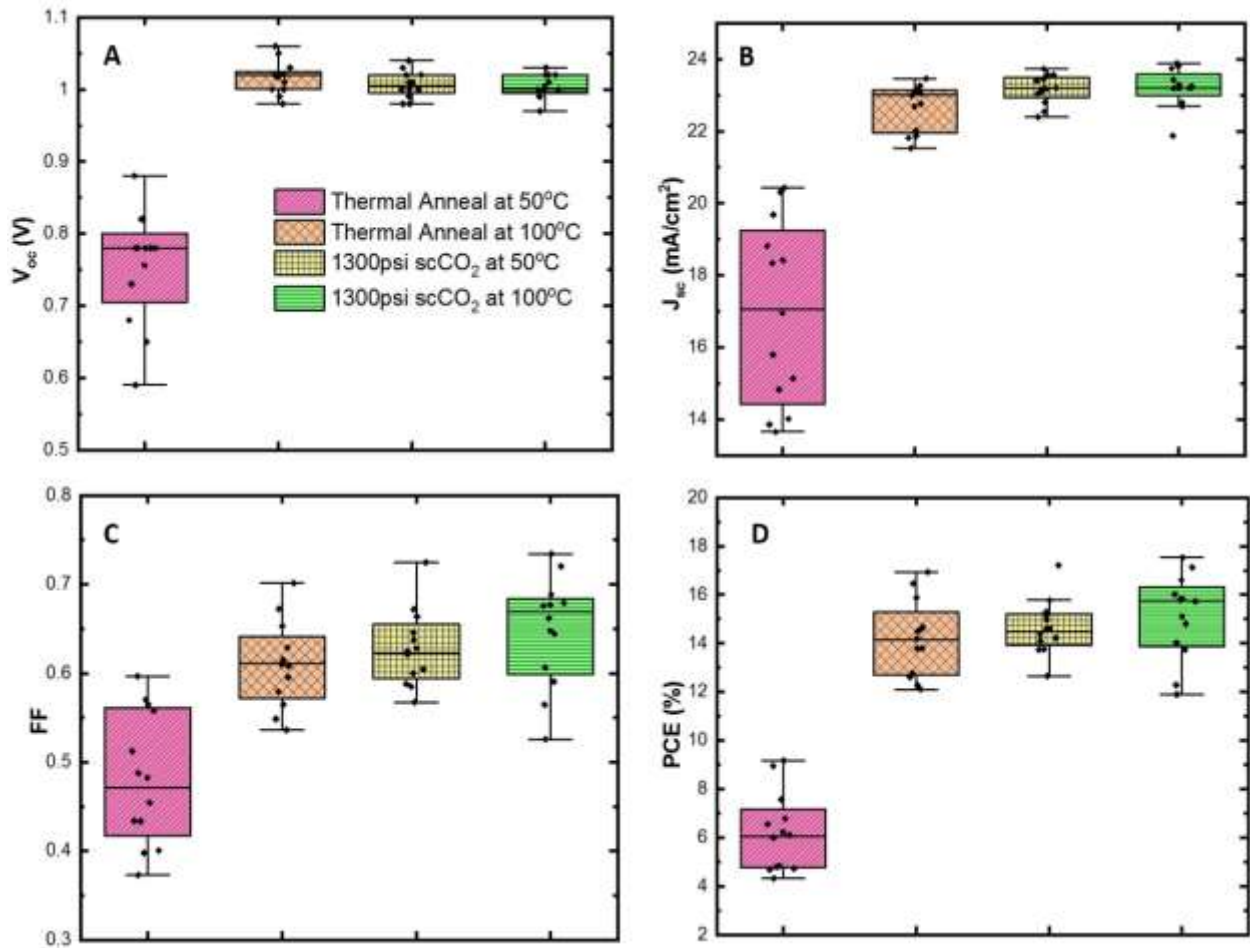
Figure 5.7: Box plot measuring (A) Open-circuit voltage (V_{oc}) (B) Short-circuit current density (J_{sc}) (C) Fill factor (FF) and (D) Power conversion efficiency [12]

Figure 5.7 is a plot of the open-circuit voltage, short-circuit current density, fill factor, and power conversion efficiency for 48 photovoltaic devices (12 for each perovskite annealing condition) produced under the conditions of Figure 5.4. Comparing the low temperature devices (thermal annealed at 50°C and films annealed at 50°C in $scCO_2$ at 1300Psi), the latter exhibited far superior photovoltaic parameters with a smaller standard deviation. The devices annealed at 50°C

in $scCO_2$ resulted in an average short-circuit photocurrent density (Jsc) of 23.17 ± 0.42 mA/cm^2,

open-circuit voltage (V_{oc}) of 1.00 ± 0.02 V, fill factor (FF) of 0.6278 ± 0.0442, and PCE of 14.65

$\pm$ 1.16%. On the other hand, devices annealed at 50°C but without $scCO_2$ resulted in poor

photovoltaic performance with Jsc of 16.94 ± 2.64 mA/cm^2, V_{oc} of 0.76 ± 0.08 V, FF of $0.4818 \pm$

0.0772, and PCE of $6.205 \pm 1.67\%$. The use of $scCO_2$ to assist in perovskite crystallization at low

temperature resulted in superior film quality and photovoltaic performance. Devices thermal

annealed at 100°C without $scCO_2$ yielded an average PCE of $14.198 \pm 1.62\%$ and devices annealed

at 100°C with $scCO_2$ resulted in an average PCE of $15.11 \pm 1.81\%$. Therefore, the benefit of using

$scCO_2$ at the higher annealing temperatures was not as dramatic.
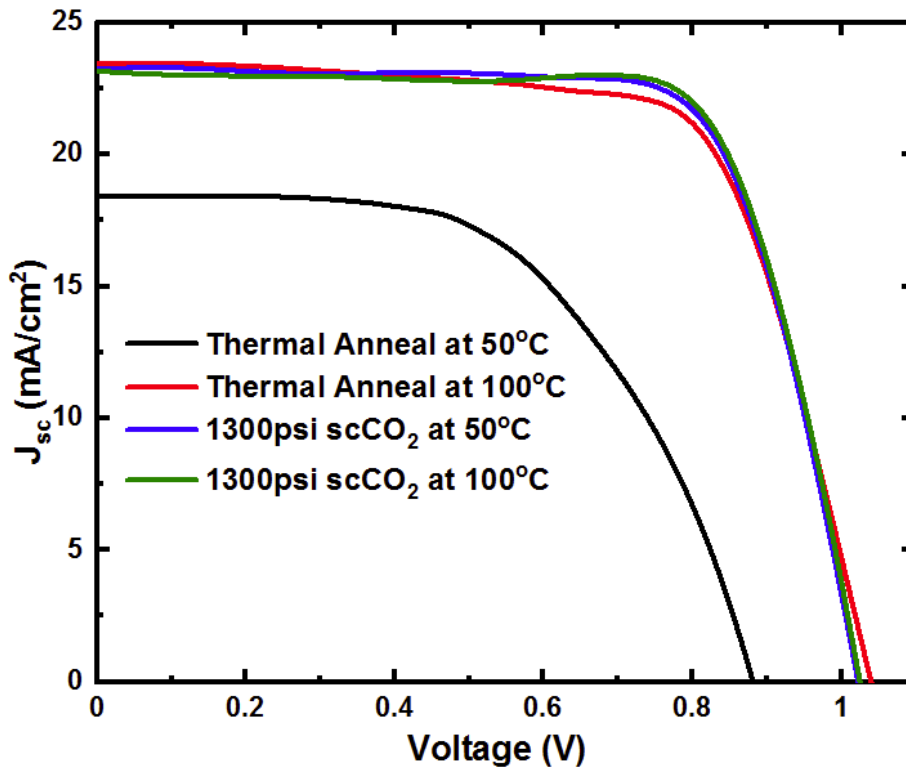
Figure 5.8: Plot of current density-voltage (J-V) curves of devices with perovskite layers

thermally annealed at 50 °C and 100°C with and without $scCO_2$ [12]

Figure 5.8 is a plot of current density versus voltage for the highest performing devices obtained at each of the four perovskite annealing conditions. For the devices annealed at low temperature, the highest PCE of 17.22% was achieved with Jsc of 23.20 mA/cm^2, V_{oc} of 1.02 V, and FF of 0.7245 with the perovskite layer annealed at 50°C scCO$_2$. For devices annealed at 50°C without scCO$_2$, the highest PCE obtained was 9.17% from Jsc of 18.41 mA/cm^2, V_{oc} of 0.88 V, and FF of 0.5646. Therefore, at lower temperatures, the use of scCO$_2$ resulted in higher quality films (Figure 5.4) with superior optical absorption (Figure 5.6 - A) and better photovoltaic performance (Figure 5.9) in comparison to thermal annealing alone. The device with the highest overall performance was obtained by annealing the perovskite layer at 100°C in scCO$_2$ which yielded a PCE of 17.52% with Jsc of 23.20 mA/cm^2, V_{oc} of 1.03 V, and FF of 0.7242. For the devices where the perovskite layer was annealed at 100°C without scCO$_2$, the highest obtained PCE was 16.94%. The superior performance of devices can be attributed to the greater smoothness, larger grain size, and better crystallinity [1] [22].
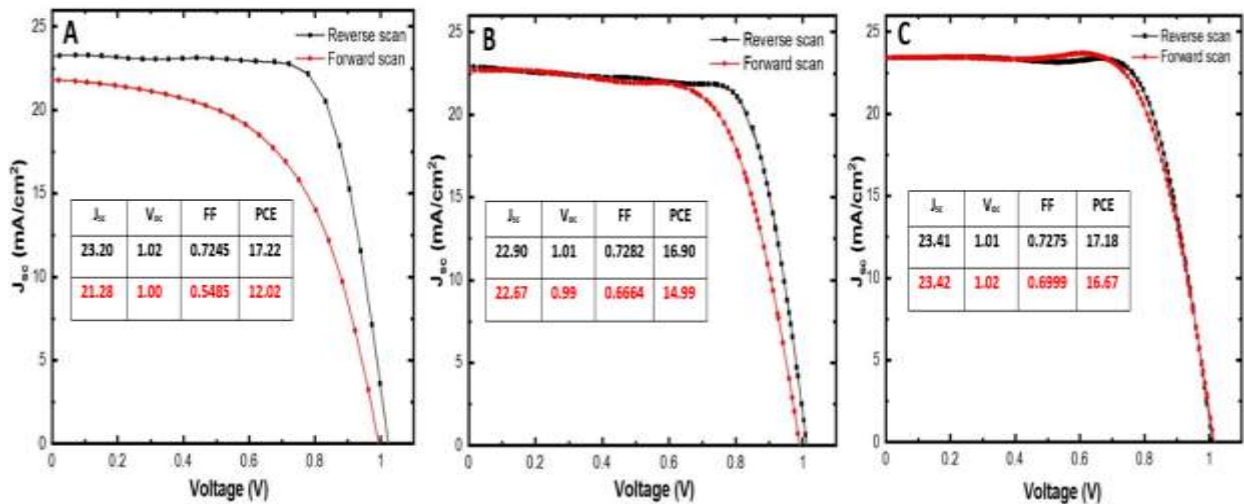
Figure 5.9: J-V curve hysteresis measured at three different scan rates, (A) 40mV/s (B) 10mV/s (C) 6mV/s. Measurement from V_{oc} to J_{sc} is referred to reverse scan (black) and vice versa is for forward scan (red) [12]

Figure 5.9 A-C shows the J−V hysteresis from a device where the perovskite layer was annealed at 50°C in scCO$_2$. The amount of hysteresis decreases with decreasing scan rate and very little hysteresis was observed at a scan rate of 6mV/s, where PCE = 17.18% at a reverse scan and 16.67% at a forward scan (3% difference).

References

1. Z. Xiao, Q. Dong, C. Bi, Y. Shao, Y. Yuan, Solvent Annealing of Perovskite-Induced Crystal Growth for Photovoltaic-Device Efficiency Enhancement, (2014) 6503–6509. doi:10.1002/adma.201401685.

2. C. Liu, K. Wang, C. Yi, X. Shi, A.W. Smith, X. Gong, A.J. Heeger, Efficient Perovskite Hybrid Photovoltaics via Alcohol-Vapor Annealing Treatment, (2016) 101–110. doi:10.1002/adfm.201504041.

3. B. Li, T. Jiu, C. Kuang, S. Ma, Q. Chen, X. Li, J. Fang, Chlorobenzene vapor assistant annealing method for fabricating high quality perovskite films, Org. Electron. 34 (2016) 97–103. doi:10.1016/j.orgel.2016.04.024.

4. J. Luo, Z. Qiu, S. Yang, X. Wang, RSC Advances Mechanism and effect of g - butyrolactone solvent vapor post-annealing on the performance of a mesoporous perovskite solar cell, (2018) 724–731. doi:10.1039/c7ra10695e.

5. G. Annohene, G.C. Tepper, Low temperature formation of $CH_3NH_3PbI_3$ perovskite films in supercritical carbon dioxide, J. Supercrit. Fluids. 154 (2019) 104604. doi:10.1016/j.supflu.2019.104604.

6. G. Annohene, J. Pascucci, D. Pestov, G.C. Tepper, Supercritical fluid-assisted crystallization of $CH_3NH_3PbI_3$ perovskite films, J. Supercrit. Fluids. 156 (2020) 104684. doi:10.1016/j.supflu.2019.104684.

7. S.S. Dinachali, W. Bai, K. Tu, H.K. Choi, J. Zhang, M.E. Kreider, L. Cheng, C.A. Ross, Thermo-Solvent Annealing of Polystyrene-Polydimethylsiloxane Block Copolymer Thin Films ,4 (2015) 500. doi:10.1021/acsmacrolett.5b00108.

8. T.P. Lodge, M.C. Dalvi, Mechanism of chain diffusion in lamellar block copolymers, R. Letters, f f, 75 (1995) 657–660.

9. K.W. Gotrik, C.A. Ross, Solvothermal Annealing of Block Copolymer Thin Films, Nano Lett., 13 (2013) 5117-5122. doi:10.1021/nl4021683.

10. D. Sanli, S.E. Bozbag, C. Erkey, Synthesis of nanostructured materials using supercritical CO2: Part I. Physical transformations, J. Mater. Sci. 47 (2012) 2995–3025. doi:10.1007/s10853-011-6054-y.

11. N. Ahn, D.Y. Son, I.H. Jang, S.M. Kang, M. Choi, N.G. Park, Highly Reproducible Perovskite Solar Cells with Average Efficiency of 18.3% and Best Efficiency of 19.7% Fabricated via Lewis Base Adduct of Lead(II) Iodide, J. Am. Chem. Soc. 137 (2015) 8696–8699. doi:10.1021/jacs.5b04930.

12. G. Annohene, G.C. Tepper, Efficient perovskite solar cells processed in supercritical carbon dioxide, J. Supercrit. Fluids. 171 (2021) 105203. doi.org/10.1016/j.supflu.2021.105203

13. G. Annohene, G.C. Tepper, The Journal of Supercritical Fluids Low temperature formation of $CH_3NH_3PbI_3$ perovskite films in supercritical carbon dioxide, J. Supercrit. Fluids. 154 (2019) 104604. doi:10.1016/j.supflu.2019.104604.

14. G. Annohene, J. Pascucci, D. Pestov, G.C. Tepper, The Journal of Supercritical Fluids Supercritical fluid-assisted crystallization of $CH_3NH_3PbI_3$ perovskite films, J. Supercrit. Fluids. 156 (2020) 104684. doi:10.1016/j.supflu.2019.104684.

15. J. Burschka, N. Pellet, S. Moon, R. Humphry-Baker, M.K. Nazeeruddin, M. Gratzel, Sequential deposition as a route to high-performance perovskite-sensitized solar cells, Nature, 499 (2013) 316–319. doi:10.1038/nature12340.

16. J-H. Im, I-H. Jang, N. Pellet, M. Gratzel, N-G. Park, Growth of $CH_3NH_3PbI_3$ cubiods with controlled size for high-efficiency perovskite solar cells, Nat. Nanotechnol. 9 (2014) 927–932. doi:10.1038/nnano.2014.181.

17. Y. Zhou, M. Yang, A.L. Vasiliev, H.F. Garces, Y. Zhao, D. Wang, S. Pang, K. Zhu, N.P. Padture, Growth control of compact $CH_3NH_3PbI_3$ thin films via enhanced solid-state precursor reaction for efficient planar perovskite solar cells, J. Mater. Chem. A. 3 (2015) 9249–9256. doi:10.1039/c4ta07036d.

18. Y. Wang, T. Zhang, F. Xu, Y. Li, Y. Zhao, A Facile Low Temperature Fabrication of High Performance CsPbI2Br All-Inorganic Perovskite Solar Cells , Sol. RRL. 2 (2018) 1700180. doi:10.1002/solr.201700180.

19. D. Shen, X. Yu, X. Cai, M. Peng, Y. Ma, X. Su, L. Xiao, D. Zou, Understanding the solvent-assisted crystallization mechanism inherent in efficient organic-inorganic halide perovskite solar cells, J. Mater. Chem. A. 2 (2014) 20454–20461. doi:10.1039/c4ta05635c.

20. Q. Chen, H. Zhou, Z. Hong, S. Luo, H. Duan, H. Wang, Y. Liu, G. Li, Y. Yang, Planar

Heterojunction Perovskite Solar Cells via Vapor-Assisted Solution Process, (2014) 3–6. doi:10.1021/ja411509g.

21. G. Yang, C. Wang, H. Lei, X. Zheng, P. Qin, L. Xiong, X. Zhao, Y. Yan, G. Fang, Interface engineering in planar perovskite solar cells: energy level alignment, perovskite morphology control and high performance achievement, 5 (2017) 1658–1666. doi:10.1039/c6ta08783c.

22. W. Ke, C. Xiao, C. Wang, B. Saparov, H. Duan, D. Zhao, Z. Xiao, P. Schulz, S.P Harvey, W. Liao, W. Meng, Y. Yu, A.J. Cimaroli, C. Jiang, K. Zhu, M. Al-Jassim, G. Fang, D.B. Mitzi, Y. Yan, Employing Lead Thiocyanate Additive to Reduce the Hysteresis and Boost the Fill Factor of Planar Perovskite Solar Cells, 28 (2016) 5214-5221

CHAPTER 6

MOISTURE STABILITY OF PEROVSKITE SOLAR CELLS PROCESSED IN SUPERCRITICAL CARBON DIOXIDE

6.1 Introduction

Although the performance of PSCs is outstanding, its major challenge to commercialization remains the stability of the crystals [1] [2]. Poor stability of PSCs are typically due to degradation of the perovskite crystals from exposure to atmospheric oxygen and humidity [3] [4] [5] [6], sensitivity to temperature [7], illumination [8] [9], ion migration [10] [11] and other minor ones such as electric field led decomposition, and interface reaction. With all these, degradation by humidity remains the main factor influencing the poor crystal stability of the perovskite materials. Thus, varied approaches have been adopted to stabilize halide perovskites, including compositional tuning [12] [13] [14], low dimensional perovskites [15] [16], additive assisted treatment [17] [18], use of perovskite surface blocking layers [9] [20], enhancing the grain sizes of the perovskites and others.

For the hybrid organic-inorganic perovskites, instability is from the organic component, where the $CH_3NH_3PbI_3$ decomposes into a lead iodide (PbI_2) and methylammonium iodide (CH_3NH_3I). CH_3NH_3I gives up a proton to water, forming H_3O^+ by breaking the bond between the A and B site of the ABX_3 perovskite structure [21] [22] [23]. Frost el at. (2014) explained a possible water-facilitated decomposition path through equations 1 to 5 [24]. Conclusions could be drawn from the equations that exposure of the perovskite to moisture results in the organic iodide forming HI acid, which dissolves in water. Trace amounts of water are adequate to deprotonate the

organic component to cause degradation. In addition, the exposure of the film to trace amounts of H_2O results in partial decomposition until the byproducts reach equilibrium.

$$CH_3NH_3PbI_3(s) \leftrightarrow CH_3NH_3I(aq) + PbI_2(s) \quad (1)$$

$$CH_3NH_3I(aq) \leftrightarrow CH_3NH_2(aq) + HI(aq) \quad (2)$$

$$4HI(aq) + O_2 \leftrightarrow 2I_2(s) + 2H_2O \quad (3)$$

$$2HI(aq) \leftrightarrow H_2\uparrow + I_2\ (s) \quad (4)$$
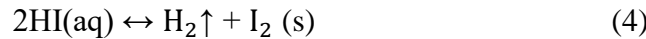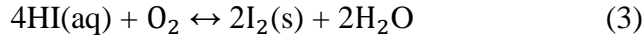
From our initial studies, we demonstrated that $scCO_2$ annealing of $CH_3NH_3PbI_3$ perovskite thin films results in high quality thin films leading to high photovoltaic efficiencies. In this chapter, we extend our studies to see the humidity degradation rate and its effect on $scCO_2$ annealed films. Understanding this will lead to a more robust development and design of how to bolster the stability using supercritical fluids. We systematically show the effect of relative humidity (RH) in a dry desiccator ($> 5\%$ RH), at 40% RH and 60% RH on film absorption, crystallinity, and PCE.

6.2 Experimental Section

6.2.1 Device fabrication

All experimental procedures are similar to our previous report [32]. Fluorine-doped tin oxide (FTO) glass substrates (Ossila, TEC 15) of size 25mm by 25mm were used. The cleaning procedure of the substrate is described as follows; ultrasonic bath in 2% Hellmanex solution, rinsing with deionized water, ultrasonic bath in isopropanol for about 15 minutes, ultrasonic bath in acetone for about 15 minutes, rinsing acetone and isopropanol, drying the isopropanol with dry air and further plasma cleaned for 15 minutes.

The Titanium dioxide (TiO_2) blocking layer (bl-TiO_2) was formed by spin coating 0.15 M titanium diisopropoxide dis(acetylacetonate) (Sigma-Aldrich, 75wt% in isopropanol) in 1-butanol (anhydrous, Sigma-Aldrich, 99.8%) onto the FTO glass substrate at 700 rpm for 8 sec, 1000 rpm for 10 sec and 2000 rpm for 40 sec, followed by drying at 125℃ for 5 minutes [25] [26]. The mesoporous TiO_2 (mp- TiO_2) layer was deposited on the bl- TiO_2 by spin-coating a TiO_2 colloidal solution containing 0.6g of TiO_2 paste (30NR-D, Greatcell Solar) diluted in 5 ml of anhydrous ethanol solution at 2000 rpm for 20 sec, followed by annealing at 540 °C for 1 hour. The substrate was further treated with 20 mM aqueous TiCl4 (> 98%, Sigma-Aldrich) solution at 90℃ for 10 min, cleaned with deionized water and then sintered at 500℃ for 30 minutes [25] [26].

$CH_3NH_3PbI_3$ was synthesized by mixing a 1:1:1 molar ratio of 2.385g of methylammonium iodide (CH_3NH_3I) (98%, Sigma Aldrich), 6.915g of lead (II) iodide (PbI_2) (99.9985%, Alfa Aesar) and 1.063 mL of dimethyl sulfoxide (DMSO) (≥99.9%, anhydrous, Sigma Aldrich) in 9.484mL of N,N-dimethylformamide (DMF) (≥99.8%, anhydrous, Sigma Aldrich) and 0.3mL of diethyl ether (≥99.8% anhydrous, Sigma Aldrich). The solution was stirred for 1 hour at room temperature and filtered with a 0.2µm syringe filter (Corning). The solution was processed in an argon-filled glove box. The precursor solution was spin coated onto the substrate at 6000rpm for 25sec. 0.5mL of diethyl ether was dripped onto the rotating surface 6sec into the spinning. For thermally annealed films, the substrate was placed on a hotplate at 50℃ and 100℃ at 30 minutes respectively. For scCO$_2$ annealed films, the thin film was placed in a pressure vessel (Parr Instrument Pressure Reactor 4768) and a syringe pump (Teledyne ISCO Pump 260D) is used to pressurize the carbon dioxide at 1300psi. After this, the substrate was blown with argon and dried in the glovebox at 50℃ for 30 minutes [25] [27] [28].

65 µl of the spiro-MeOTAD solution, which contained 72.3mg spiro-MeOTAD (Sublimed, Ossila), 28.8 µl of 4-tert-butyl pyridine (Ossila) and 17.5 µl of lithium bis(trifluoromethanesulfonyl)imide (Li-TFSI) solution (520 mg Li-TSFI (Ossila) in 1 ml acetonitrile (Sigma–Aldrich, 99.8 %) in 1ml of chlorobenzene, was spin-coated on the perovskite layer at 3000 rpm for 30 sec [29] [30]. Finally, the Silver (Ag) electrode was deposited using electron beam evaporation at a constant evaporation rate of 0.03 nm/s through a shadow mask resulting in an electrode thickness of approximately 100 nm. A homemade device was used to expose the samples to higher relative humidity (40% and 60%). For lower relative humidity ($<$ 5% RH), samples were stored in a dry desiccator kept in argon filled glovebox.

6.2.2 Device characterization

The crystallographic properties of the perovskite films were characterized by X-ray diffraction (XRD) measurements (PANalytical MPD X'pert Pro), using a Cu Kα (λ =1.54 nm) radiation source that operated at 45kV and 40mA. The X-ray diffractograms were obtained at a scan rate of 0.01°/s for 2θ values between 10° and 60°. The surface coverage and grain size were obtained using a scanning electron microscope (SEM) (Hitachi SU-70 FE-SEM) at 20 kV and analyzed using the ImageJ software package. Optical spectrometry (transmission, reflection, absorption) of the films was conducted using a spectral response measurement system (PerkinElmer Lambda 35 UV/VIS Spectrometer). The J-V curves were measured by G2V optics small area Pico simulator at room temperature under AM 1.5G illuminations (100 mW/cm^2), and calibrated using a standard silicon solar cell device. An aperture mask of 0.09cm^2 was used to define the device area.

6.3 Effects of Relative Humidity $CH_3NH_3PbI_3$ perovskite thin films
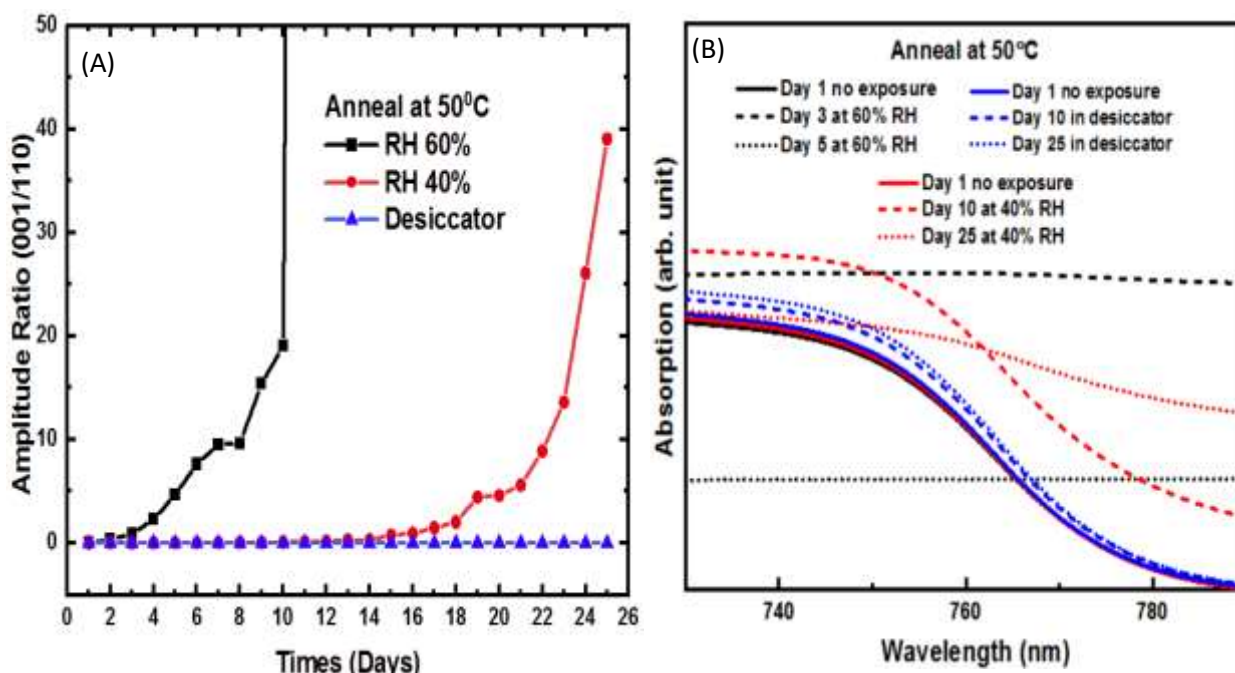
Figure 6.1: A: Amplitude ratio of relative intensity of the (001) and (110) planes of $CH_3NH_3PbI_3$ of films thermally annealed at 50℃ B: Optical absorption spectra of the film at different humidity parameters corresponding to A

In our previous studies, we have shown the effect of $scCO_2$ annealing with parameters such as time, temperature, pressure, and additions of varied cosolvents on the crystallinity of the perovskite [25] [27] [28]. For all $scCO_2$ annealing (with no cosolvent), the diffraction peaks at 14.1°, 24.8°, 28.7°, and 32.2°, corresponds to the (110), (202), (220), and (310) planes of crystalline $CH_3NH_3PbI_3$ respectively, with a tetragonal crystal structure, were found [25] [26] [27] [28]. The XRD for PbI_2 shows that in general, thin film growth is oriented along (001) direction at 12.73° irrespective of the spin parameters. This is typically due to the use of DMF, a less soluble,

polar solvent containing electronegative oxygen atoms [35]. PbI_2 presence typically shows incomplete crystallization and/or degradation [36]. The effect of relative humidity on the $CH_3NH_3PbI_3$ crystallinity was studied using XRD and UV-VIS.

Figure 6.1 – A shows the ratio of the relative intensities of the dominant peak of PbI_2 (001) and that of $CH_3NH_3PbI_3$ (110) after thermal annealing at 50°C. From this, there was a negligible degradation rate when samples were kept in the desiccator for 25 days due to fewer moisture interactions with the perovskite film. However, when the samples were exposed to a relative humidity of 40%, there was an exponential decay, which takes off on about day 15. This conforms to other degradation works described earlier on how unencapsulated films degrade with time. Exposing the thin films to 60% RH also shows rapid exponential degradation on the first day of exposure. Therefore, we see a strong correlation between an increase in relative humidity with degradation of the perovskite film.
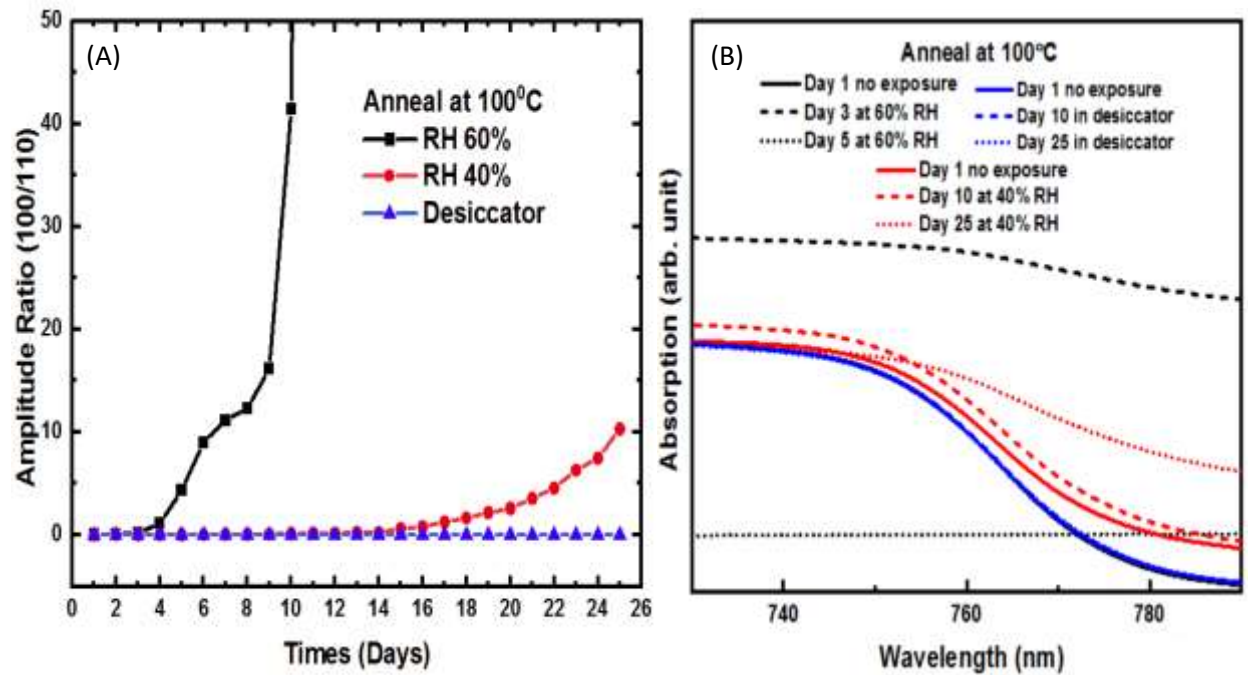
Figure 6.2: A: Amplitude ratio of the relative intensity of the (001) and (110) planes of

$CH_3NH_3PbI_3$ of films thermally annealed at 100°C B: Optical absorption spectra of the film at

different humidity parameters corresponding to A

Figure 6.1 – B shows the optical absorption spectra of the perovskite film around the band

gap after annealing at 50°C and exposing it to varied relative humidity parameters. The absorption

spectra after keeping the samples in a dry desiccator showed the pattern for perovskite formation

around the band gap but a little broadening from day 10 to day 25. This corresponds to the relative

flat change shown in the XRD pattern. As the humidity is boosted to 40% RH, the spectrum

broadens widely with an increase in days, showing less absorption. For 60% RH, the spectrum

flattens drastically with an increase in humidity accounting for an exponential degradation, which

leads to a more transparent film. On day 5, we see no absorption spectra response of films exposed

to the relative humidity of 60%.

Figure 6.2 – A shows the ratio of the relative intensities of the dominant peak of PbI_2 (001)

and that of $CH_3NH_3PbI_3$ (110) after thermal annealing at 100°C. With this also, there is a negligible

degradation rate when samples are kept in the desiccator for 25 days. When the samples are

exposed to a relative humidity of 40%, there was no crystal degradation up until the 15, where it

gradually degrades. The better degradation mechanism of thermally annealed films at 100°C

compared to those at 50°C is due to high quality film morphology. Exposing the thin film to 60%

RH also showed exponential degradation.

In Figure 6.2 – B, the optical absorption spectra of the perovskite film around the band gap

after annealing at 100°C and exposing it to varied relative humidity parameters are shown. The

absorption spectra after keeping the samples in a dry desiccator are unchanged after 25 days. As the humidity is boosted to 40% RH, absorption flattened compared to those made on the first day before exposure. For 60% RH, the spectrum flattened drastically with an increase in humidity accounting for an exponential degradation, which led to a more transparent film. The traditional annealing at 100°C did not offer any benefit against the exponential degradation at 60% RH but showed less degradation at 40% RH compared to films annealed at 50°C.
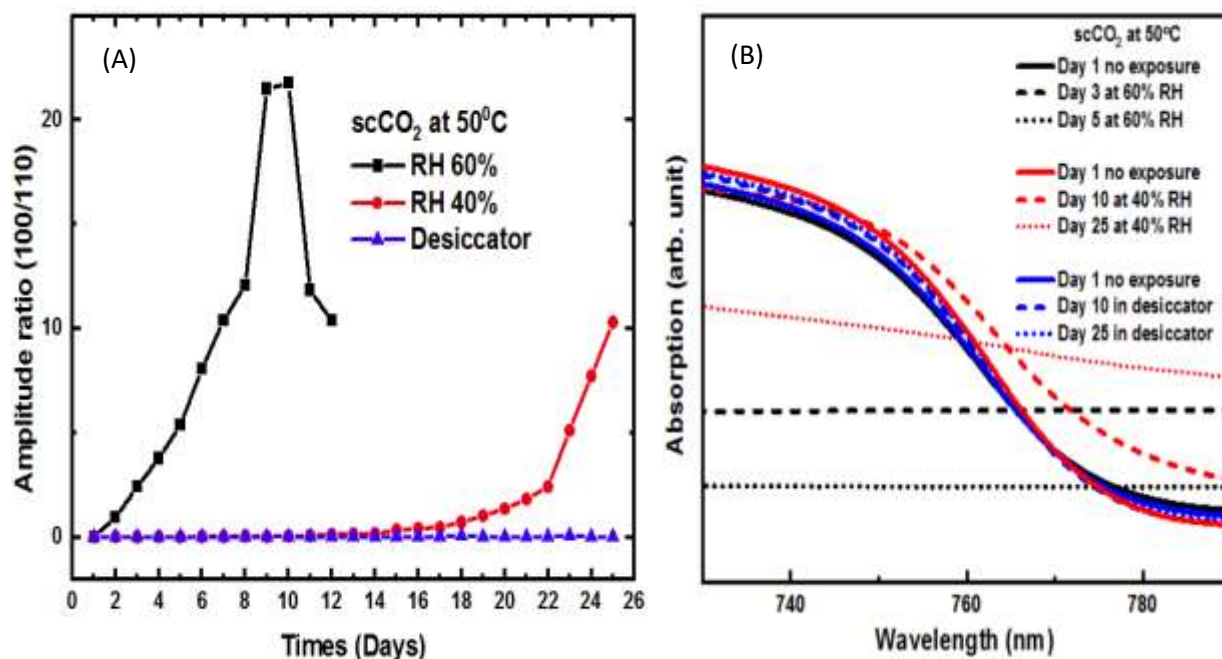
Figure 6.3: A: Amplitude ratio of the relative intensity of the (001) and (110) planes of $CH_3NH_3PbI_3$ of films after $scCO_2$ annealing at 50°C B: Optical absorption spectra of the film at different humidity parameters corresponding to A

In Figure 6.3 – A, there is a negligible degradation rate when samples are kept in the desiccator for 25 days as well after $scCO_2$ annealing at 50°C. Samples exposed to a relative

humidity of 40% had no degradation until the 15th day when it rose slowly. Exposing the thin films to 60% RH also showed rapid exponential degradation on the first day of exposure. Figure 2.3 – B shows the optical absorption spectra of the perovskite film around the band gap after $scCO_2$ annealing at 50°C and exposing it to varied relative humidity parameters. The absorption spectra after keeping the samples in a dry desiccator were similar through to the 25th day. As the humidity was raised to 40% RH, the absorption vastly reduces on day 25. For 60% RH, the film's absorption decreases drastically with no visible band gap.

6.4 Effects of Relative Humidity $CH_3NH_3PbI_3$ perovskite device performance
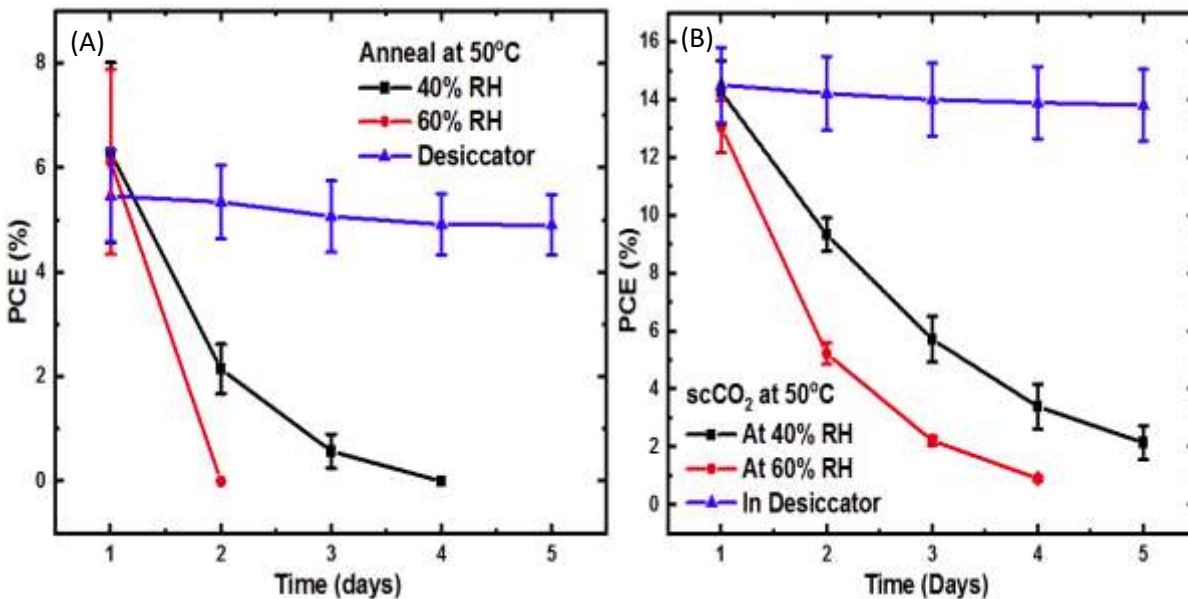
Figure 6.4: PCE degradation rate of perovskite films after annealing with (A) thermal at 50°C (B) $scCO_2$ at 50°C

Figure 6.4 (A and B) compares the power conversion efficiency degradation rate of films thermally annealed and with $scCO_2$ at a lower temperature of 50°C, after exposure to different

relative humidity parameters. On day one, which was a point of no exposure to any form of relative humidity, the average PCE of films annealed with $scCO_2$ was about twice as that of thermally annealed films. To be precise, devices as-fabricated after thermal annealing at 50°C without any humidity exposure had an average PCE of 6.29 ± 1.72%, 6.12 ± 1.77%, and 5.46 ± 0.87% and were used for degradation rate experiment for 40% RH, 60% RH and samples stored in dry desiccator respectively. However, at the same temperature but using $scCO_2$ for post-deposition annealing, the average PCE jumped to 14.27 ± 1.09%, 13.07 ± 0.90%, and 14.52 ± 1.32% respectively. This shows that $scCO_2$ annealed films have better photovoltaic performance at lower temperatures than thermally annealed films due to superior film quality.
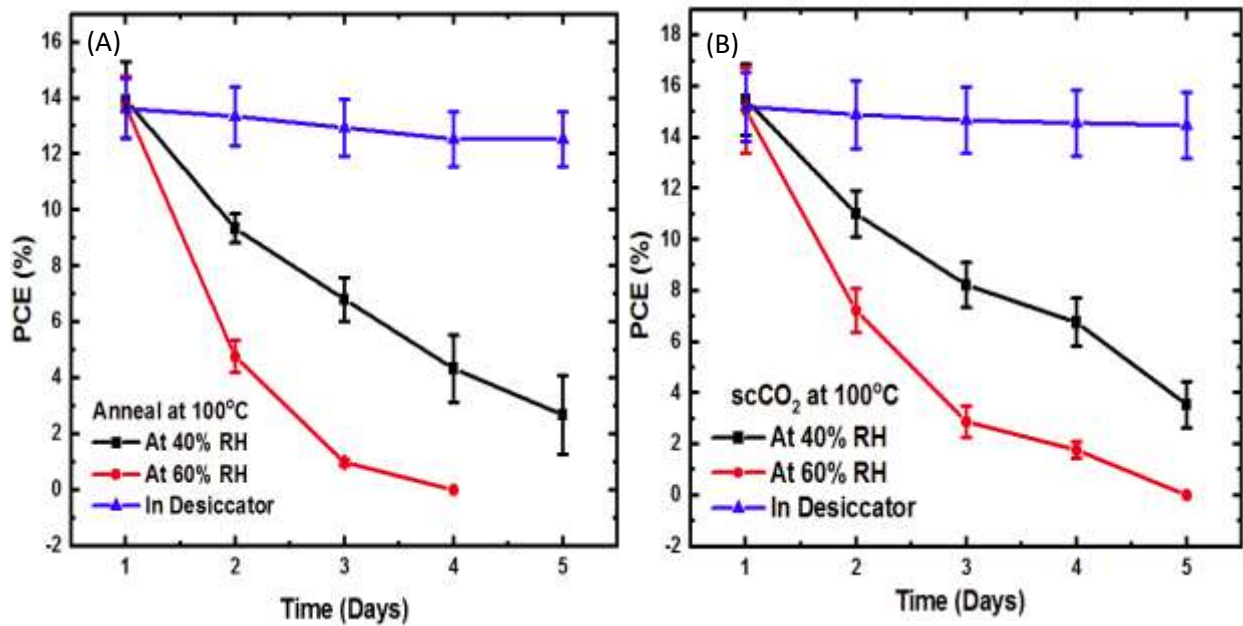
Figure 6.5: PCE degradation rate of perovskite films after annealing with (A) thermal at 100°C

(B) $scCO_2$ at 100°C

When the devices are kept in a dry desiccator, the PCE of both films thermally annealed and with $scCO_2$ are relatively constant. This collaborates with data shown in the XRD and UV-Vis, where less moisture did not have a detrimental effect on the perovskite film. The PCE tracked in days after exposure to a relative humidity of 60% showed a one-day rapid degradation with no efficiency for thermally annealed films at 50℃. Compared to samples with $scCO_2$, the degradation was steep but much slower and faded out by day 4. This trend was similar for samples exposed to 40% RH. Thus, $scCO_2$ annealed perovskite films at lower temperatures have not only better film quality (greater smoothness, larger grain) and better crystallinity but also high photovoltaic performance and better degradation rate compared to films thermally annealed at lower temperatures [25] [26] [27].

Figure 6.5 (A and B) compares the power conversion efficiency degradation rate of films thermally annealed and with $scCO_2$ at a lower temperature of 100℃, after exposure to different relative humidity parameters. On day one, before any humidity exposure, the average PCE of films thermally annealed at 100℃ were 13.93 ± 1.36%, 13.68 ± 1.10%, and 13.63 ± 1.07%, which were used for 40% RH, 60% RH exposure experiment respectively. The degradation trend in days of perovskite films thermally annealed at 100℃ was very similar to those annealed with $scCO_2$ at 50℃ and much improved than ones thermally annealed at 50℃ as earlier shown. The average PCE and degradation rate of films annealed in $scCO_2$ at 100℃ were overall slightly better than ones thermally annealed at 100℃. Since the change was not dramatic, we see no significant benefit in using high temperature $scCO_2$ annealing of perovskite films compared to thermal annealing at similar temperatures.

Reference

1. Y. Rong, Y. Hu, A. Mei, H. Tan, M.I. Saidaminov, S.I. Seok, M.D. McGehee, E.H. Sargent, H. Han, Challenges for commercializing perovskite solar cells, Science, 361 (6408) (2018), p. eaat8235, 10.1126/science.aat8235

2. J. Kang, K. Han, X. Sun, L. Zhang, R. Huang, I. Ismail, Z. Wang, C. Ding, W. Zha, F. Li, Q. Luo, Y. Li, J. Lin, C.-Q. Ma, Suppression of Ag migration by low-temperature sol-gel zinc oxide in the Ag nanowires transparent electrode-based flexible perovskite solar cells, Org. Electron., 82 (2020) (2020), Article 105714, 10.1016/j.orgel.2020.105714

3. Z. Song, A. Abate, S.C. Watthage, G.K. Liyanage, A.B. Phillips, U. Steiner, M. Graetzel, M. J. Heben, Perovskite solar cell stability in humid air: partially reversible phase transitions in the PbI_2-CH_3NH_3I-H_2O system, Adv. Energy Mater., 6 (19) (2016), p. 1600846, 10.1002/aenm.201600846

4. J. Yang, B.D. Siempelkamp, D. Liu, T.L. Kelly, Investigation of $CH_3NH_3PbI_3$ degradation rates and mechanisms in controlled humidity environments using in situ techniques, ACS Nano, 9 (2) (2015), pp. 1955-1963, 10.1021/nn506864k

5. D. Bryant, N. Aristidou, S. Pont, I. Sanchez-Molina, T. Chotchunangatchaval, S. Wheeler, J.R. Durrant, S.A. Haque, Light and oxygen induced degradation limits the operational stability of methylammonium lead triiodide perovskite solar cells, Energy Environ. Sci., 9 (5) (2016), pp. 1655-1660, 10.1039/C6EE00409A

6. T.-Y. Yang, N.J. Jeon, H.-W. Shin, S.S. Shin, Y.Y. Kim, J. Seo, Achieving long-term operational stability of perovskite solar cells with a stabilized efficiency exceeding 20% after 1000 h, Adv. Sci., 6 (14) (2019), p. 1900528, 10.1002/advs.201900528

7. B. Conings, J. Drijkoningen, N. Gauquelin, A. Babayigit, J. D'Haen, L. D'Olieslaeger, A. Et hirajan, J. Verbeeck, J. Manca, E. Mosconi, F.D. Angelis, H.-G. Boyen, Intrinsic thermal instability of methylammonium lead trihalide perovskite, Adv. Energy Mater., 5 (15) (2015), p. 1500477, 10.1002/aenm.201500477

8. T. Leijtens, G.E. Eperon, S. Pathak, A. Abate, M.M. Lee, H.J. Snaith, Overcoming ultraviolet light instability of sensitized TiO_2 with meso-superstructured organometal tri-halide perovskite solar cells, Nat. Commun., 4 (1) (2013), p. 2885, 10.1038/ncomms3885

9. N.N. Shlenskaya, N.A. Belich, M. Grätzel, E.A. Goodilin, A.B. Tarasov, Light-induced reactivity of gold and hybrid perovskite as a new possible degradation mechanism in perovskite solar cells, J. Mater. Chem. A, 6 (4) (2018), pp. 1780-1786, 10.1039/C7TA10217H

10. Y. Zhou, Y. Yin, X. Zuo, L. Wang, T.-D. Li, Y. Zhou, N.P. Padture, Z. Yang, Y. Guo, Y. Xue, K. Kisslinger, M. Cotlet, C.-Y. Nam, M.H. Rafailovich, Enhancing chemical stability and suppressing ion migration in $CH_3NH_3PbI_3$ perovskite solar cells via direct backbone attachment of polyesters on grain boundaries

11. S. Tan, I. Yavuz, N. DeMarco, T. Huang, S.-J. Lee, C.S. Choi, M. Wang, S. Nuryyeva, R. Wang, Y. Zhao, H.-C. Wang, T.-H. Han, B. Dunn, Y. Huang, J.-W. Lee, Y. Yang, Steric impediment of ion migration contributes to improved operational stability of perovskite solar cells, Adv. Mater., 32 (11) (2020), p. 1906995, 10.1002/adma.201906995

12. J.H. Noh, S.H. Im, J.H. Heo, T.N. Mandal, S.il Seok, Chemical management for colorful, efficient, and stable inorganic− organic hybrid nanostructured solar cells, Nano Lett., 13 (2013), pp. 1764-1769, 10.1021/nl400349b

13. Z. Li, M. Yang, J.S. Park, S.H. Wei, J.J. Berry, K. Zhu, Stabilizing perovskite structures by tuning tolerance factor: formation of formamidinium and cesium lead iodide solid-state alloys, Chem. Mater., 28 (2016), pp. 284-292, 10.1021/acs.chemmater.5b04107

14. M. Saliba, T. Matsui, J.Y. Seo, K. Domanski, J.P. Correa-Baena, M.K. Nazeeruddin, S.M. Zakeeruddin, W. Tress, A. Abate, A. Hagfeldt, M. Grätzel, Cesium-containing triple cation perovskite solar cells: Improved stability, reproducibility and high efficiency, Energy Environ. Sci., 9 (2016), pp. 1989-1997, 10.1039/c5ee03874j

15. L. Mao, C.C. Stoumpos, M.G. Kanatzidis, Two-dimensional hybrid halide perovskites: principles and promises, J. Am. Chem. Soc., 141 (2019), pp. 1171-1190, 10.1021/jacs.8b10851

16. J. Yan, W. Qiu, G. Wu, P. Heremans, H. Chen, Recent progress in 2D/quasi-2D layered metal halide perovskites for solar cells, J. Mater. Chem. A, 6 (2018), pp. 11063-11077, 10.1039/c8ta02288g

17. Y. Li, J. Shi, J. Zheng, J. Bing, J. Yuan, Y. Cho, S. Tang, M. Zhang, Y. Yao, C.F.J. Lau, D.S. Lee, C. Liao, M.A. Green, S. Huang, W. Ma, A.W.Y. Ho-Baillie, Acetic acid assisted crystallization strategy for high efficiency and long-term stable perovskite solar cell, Adv. Sci., 7 (2020), 10.1002/advs.201903368

18. T.H. Han, J.W. Lee, C. Choi, S. Tan, C. Lee, Y. Zhao, Z. Dai, N. de Marco, S.J. Lee, S.H. Bae, Y. Yuan, H.M. Lee, Y. Huang, Y. Yang.   Perovskite-polymer

composite cross-linker approach for highly-stable and efficient perovskite solar cells, Nat. Commun., 10 (2019), pp. 1-10, 10.1038/s41467-019-08455-z

19. S. Ito, S. Tanaka, K. Manabe, H. Nishino, Effects of surface blocking layer of Sb_2S_3 on nanocrystalline TiO_2 for $CH_3NH_3PbI_3$ perovskite solar cells, J. Phys. Chem. C, 118 (2014), pp. 16995-17000, 10.1021/jp500449z

20. N. Arora, M.I. Dar, A. Hinderhofer, N. Pellet, F. Schreiber, S.M. Zakeeruddin, M. Grätzel, Perovskite solar cells with CuSCN hole extraction layers yield stabilized efficiencies greater than 20%, Science, 358 (2017), pp. 768-771, 10.1126/science.aam5655

21. A. Aftab. M. I. Ahmad, A review of stability and progress in tin halide perovskite solar cell, Solar Energy, 216 (2021) 26 – 27. doi.org/10.1016/j.solener.2020.12.065

22. M.K. Rao, D.N. Sangeetha, Y.N. Sudhakar, M.G. Mahesha, Review on persistent challenges of perovskite solar cells' stability, Solar Energy, 218 (2021) 469 – 491. doi.org/10.1016/j.solener.2021.03.005.

23. M. Jeevarag, S. Sudhahar, M.K. Kumar, Evolution of stability enhancement in organo-metallic halide perovskite photovoltaics – a review, 27 (2021) 102159. doi.org/10.1016/j.mtcomm.2021.102159.

24. J.M. Frost, K.T. Butler, F. Brivio, C.H. Hendon, M. van Schilfgaarde, A. Walsh, Atomistic origins of high-performance in hybrid halide perovskite solar cells, Nano Lett., 14 (2014), pp. 2584-2590

25. G. Annohene, G.C. Tepper, Efficient perovskite solar cells processed in supercritical carbon dioxide, J. Supercrit. Fluids. 171 (2021) 105203. doi.org/10.1016/j.supflu.2021.105203

26. N. Ahn, D.Y. Son, I.H. Jang, S.M. Kang, M. Choi, N.G. Park, Highly Reproducible Perovskite Solar Cells with Average Efficiency of 18.3% and Best Efficiency of 19.7%

Fabricated via Lewis Base Adduct of Lead(II) Iodide, J. Am. Chem. Soc. 137 (2015) 8696–8699. doi:10.1021/jacs.5b04930.

27. G. Annohene, G.C. Tepper, The Journal of Supercritical Fluids Low temperature formation of $CH_3NH_3PbI_3$ perovskite films in supercritical carbon dioxide, J. Supercrit. Fluids. 154 (2019) 104604. doi:10.1016/j.supflu.2019.104604.

28. G. Annohene, J. Pascucci, D. Pestov, G.C. Tepper, Supercritical fluid-assisted crystallization of CH3NH3PbI3 perovskite films, J. Supercrit. Fluids. 156 (2020) 104684. doi:10.1016/j.supflu.2019.104684.

29. J. Burschka, N. Pellet, S. Moon, R. Humphry-Baker, M.K. Nazeeruddin, M. Gratzel, Sequential deposition as a route to high-performance perovskite-sensitized solar cells, Nature, 499 (2013) 316–319. doi:10.1038/nature12340.

30. J-H. Im, I-H. Jang, N. Pellet, M. Gratzel, N-G. Park, Growth of CH3NH3PbI3 cubiods with controlled size for high-efficiency perovskite solar cells, Nat. Nanotechnol. 9 (2014) 927–932. doi:10.1038/nnano.2014.181.

31. J. Luo, R.Z. Qiu, Z.S. Yang, Y.X. Wang Q.F Zhang, Mechanism and effect of g-butyrolactone solvent vapor post-annealing on the performance of a mesoporous perovskite solar cell, RSC Advances (2018) 724–731. doi:10.1039/c7ra10695e.

32. T. Oku, Crystal Structures of $CH_3NH_3PbI_3$ and related perovskite compounds used for solar cells, Solar Cells - New Approaches and Reviews, (2015) 78-98, http://dx.doi.org/10.5772/59284

33. Q. Chen, H. Zhou, Z. Hong, S. Luo, H. Duan, H. Wang, Y. Liu, G. Li, Y. Yang, Planar Heterojunction Perovskite Solar Cells via Vapor-Assisted Solution Process, J. Am. Chem. Soc (2014) 622–625. doi:10.1021/ja411509g.

34. G. Yang, C. Wang, H. Lei, X. Zheng, P. Qin, L. Xiong, X. Zhao, Y. Yan, G. Fang, Interface engineering in planar perovskite solar cells: energy level alignment, perovskite morphology control and high performance achievement, J. Mater. Chem. A (2017) 1658–1666. doi:10.1039/c6ta08783c.

35. D. Acuna, B. Krishnan, S. Shaji, S. Sepulveda, J.L Menchaca, Growth and properties of lead iodide thin films by spin coating, Bull. Mater. Sci. 9 (2016) 1453-1460. DOI 10.1007/s12034-016-1282-z

36. D. Shen, X. Yu, X. Cai, M. Peng, Y. Ma, X. Su, L. Xiao, D. Zou, Understanding the solvent-assisted crystallization mechanism inherent in efficient organic-inorganic halide perovskite solar cells, J. Mater. Chem. A. 2 (2014) 20454–20461. doi:10.1039/c4ta05635c.

CHAPTER 7

CONCLUSION

It was demonstrated that perovskite crystals can grow at low temperatures with the help of $scCO_2$. $ScCO_2$ serves as an anti-solvent to the perovskite precursors, promoting solid-state crystallization and increasing the grain size, crystallinity, and optical absorbance of perovskite films. Because of its special properties (diffusivity, permeability, density, and viscosity), $scCO_2$ is an excellent medium for solid-state crystallization. Its low critical pressure and temperature allow for mass production scalability. In the supercritical region, increasing temperature causes grain size to increase while increasing pressure causes grain size to decrease. Post-deposition annealing in $scCO_2$ resulted in full conversion of perovskite, while thermal annealing alone resulted in incomplete conversion at lower temperatures. Annealing at 100℃ resulted in smaller average grains (404 nm) than annealing at 45℃ in $scCO_2$ at 1200psi (408nm).

Perovskite films were developed in binary supercritical fluid solvents containing CO_2 as the main solvent and a variety of small organic molecules as cosolvents. Supercritical fluid enhanced molecular transport inside the film and out of the film, resulting in the creation of a diverse variety of film morphologies. Organic cosolvents may be used in combination with CO_2 to improve overall molecular transport inside the film, or they may associate preferentially with a specific film component to selectively mobilize or remove one component within a solid film. The average grain size, film morphology, and absorption spectra can all be modified in this way. Cosolvents were rated based on the strength of their hydrogen bonds, and their interactions with the PbI_2 and CH_3NH_3I film constituents were significantly different. While this research centered

118

on one kind of perovskite film and a specific group of organic cosolvents, the technique presented here should be applicable to improving or tuning the morphology, crystal structure, optical, and electrical properties of a broad variety of thin films.

The use of supercritical carbon dioxide to crystallize perovskite films at low temperatures resulted in high-quality perovskite films and high-efficiency photovoltaic devices. With $scCO_2$ parameters of 1300psi and 100°C, the highest performing devices had a PCE of 17.52 percent and a PCE of 17.22 percent with $scCO_2$ parameters of 1300psi and 50°C. As compared to films annealed at those temperatures without $scCO_2$, the perovskite film quality and system photovoltaic output were increased. $ScCO_2$ is a readily available, environmentally friendly anti-solvent to perovskite materials, and we have demonstrated that it is highly promising for the development of high-quality perovskite films and perovskite solar cells with exceptional photovoltaic efficiency.

Studies into moisture degradation mechanisms comparing the use of $scCO_2$ and thermal annealed $CH_3NH_3PbI_3$ perovskite devices were reported. Moisture degradation studies of perovskite solar cells are very crucial in understanding how to engineer and improve the device lifetime. We have found that at lower annealing temperatures, not only does using $scCO_2$ in annealing result in better film quality and absorption but also yields better device performance and degradation rate. Its photovoltaic performance and degradation trend are also comparable, if not better, than the more traditional thermal annealing at 100°C.

VITA
Gilbert Annohene

Address: 5725 Kilrush Court, Apt. D, Henrico VA, 23228

Email: annoheneg@vcu.edu Phone: (804) 855-7713

EDUCATION

- **Ph. D.** in Mechanical and Nuclear Engineering   Expected May 2021
  Virginia Commonwealth University – Richmond, Virginia.
- **M.Sc.** in Mechanical and Nuclear Engineering   August 2017 – May 2019
  Virginia Commonwealth University – Richmond, Virginia.
- **B.Sc.** in Mechanical Engineering   August 2012 – June 2016
  Kwame Nkrumah University of Science and Technology - Kumasi, Ghana.

RESEARCH EXPERIENCE

Virginia Commonwealth University: Graduate Researcher   August 2017 – May 2021

Nano-structured Materials Laboratory

- Attained patent on the novel use of supercritical fluids to crystallize (Nucleation and Crystal growth) perovskite semiconductors processed in a glovebox and in a cleanroom, achieving record 17.3% PCE.
- Procured and set up the whole laboratory for thin film manufacturing and electrical characterization (current-voltage, external quantum efficiency) of solar devices.
- Lead team of six in manufacturing optoelectronic device prototypes by monitoring and maintaining product development schedules, creating specifications and technical documentations.
- Expert in thin film deposition process analytical technology, kinetics of reactions and data analysis.
- Independently designed experiments and carried out scientific work, wrote and/or reviewed SOP documentation, process analytical technology and statistical data analysis.

Microsensor and Radiation detector laboratory

- Incorporated three conductive nanoparticles (carbon black, carbon nanotubes and graphene) to yield electrospun superhydrophobic polymeric fibers for de-wetting applications.
- Experimented into biodegradable electrospun polymeric scaffolds for tissue engineering applications by collaborating with a team of six on the innovatory seeding of biological cells.
- Defined manufacturing processes for products based on bench scale tests, including fundamental similarities between process conditions and process chemistry.
- Integrated motion control unit into electrospray system and machine vision to monitor Taylor Cone.

National Renewable Energy Laboratory (NREL): Hands-on Training   July 2019

- One of fifteen graduate students globally selected for hand on training on the design and fabrication of Si, III-V, CdTe and perovskite solar cell technologies.
- Trained on six PV-related characterization techniques, including secondary ion mass spectrometry, time-resolved photoluminescence, X-ray and UV photoelectron spectroscopy, and scanning probe techniques.
- Mastered PV module fabrication and characterization as well as outdoor testing of photovoltaic modules.

TEACHING EXPERIENCE

Virginia Commonwealth University: Teaching Assistant   August 2017 – May 2021

- Assisted in Fluid Mechanics, Thermodynamics, Numerical Methods, Law and Engineering, Engineering Analysis and Continuum Mechanics at Virginia Commonwealth University.

- o Assisted faculty members with classroom instruction, controlling grade center, exams and projects.
- o Held office hours to tutor and mentor undergraduate and graduate student with course contents.

ENGINEERING EXPERIENCE

Vie De France Yamazaki: Production Associate   March 2017 – August 2017
- o Led process engineering studies to introduce new and improved processing techniques and technologies
- o Created scale up models by developing expert processing equipment understanding at different scales.
- o Developed a strong understanding of how key product quality attributes are influenced by processing.
- o Presided a team of four in reviewing production specifications to verify accurate weights and measurements

Atlantic International Holdings: Engineering Intern   May 2015 – August 2015
- o Interfaced with a range of operators, technicians, and other technical staff across Production and R&D teams.
- o Supervised five HVAC technicians on troubleshooting, preventive and corrective maintenance
- o Validated a range of 2D and 3D CAD designs leading to meet goals, specifications and better performance.

GRADUATE COURSEWORK

Engineering Analysis	Engineering Materials
Advanced Characterization of Matter	Continuum Mechanics
Photovoltaic	Fundamentals of Solar Cells
Polymer Engineering	Project Management
Heat and Mass Transfer	Signal Processing
Fundamentals of Photonics	Law and Engineering
Nuclear Engineering	Engineering Simulations

SKILLS

Software: SolidWorks, MATLAB, Originlab, Mathematica, Python, AutoCAD, Ansys, ChemOffice, JMP.
Technical: Thin film deposition, Design of Experiment, Equipment Installation, Equipment Maintenance, Troubleshooting, Quality Control Analysis, Test instrumentation, R&D.
Equipment: SEM, FIB-SEM, XRD, Spectroscopic ellipsometer, AFM, UV-Vis, FTIR, Mass Spectrometer, Electrospinning system, Hysitron Nano-indenter, Nano-film deposition (sputtering, E-beam, thermal evaporation), SIMS.

PUBLICATIONS, PROCEEDING AND PATENT

Published
- o **G. Annohene**, G.C. Tepper, Efficient perovskite solar cells processed in supercritical carbon dioxide, J. Supercritical Fluids. 171 (2021) 1052034
- o **G. Annohene**, G.C. Tepper, Supercritical fluid-assisted crystallization of $CH_3NH_3PbI_3$ perovskite films, J. Supercritical Fluids. 156 (2020) 104684.
- o **G. Annohene**, G.C. Tepper, Low temperature formation of $CH_3NH_3PbI_3$ perovskite films in supercritical carbon dioxide, J. Supercritical Fluids. 154 (2019) 104604.
- o J. Bracamonte, S.K Saunders, S. Cole, **G. Annohene**, G.C Tepper, J. S Soares, In vitro degradation of electrospun polycaprolactone tissue engineering scaffolds under cyclical dynamic loading, Summer Biomechanics, Bioengineering and Biotransport Conference 2019, PA.

Patent granted

Gary Tepper and Gilbert Annohene: (62/905,511), Low Temperature Formation of Perovskite Films in Supercritical CO_2.

ACTIVITIES AND PROFESSIONAL SOCIETIES

Presentations
o   Graduate Symposium Poster presentation, VCU 2019.
o   National Renewable Energy Laboratory, Golden Colorado, 2019.
o   International Society for Optics and Photonics, San Diego California, 2019.
o   International Society for Optics and Photonics – Digital Forum, San Diego California, 2020.

Professional societies
o   American Society of Mechanical Engineers – National Student Member (2019 - present).
o   International Society for Optics and Photonics – National Student Member (2019 – present).
o   National Society of Black Engineers

Other Experience
o   Peer review committee member for tenure and promotion of professors at VCU MNE Engineering department.
o   Black Graduates Students Association VCU Secretary August 2018 – May 2019.